

Megaelectron volt secondary-ion mass spectrometry - yield dependence on experimental parameters and new capabilities of the technique

vorgelegt von:

Diplom-Physiker
Valentin Stoytschew

von der Fakultät II - Mathematik und Naturwissenschaften
der Technischen Universität Berlin

zur Erlangung des akademischen Grades
Doktor der Naturwissenschaften, Dr.rer.nat.

genehmigte Dissertation

Promotionsausschuss:

Vorsitzender: Prof. Dr. rer. nat. Norbert Esser

Gutachter: Prof. Dr. rer. nat. Birgit Kanngießer

Gutachter: Dr. Milko Jaksic

Tag der wissenschaftlichen Aussprache: 26. April 2019

Berlin 2019

„It`s not an exact science “

Dr. JD

„It takes time “

Professor Roberto Daniel Perez

“gnarr brghhh \$%#?/”

Natko S.

Abstract

Time of flight Mega-electron Secondary Ion Mass Spectroscopy (TOF MeV SIMS) is a mass spectrometry technique using swift heavy ions ($m > 16 u$, $E_{kin} > 1 MeV$) to induce desorption of secondary ions from a sample. While swift heavy ions have been used for several decades to achieve high molecular secondary ion yields in mass spectrometry, there has been no systematic investigation into the experimental parameters' influence on the secondary ion yield for TOF MeV SIMS.

This thesis tries to fill this knowledge gap and while doing so, various assumptions that have been made about TOF MeV SIMS are tested and new possibilities of the technique are explored, using the RBI heavy ion microprobe.

The work began with an upgrade of the setup to provide accurate yield measurements. For this purpose, a detector that periodically measures the beam current was installed. Additionally, the possibilities for capillary usage in Ion Beam analysis and primary ion triggered MeV SIMS were explored.

With the setup ready, the influence of various experimental parameters on the secondary ion yield for MeV SIMS has been tested. The reproducibility as well as the efficiency of the measurement process were improved and a value for the error of an MeV SIMS measurement at the RBI-Setup was determined.

Further on dynamic MeV SIMS as well as standard based quantitative MeV SIMS were tried out in analogy to keV-SIMS. The results indicate that it is possible to realise depth scans with MeV SIMS and that standard based MeV SIMS is possible, if the experimental parameters are well known and controlled.

After the work on the experimental technique itself, MeV SIMS was applied to four different applications: Analysis of varnish used in church icons, study of the effects of MeV-Ion beams on the bonds in PMMA, forensics investigations on ink, showing who last wrote on a document, and testing of PCBs for materials not allowed under RoHS regulations.

The potential of the Method has been shown in these tests of techniques and applications. There is more than the ambient pressure application alone for MeV SIMS in the future and combining the ambient pressure setup with the applications explored in this thesis provides many possibilities to further develop the MeV SIMS technique.

Kurzusammenfassung

Time-of-Flight Mega-Elektron Sekundärionenmassenspektroskopie (TOF MeV SIMS) ist eine Massenspektrometrietechnik die schnelle, schwere Ionen verwendet ($m > 16 \text{ u}$, $E_{\text{kin}} > 1 \text{ MeV}$), um Sekundärionendesorption von einer Probe zu induzieren. Obwohl schnelle, schwere Ionen schon seit einigen Jahrzehnten zur Desorption von Sekundärionen mit hohem Ertrag verwendet werden, gibt es bis heute noch keine systematische Untersuchung zum Einfluss der experimentellen Parameter auf den Sekundärionenertrag. Diese Arbeit versucht diese Informationslücke zu schließen und dabei wurden, mit dem MeV SIMS System des RBI, einige der bestehenden Thesen bezüglich TOF MeV SIMS überprüft und das Entwicklungspotential der Technik ausgelotet.

Die Arbeit begann mit einer Verbesserung des Aufbaus. Um exakte Gewinnmessungen zu ermöglichen, wurde eine Messmethode für den Primärionenstrom, der während einer MeV SIMS Messung auf die Probe fällt, entwickelt. Zusätzlich wurde eine neue Art Glaskapillare für die Verringerung des Ionenstrahldurchmessers erprobt und TOF MeV SIMS mit einem Startsignal, das durch die Primärionen erzeugt wird.

Nach diesen Arbeiten am Aufbau wurde der Einfluss verschiedener Parameter im Messaufbau auf die Sekundärionendetektion geprüft. Wichtige Parameter sind hier der Winkel zwischen Probe und Extraktor, der Abstand zwischen Extraktor und Probe, die Beschleunigungsspannung zwischen Probe und Extraktor, die Größe des Messbereiches über den gerastert wird und der Primärionentyp. So wurde die Effizienz der Messmethode verbessert und die Reproduzierbarkeit der Messungen erhöht. Zusätzlich wurde eine Abschätzung des Fehlers einer MeV SIMS Messung gefunden, die auf experimentellen Daten beruht.

Anschließend wurden zwei neue MeV SIMS-Techniken in Analogie zur keV-SIMS getestet: Dynamische MeV SIMS und standardbasierte quantitative MeV SIMS. Den Ergebnissen nach können beide Techniken in MeV SIMS angewandt werden. Besonders nachdem die Vorarbeit bei der Bestimmung des Einflusses der experimentellen Parameter die Reproduzierbarkeit einer Messung deutlich erhöht hat, was die standardbasierte Quantifikation exakter macht.

Nach diesen Arbeiten an der Technik allein, wurde MeV SIMS zur Lösung einiger Fragestellungen angewandt. Dazu gehörte die Frage welche Art Lack auf einer religiösen Ikone verwendet wurde, um so die Reparatur durch den Konservatoren zu ermöglichen, die Frage welche chemischen Bindungen sich in PMMA nach Bestrahlung durch Ionen bilden, eine Fragestellung aus der Forensik, bei der festgestellt werden soll mit welchem Stift ein Dokument zuletzt bearbeitet wurde und die Suche nach Materialien in einer PCB, die unter den RoHS-Bestimmungen verboten sind.

Die Tests und Anwendungen, die in dieser Arbeit präsentiert werden, zeigen die Möglichkeiten von MeV SIMS. Neben der Arbeit an der Entwicklung von MeV SIMS bei Normaldruck gibt es noch zahlreiche Erweiterungen und Techniken, die sowohl in der Kombination mit MeV SIMS bei Normaldruck, als auch bei MeV SIMS im Vakuum, von großem Nutzen sein können.

Acknowledgements

Let me start with the most important part first, it is time to say: “Thank you!”. A few years have passed now since I started my time at the Ruder Boskovic Institute and thanks to the nice people there I learned quite a few things along the way. I also had the great opportunity to spend some time at the IAEA, ETHZ and University of Surrey and must thank the people there for the friendly welcome and letting me take part in the lab-work. Last but not least I also have to thank my Research group at the TU-Berlin for the support and advice given, especially during the write-up part of the work on the thesis.

The people working in these labs have been part of an experience that showed me how glad I can be to work in science.

All this came as a part of a Marie-Curie grant, a great program to get an insight in as many parts of one’s field as possible and I can only recommend taking the opportunity if this grant is available.

Here the names of all the people that I want to thank for making the time spent while working on the thesis a great time! Thank you, Danke and Hvala puno Andrea, Damir, Milko, mala Iva, Ivancica and Iva, Wolfgang, Birgit, Zdravko, Marta, Monica, Max, Koran Zokan, Donny, Tonci, Veljko, Nico, Ivan, Marko, Roger, ฟูฟี่, Backe, Daniel,Georgi, Daniel, Daniel, Milen, Mariannne, Edu, Alex, Alexander, Martin, Roberto, Damir, Pawel, Sabine, Seppl, Chris, Victor, Julien, Mladen, Maria, Roberto, Vikingo, Vani, Matsuo-San and his team, Steffen und Marcel, Goldmann, Bor, Marko, Ursula, Martha, Gerhard, Iveta, Johnny, R.Norarat, Brian Schulz, Zetze, Dimitr and everyone else I might have forgotten. I can assure you it wasn’t on purpose.

Acronyms

Amu/u – Atomic Mass Unit

Da – Dalton, mass unit equivalent to 1 amu

DAM - Dipole analyser magnet

DAQ - Data acquisition

DSM - Dipole switching magnet

EMQ – Electromagnetic quadrupole

IBC - Ion beam centre

MC SNICS - Multi cathode source of negative ions by caesium sputtering

MetA-SIMS – Metal assisted secondary ion mass spectrometry

MeV/keV – Mega/kiloelectron volt

MS – Mass spectrometry

PIXE – Particle induced x-ray emission

PMMA – Polymethylmethacrylates

PS – Polystyrene

RBI – Ruder Bošković Institute

RBS – Rutherford backscattering

SIMS – Secondary ion mass spectrometry

SRIM - Stopping and range of ions in matter

STIM – Scanning transmission ion microscopy

TOF – Time of flight

VI – Visual interface

Content

Abstract	3
Kurzusammenfassung	4
Acknowledgements	6
Acronyms.....	7
1 Introduction.....	11
2 Theoretical background.....	13
2.1 The Stopping Force.....	14
2.2 The secondary ion desorption process.....	17
3 Experimental Setup	20
3.1 Ion Source.....	21
3.2 Ion transport system	22
3.2.1 Electrostatic optics	22
3.2.2 Electromagnetic optics	26
3.3 Ion acceleration.....	29
3.4 Microbeam setup	31
Figure 3-4-2: Ray tracing simulation of a triplet setup using high excitation mode [51]. The beam has its first focal point in the EMQ array.....	34
3.5 Sample chamber.....	34
3.6 Mass spectrometer.....	35
3.6.1 Start signal of the TOF measurement.....	36
3.6.2 Stop signal of the TOF measurement	38
3.6.3 Calibration of the TOF measurement.....	41
3.6.4 Further possible improvements for an MeV SIMS	43
3.7 Data acquisition.....	43
4 Upgrades of the setup	45
4.1. Ion beam intensity monitor.....	46
4.1.1 Mounting and movement of the ion beam intensity monitor	47
4.1.2 Calibration of the ion beam intensity monitor.....	48
4.1.3 Validation of the beam intensity measurement	49
4.1.4 Systematic error of the primary ion measurement.....	52
4.2 Thick wall capillary for ion beam collimation.....	52
4.2.1 Production and usage of the capillary.....	53
4.2.2 Testing of capillary characteristics	55

4.3 Transmission triggered MeV SIMS	59
4.3.1 RBI setup.....	59
5. Secondary ion yield dependence on experimental parameters	63
5.1 Secondary ion yield dependence on setup parameters.....	63
5.1.0 Variance of the yield measurement	64
5.1.1 Dependence on the position on the sample	65
5.1.2 Angle dependence.....	67
5.1.3 Dependence on the scan area size and the distance between extractor and sample surface	73
5.1.4 Dependence on the extraction voltage.....	77
5.1.5 Summary.....	81
5.2 Primary ion type and fluence dependence of the secondary ion yield.....	81
5.2.1 Primary ion characteristic dependence.....	82
5.3 Fluence dependence of the secondary ion yield (dynamic MeV SIMS)	84
5.3.1 Crater formation.....	84
5.3.2 Static SIMS limit for organic compounds using MeV Ions.....	86
5.3.3 High fluence (Dynamic) SIMS behaviour for homogenous samples	87
5.3.4 Summary.....	97
5.4 MeV SIMS on multi-layer samples.....	98
5.4.1 MeV SIMS on PS/PMMS double layer sample.....	98
5.4.2 Spectra of metalized Leucine samples	100
5.4.3 Summary.....	102
5.5 MeV SIMS of mixed samples	103
5.5.1 Production of mixed samples	103
5.5.2 Yields of mixed samples	104
6 MeV SIMS Applications	107
6.1 Application I: Forensics.....	107
6.2 Application II: Study of post-Byzantine Albanian Orthodox Church icons	113
6.3 Application III: Study of the fragmentation and cross-linking effects in PMMA.....	115
6.4 Application IV Mass spectrum of a PCB board	118
7 Conclusions and Outlook.....	120
Appendix A MeV SIMS spectra compilation.....	123
A.1 Glycine.....	123
A.2 Leucine	125

A.3 Arginine	126
A.4 Irganox 1010.....	127
A.5 Polymethylmethacrylate	129
A.6 Polystyrene.....	131
A.7 Cholesterol	134
A.8 Quinacridone rosé PV 19.....	135
A.9 Phthalocyanine blue PB 15.....	136
Appendix B Sample thickness influence	137
Bibliography.....	139

1 Introduction

Time-of-flight megaelectron volt secondary-ion mass spectrometry (TOF MeV SIMS) employs ions with a kinetic energy in the MeV range (primary-ions) to desorb charged particles (secondary-ions) from a sample which are then detected in a TOF mass spectrometer [1, 2, 3]. It belongs to the group of mass spectrometry material analysis techniques. Mass spectrometry determines the mass of particles obtained from a sample, thus providing information on the type of atoms and molecules present. This sets it apart from other techniques like for example x-ray fluorescence analysis (XRF) [4] or particle induced x-ray emission (PIXE) [5] where the information is obtained from characteristic radiation emitted by the sample. Two side effects from this type of measurement are that a small part of the sample is permanently removed, and that the information is obtained almost exclusively from the surface layer.

The mass spectrometry methods that can be used to analyse particles from a sample are manifold and can be chosen depending on the necessities of the experiment. They include gas/liquid chromatography-mass-spectrometry (GC/LC-MS) [6, 7], desorption electrospray ionization (DESI) [8], matrix assisted laser desorption/ionisation (MALDI) [9], electron ionisation (EI) [10], plasma desorption ionization mass spectrometry (PDMS) [11], kiloelectron volt secondary-ion mass spectrometry (keV-SIMS) [12] and many more, each having their distinct advantages and disadvantages. DESI for example provides high yields for high mass ions and can be used in ambient pressure while spatial resolution is poor [13, 14]. KeV-SIMS has high resolution imaging capabilities [15] but lacks the ambient pressure application and high mass yield.

Now, if one is looking for a technique that performs well in all these categories, MeV SIMS is a viable candidate and a number of setups have been built in the last years [1, 16, 17, 18] including one at the Ruđer Bošković Institute (RBI) in Zagreb [19].

MeV SIMS setups can provide micrometre and sub-micrometre imaging resolution [20], ambient pressure applications [21, 22] and good high mass yields [3, 23, 24]. The Ambient pressure application becomes possible due to the range of MeV ions in air [25, 26], good imaging resolution is obtained by focussing of ion beams to micrometre and sub micrometre diameters [27], while electronic stopping, the dominant energy deposition process for ions with a kinetic energy in the MeV-range, desorbs very efficiently a great number of heavy mass ions from the sample [3, 23].

The electronic stopping process deposits a high amount of energy in the target compared to the nuclear stopping process. As the energy is deposited into the electronic system, as opposed to elastic collisions between the nuclei for nuclear stopping, its cross section is much higher once the primary ion has reached velocities above the Bohr velocity of the electrons in the target [28].

The distribution of the deposited energy is still a matter of discussion, but it is evident that it leads to desorption of a significantly higher number of high mass secondary ions and lower fragmentation of the targets molecular ions when compared to keV SIMS [1, 24].

MeV SIMS setups have been realized in various ways according to the different approaches chosen by the Research Groups working on the technique. At the RBI the most common type of setup, using a vacuum chamber, electromagnetic optics, triggering by beam chopping and extraction through a potential difference between the sample and the TOF-tube of a mass spectrometer is used. Similar Setups exist at the Kyoto University accelerator facility [17], at the Jožef Stefan Institute (JSI) in Ljubljana [16] or in Surrey at the Ion Beam Centre (IBC) [1]. These setups show an increased secondary ion yield especially for higher molecule masses compared to keV SIMS with a spatial resolution in the micrometre range.

Apart from the conventional setup another triggering mechanism utilizing primary ions passing through the sample and hitting a detector behind the sample has been implemented at the RBI [20] to provide high secondary ion yield combined with a resolution that rivals the resolution achievable in keV SIMS.

Another way to produce a micrometre spot for MeV SIMS has been tested at the Eidgenössische Technische Hochschule Zürich (ETHZ) using capillary optics combined with secondary electron triggering of the TOF measurement [18]. This setup can use heavy high energy primary ions that cannot be focussed easily down into the micrometre range with electromagnetic optics. It also employs a fixed extractor with a large aperture. Due to the triggering process and the large extractor, this setup produces high secondary ion yields with an average spatial resolution and slightly lower mass resolution compared to other setups.

An important trend in the current research is ambient pressure MeV SIMS. The laboratories at Kyoto university and Surrey have tried different approaches to realise a working ambient pressure setup. The Kyoto group started with low pressure, so called “Wet-SIMS” [29], in an experimental chamber while the Surrey group went directly for ambient pressure SIMS by extracting the beam into air through a silicon nitride window and pushing the secondary ions in the mass spectrometer with a Helium gas flow passing over the sample [21].

Besides the work on the setup there are still many open questions regarding MeV SIMS that need to be answered. There is no comprehensive theory that fully describes the process of secondary ion desorption after MeV ion impact. Also, there is not sufficient data that demonstrates the influence of the experimental setup parameters as well as primary ion type and fluence on the secondary ion yield. With this lack of information, it is easily understandable that the capabilities of MeV SIMS for applications which are commonly used with keV-SIMS, for example dynamic SIMS on multilayer samples and quantitative SIMS, have not been tested up until now.

Naturally, any analytical technique should not only be qualitative but quantitative. Therefore, the primary goal of this thesis is to increase the amount of available experimental data on the dependence of the secondary ion yield on the setup parameters. From this information a measurement procedure with optimized efficiency and increased reproducibility can be devised, enabling the reliable testing of techniques like dynamic SIMS (depth profiling) and quantitative SIMS for MeV SIMS.

For this purpose, a main prerequisite is a reliable method to measure the low currents (fA) used in TOF MeV SIMS. This enables the precise measurement of the number of secondary ions detected in a TOF detection system for each impact of a primary ion. With this reliable yield measurement established, one can observe the effect of irradiation and surface density on the secondary ion yield enabling standard based quantitative measurements as well as depth profiling.

In the following chapter the theoretical background and open questions connected to the processes associated to primary ion impact and the emission of secondary ions will be explained. Afterwards, the experimental setup designed to reliably determine the secondary ion yield dependences will be presented, with the new devices designed particularly for this task. In the next part the experimental results obtained with the setup will be shown along with suggestions how to increase reproducibility and efficiency of the MeV SIMS experimental setup. Finally, a number of applications where the use of MeV SIMS can be advantageous will be presented.

2 Theoretical background

Mass spectrometry of secondary ions emitted from a sample after swift heavy ion impact has been first reported in 1974 by Macfarlane, Skowronski and Torgerson [30] using a Californium 252 radioactive alpha source emitting 7.3 MeV He^{2+} ions. Macfarlane et al. attributed the ion desorption to a thermal spike occurring along the ion trajectory in the target material. The thermal spike theory is one of many theories [31] postulated to describe sputtering of particles after MeV ion impact. In the following chapters the theory of energy deposition in the sample manifesting itself in the stopping force and the process of ion desorption initiated by this energy deposition will be summarised.

The use of the expression *stopping force* in the place of the usually used stopping power has been suggested by Peter Sigmund [25, 32, 33]. The stopping force is defined as the cause for the change of energy along the ions path dE/dx and thus can be defined as a force as follows from $E = \int F dx$.

2.1 The Stopping Force

The dominant form of energy transfer from the primary ion to the sample depends on the primary ion's kinetic energy. In the keV energy range the most important form of energy transfer is called nuclear stopping [25] and can be described by elastic collisions of the primary ion with one of the sample's atom's nuclei.

Conservation of momentum and energy in an elastic collision process leads to the relation for the energy transfer from the primary ion with mass M_1 and the energy E_0 onto the sample atom with mass M_2 , and the scattering angle Θ :

$$T = \frac{4E_0M_1M_2}{(M_1+M_2)^2} \sin^2 \frac{\theta}{2} \quad (2.1.A)$$

or in a centre of mass system

$$T = \frac{4E_cM_c}{M_2^2} \sin^2 \frac{\theta}{2} \quad (2.1.B)$$

with the centre of mass energy

$$E_c = \frac{E_0M_2}{(M_1+M_2)} \quad (2.1.C)$$

The scattering angle Θ depends on the impact parameter p , which is the closest distance between the two nuclei on the primary ion's trajectory past the sample atom, and on the interatomic potential between the two atoms $V(r)$. The lower limit of the integral r_{min} is the closest the primary ion can get to the secondary ion before it gets repulsed by the Coulomb force:

$$\theta = \pi - 2 \int_{r_{min}}^{\infty} \frac{pdr}{r^2 \left[1 - \frac{V(r)}{E_c} \frac{p^2}{r^2} \right]^{1/2}} \quad (2.1.D)$$

A way to describe the interatomic potential $V(r)$ is by summing up the Coulomb force between the two atoms' nuclei, including the effects of their electron clouds, and two additional effects called kinetic effect and exchange effect based on the overlap of the electron clouds and the energy change of the electrons due to the Pauli Exclusion Principle. The Coulomb repulsion depends on the atomic number of the atoms involved while the kinetic effect and the exchange effect depend on the charge distribution in the electron cloud around the core. One form of representing this potential is the use of a screening potential $\Phi(r)$ which represents the difference between $V(r)$ and the Coulomb potential caused by the charge of the atoms' core alone:

$$V(r) = \frac{\Phi(r)Z_1Z_2e^2}{r} \quad (2.1.E)$$

There are several approximations for this screening of the repulsion potential, i.e. the Bohr, Thomas-Fermi, Moliere and Lens Jensen Models [34].

The program stopping and range of ions in matter (SRIM) [34] used in this dissertation to calculate stopping forces applies its own screening function different from the approximations mentioned above. It is built upon the calculation of interatomic potentials of a selection of atom pairs using the electron densities of each atom. The results for the calculations are used as data points and function 2.1.F is fitted to them.

$$\Phi(x) = \sum_{i=1}^3 a_i \exp(-b_i x) \quad (2.1.F)$$

Here a_i and b_i are fitting parameters and x is a scaled interatomic distance $x = \frac{r_{12}}{a_I}$ simulating the effect of screening of the cores' charge at the distance r_{12} between both atoms using

$$a_I = \frac{0.8853 a_0}{Z_1^{0.23} + Z_2^{0.23}} \quad (2.1.G)$$

The parameter a_0 is the Bohr atomic radius and Z_1 and Z_2 are the atomic numbers of the elements involved.

The advantage of this approach is that interatomic potentials are considered which cannot be approximated by the classical approximations sufficiently, i.e. Boron – Boron, Nickel-Nickel and Gold-Gold interatomic potentials.

This provides one formula to calculate $V(r)$ with an acceptable variance from the previously calculated data (5 % according to SRIM chapter 2 [34]) for all tested atom pairs and makes it feasible to calculate the Energy transfer T from equation 2.1.B in a reasonable amount of time to provide a nuclear stopping force S_n :

$$S_n(E) = \int_0^\infty T d\sigma = 2\pi \frac{4EM_1M_2}{(M_1+M_2)^2} \int_0^{p_{max}} \sin^2 \frac{\theta}{2} p dp \quad (2.1.H)$$

S_n is the average over all possible energy transfers for a primary ion with Energy E . To calculate the Energy loss per distance travelled $\frac{\Delta E}{\Delta x}$ this value must be multiplied with the number of atoms per unit volume: $\frac{\Delta E}{\Delta x} = \frac{n_{atoms}}{\Delta V} S_n$.

The nuclear stopping collision described here is the starting point of a collision cascade, which leads to the ejection of secondary ions if it reaches the surface.

If the impinging ions velocity is higher than the Bohr velocity, which is about 25 keV/u, the importance of nuclear stopping in the energy deposition process decreases and electronic stopping takes over.

Electronic stopping is more complicated to model than nuclear stopping as it deals with an ion that constantly changes its charge and the electron density around it, while passing through the sample.

It has to be assumed that the primary ion's charge is fluctuating as it moves through the target while losing and collecting electrons. The primary ion's effective charge is defined as the average charge an ion has after passing by a sufficient number of ions in the target for a given primary ion speed. At this stage the electron stripping, and collection processes have reached an equilibrium state and the primary ions charge oscillates around this efficient charge value.

For hydrogen nuclei a fully stripped state is assumed in SRIM [34]. As the average distance of the hydrogen atom's electron from its nucleus is larger than the inter-atomic distances in solids the nucleus can be considered separated from its electron immediately as it passes through the first atomic layer of the sample [35]. A counter argument to this hypothesis is that the hydrogen nucleus entering the target can polarise the electron gas in the target and create a virtually bound electron [36].

Using this effective charge Z_1^* a value for the electronic stopping force S_e can be calculated with:

$$S_e = \int I(v, \rho) (Z_1^*(v))^2 \rho dx^3 \quad (2.1.I)$$

The electronic stopping force depends on the velocity v of the primary ion, the charge density of the target $\rho(x)$, the interaction function $I(v, \rho)$ for the primary ion with the electron gas in the volume dx^3 and the effective charge $Z_1^* = \gamma Z_1$, with Z_1 the atomic number of the primary ion. For the hydrogen atom the effective charge is assumed to be 1 ($\gamma = 1$). The factor γ is velocity dependent alone and represents the stripping of ions induced while passing through the target. A rough approximation for any element's stopping force in a target can thus be applied by using the relation $S_x = \gamma Z_x S_H$. The value for the effective charge is obtained from Thomas-Fermi effective charge model:

$$\gamma = \sqrt{1 - \exp\left(\frac{-0.92v_1}{v_0 Z_1^{2/3}}\right)} \quad (2.1.J)$$

Here v_1 is the primary ions speed and $v_0 = e^2/(4\pi\epsilon_0\hbar)$ the Bohr velocity.

For hydrogen and helium primary ions this approximation works, calculating the stopping force with formula 2.1.G and using Lindhard's formula [37] for the Interaction function.

There is a deviation for energies below 1 MeV/amu and for SRIM stopping force calculations a correction function is applied for low energies.

For higher mass primary ions like silicon and oxygen the Lindhard formula calculation of the hydrogen stopping power with the effective charge scaling, provides good agreement with

experimental data for energies above 200 keV/amu, which is the energy range used for MeV SIMS experiments.

At lower energies, where nuclear stopping is dominant, electronic stopping is proportional to the primary ions speed, with the proportionality constant depending on the target material through its density. In Figure 2-1-1 the electronic and nuclear parts of the stopping force, as well as their sum, are shown for a Silicon primary ion hitting a Leucine target.

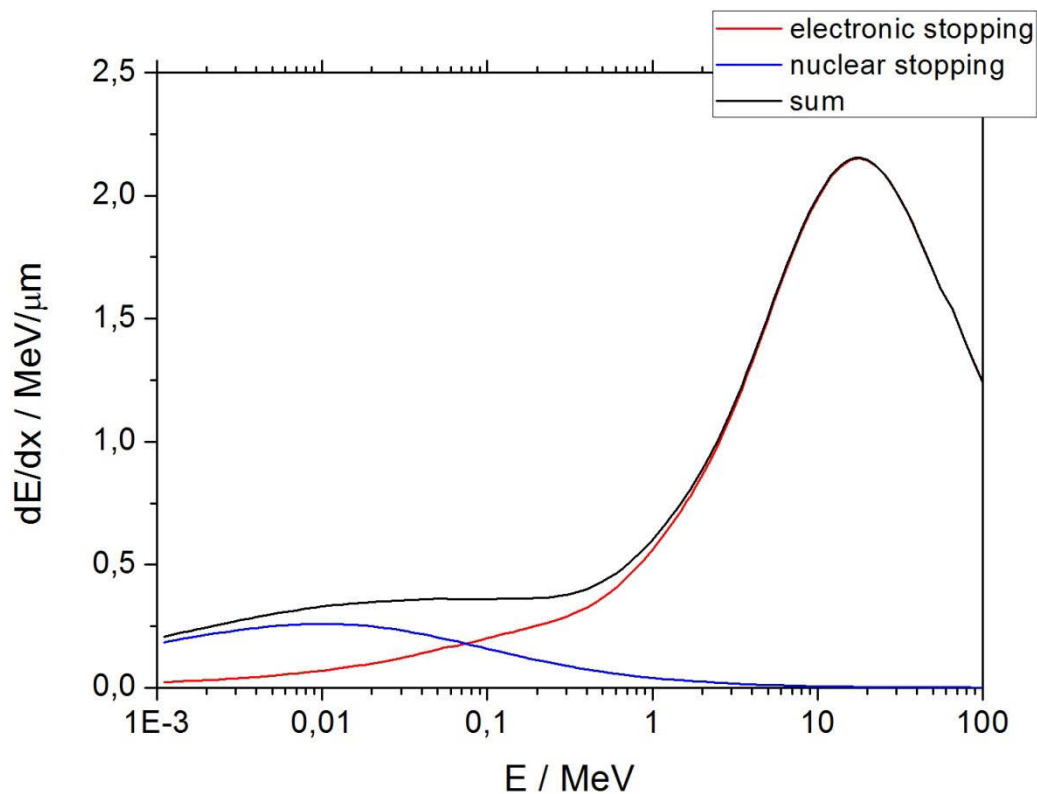


Figure 2-1-1: Calculated stopping power using SRIM [34] for Silicon in Leucine: In Red electronic stopping, in blue nuclear stopping and in black the sum of nuclear and electronic stopping.

2.2 The secondary ion desorption process

The prevalent process of secondary ion desorption after ion bombardment depends on the energy and mass of the primary ion. For the low keV energies used during keV-SIMS, desorption is caused by elastic collision processes (nuclear stopping) producing a collision cascade similar to billiard balls hitting each other. The primary ion enters the target material, depositing its energy through a number of collision processes until its energy is too low to displace a target atom, with the last energy being dispersed through molecular vibrations (phonons).

If at one point the collision cascade started by the primary ion reaches the target surface and the energy of the recoiled target particle is higher than the surface binding energy, a target atom or molecule is ejected.

For the higher primary ion energies used during MeV SIMS, the electronic energy transfer to the target atoms is the dominant process. It does not eject particles through nuclear collisions but through the transfer of the primary ions' energy to the electronic system of the target. Depending on the targets' material characteristics the energy gets distributed in different ways. Metals with high electron mobility and high heat conductivity favour radiative relaxation as opposed to atom displacement. Thus, sputtering is caused mainly by collision cascades caused by nuclear stopping. In insulators on the other hand, the low electron mobility and heat conductivity lead to the formation of a cylinder of heated up ion plasma around the primary ion track. This area is called 'infratrack' and it is an area of a high ionisation and excitation of the target atoms' electrons. Additionally, high energy electrons produced in the infratrack move further away from the ion track, forming an area of effect called the 'ultratrack'.

What happens after the track formation has been described by several theories [31]:

The transition state model assumes that the energy deposited in the ion track is used to populate intermediate states in the electronic system of the target that further on fill exothermic final states. Some of these final states are ejected particles. This model can be applied if the number of possible states is large and the energy difference between the states is small. It can predict the fragmentation patterns in mass spectra obtained and does not depend on the way the energy is transferred to the electronic system giving a possible explanation for the similar fragmentation patterns for keV and MeV SIMS.

The expansion model assumes that the molecules excited through electronic stopping expand and put pressure on the lattice cell or other molecules around them. This pressure puts the atoms of the surrounding molecules into motion if the competing effect of electron-electron collisions is not stronger.

In the excitation model the effect of the energetic excitation on a single molecule as opposed to the whole system is taken as the sputtering cause. An excited molecule can have electrons in a repulsive molecular orbital and if the molecules are at the surface, or the excitons migrate to the surface, desorption can occur.

The Coulomb explosion model can be applied if the electron mobility in the target is low. As the ionised atoms along the ion track are not neutralised the coulomb repulsion between the ions in an infratrack leads to an explosion. The repulsed atoms initiate a shockwave that moves through the target material with the speed of sound. If the energy of this wave is high enough at the target surface it leads to desorption of secondary ions.

Another approach is the thermal spike model [38]. It assumes that temperature in the cylinder of molten material formed around the impinging ions track can be described through a Gaussian function:

$$\Delta T(r, t) = \frac{gS_e}{\pi \rho c a^2(T, t)} \exp\left\{-r^2/a^2(T, t)\right\} \quad (2.2.A).$$

Here $\Delta T(r, t)$ is the temperature increase after the primary ion impact at point r and time t , S_e is the stopping force of the ion, g is the share of the stopping force deposited in the thermal spike, ρ the density, c the specific heat of the target and $a(T, t)$ is a material parameter. It is defined to be $a(T, 0) = a(0) = \text{constant}$. Melting occurs if the temperature T which is the sum of the temperature increase ΔT and the target temperature T_{tg} , is higher than melting temperature of the target T_m : $T = \Delta T + T_{tg} > T_m$. The evolution of the thermal spike depends on the material characteristics of the target. If it reaches the surface desorption of molecules can occur if the temperature is still high enough. The secondary ion yield Y is then proportional to the integral over the surface of the temperature, the surface binding energy U and the probability for the formation, survival and detection of the secondary ions P_i :

$$Y = \text{const} \times \sum_i \iint P_i(t, T) \times \exp\left(-\frac{U}{k_B T}\right) r dr dt \quad (2.2.B).$$

E.M. Bringa and R. E. Johnson [39] propose a combination of the Coulomb explosion and thermal spike model as two manifestations of the same process. The Coulomb explosion leading to thermal spike as the ion tracks molecules are set into motion.

Their molecular dynamics simulations result in a dependence of the yield on the stopping force in the second order similarly to the thermal spike model, the difference being the distribution of the energy in the sample through not only thermal diffusion but also a shockwave. The authors of the paper state that the process of desorption is thus understood and the new questions to investigate now is the ion track formation and structure regarding the time before the coulomb explosion in order to predict the intensity of the explosion.

It is evident though, that more precise secondary ion yields from experimental data are needed to verify the theory as well as to gain further insight in the coulomb explosion process.

Observed sputtering yields have shown a dependence on the stopping force $\left(dE/dx\right)^n$ with $n \in [1..3]$ [31]. Additionally, they show a branching for identical stopping forces depending on the primary ion velocity, the velocity effect. Secondary ion yields are higher for the slower primary ion if the stopping force is equal. An explanation for the velocity effect is the lower energy density in the ultratrack formed by the δ -electrons as these electrons have a higher velocity themselves if excited by faster primary ions. Their energy gets distributed to a wider area, even though dE/dx from the primary ion is the equal. The resulting lower energy density then leads to fewer secondary ions desorbed.

3 Experimental Setup

In this chapter, only the basics of the facility used to perform secondary ion mass spectrometry with an MeV energy ion beam will be discussed, for the other mass spectroscopy techniques the reader may consult the references provided in the introduction. Further on, the setup will be described as it existed at the start of the author's stay at the RBI. Changes that were done afterwards will be described in chapter 4.

As explained in the introduction, secondary ion mass spectroscopy employs bombardment by ions to induce desorption of particles from an analyte. Since the early days of SIMS many different types of primary ions have been used, ranging from alpha particles emitted by radioactive sources [30] to big clusters of thousands of atoms, with the most recent development being metallic MeV cluster ions [40]. Each type of primary ion has its advantages. Low energy ions can be provided by a small tabletop source and can be focussed down to a few nanometres. High-energy ions, on the other hand, need more complex machinery that can fill up an experimental hall of hundreds of square meters surface area but provide superior secondary ion yield, especially for high mass secondary ions, and the ability to extract the beam into air. At the Ruder Bošković institute (RBI) elemental ions with a kinetic energy in the MeV range are used.

Any secondary ion mass spectroscopy instrument consists of three main parts: The ion source, the sample chamber and the mass spectrometer. The following chapter will explain the construction and functionality of these parts.

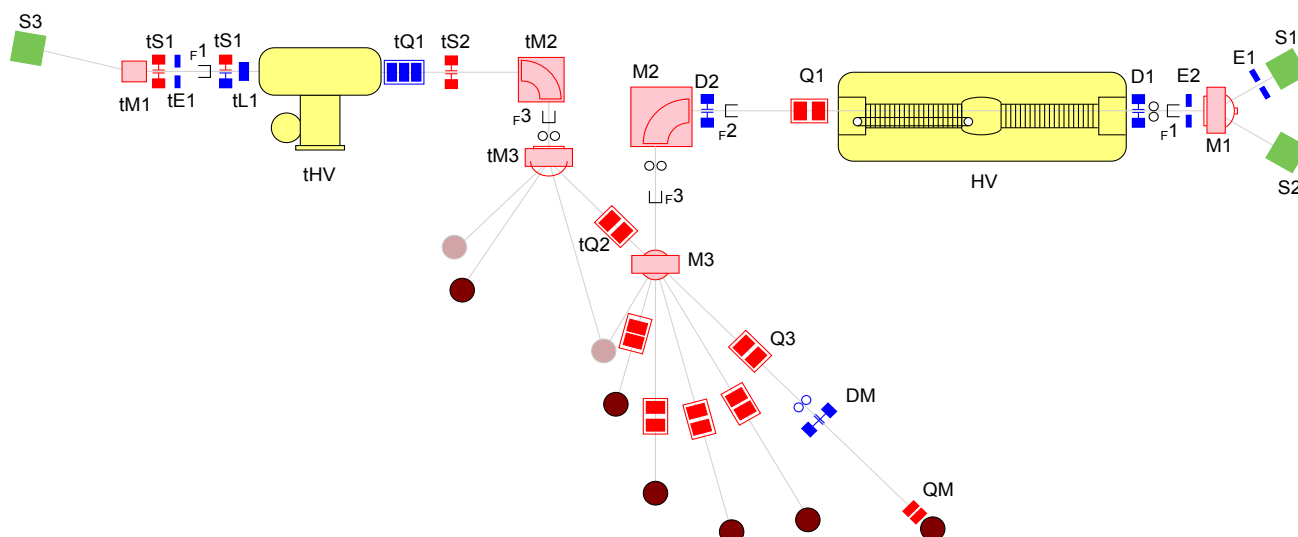


Figure 3-1: Setup of the beamlines at the Ruder Bošković Institute (RBI) [41]. Shown in yellow are the 1 MV Tandetron accelerator (left) and 6 MV Van de Graaff accelerator (right). The ion sources are in green and the ion beam optic components in red.

3.1 Ion Source

The ion source used during the experiments presented in this thesis is a Multi Cathode Source of Negative Ions by Caesium Sputtering (MC SNICS) from Pelletron [42]. It is a sputtering source, which means the same process used for SIMS, desorption of ions from a sample through ion bombardment is used to produce the primary ions for the experiment. Keeping this in mind the name secondary ion mass spectrometry could be changed to tertiary ion mass spectrometry (TIMS) for this type of setup.

Figure 3-1-1 shows the schematic of the ion production process: It starts with the heating of a caesium reservoir providing caesium atoms that move into the source. The sputtering targets in the source are cooled which leads to condensation of a part of the caesium gas at its surface. Another part of the caesium comes into contact with the conical tungsten ioniser and turns into positively charged caesium ions. Due to the electric field in the source chamber these ions get accelerated onto the cathode and sputter away particles from the target. The caesium deposited on the target surface provides electrons to form negative ions with the material that gets desorbed from the sputtering target. These are the primary ions that get extracted into the tandem accelerator.

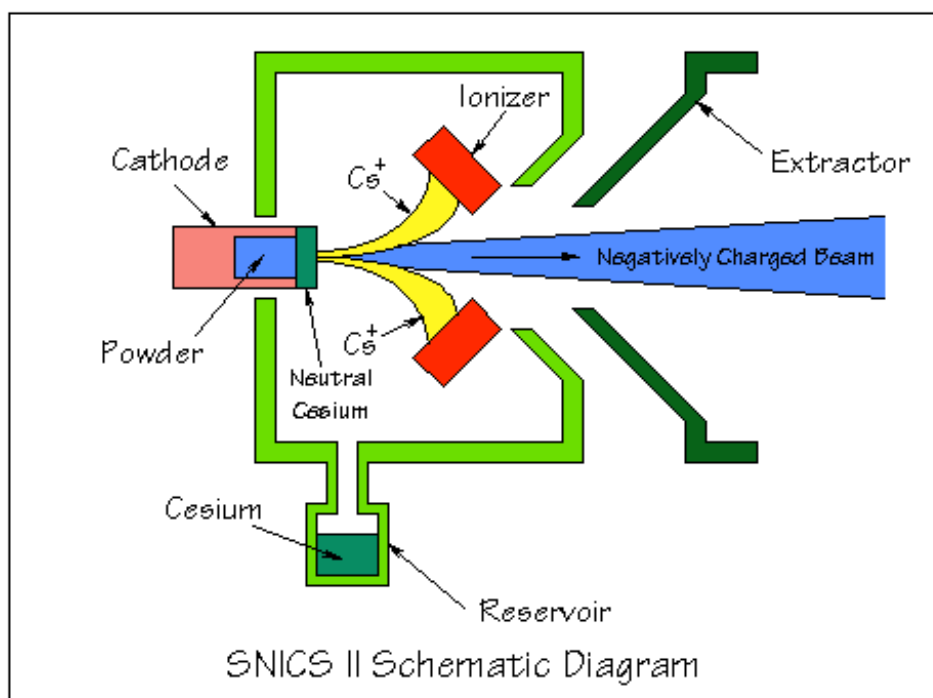


Figure 3-1-1: SNICS source [43] - The Caesium reservoir is heated and produces caesium vapour. Some of it is deposited on the primary ion source which is also a cathode, and some is ionised on an ionizer. The now positive Caesium ions are then accelerated to the cathode to sputter of particles from the cathode.

The type of primary ion that can be produced is limited by the fact that they need to carry a negative charge [44]. For low electronegativity atoms the Caesium layer on the cathode alone is not enough to produce a sufficient number of anions. In this case molecular ions are used in the first part of the tandem acceleration process. Preferably hydrides are used as they will leave most of the kinetic energy with the desired primary ion after separating in the accelerator.

The achievable secondary ion yield from MeV SIMS increases with the mass of the primary ion used because the stopping force maximum increases with the mass. A gold primary ion will produce more secondary ions than a helium primary ion if used with a kinetic energy close to its stopping force maximum. Due to the limitations of the beamline oxygen and silicon primary ions were used in the RBI facility. The cathodes to produce these ions are made of pure silicon and LiO_2 .

3.2 Ion transport system

All primary ions have to be transported into the sample chamber and focussed on the analyte, regardless of the type of primary ions used. The elements of the transport system, ion beam optics, are similar for all SIMS setups and include electrostatic deflectors, electromagnetic lenses, beam defining slits and analysing as well as switching magnets.

Ion optic elements can be divided into two groups of devices using either the Coulomb force or the Lorentz force to change the ions path in the beamline. As the Lorentz force is proportional to the speed of the ion it is more effective than electrostatic beam optics at the high energy part of the beamline.

3.2.1 Electrostatic optics

There are three types of ion optics at the RBI using the Coulomb force: electrostatic deflectors, gap lenses, including the Einzel lens, and electrostatic quadrupoles.

Electrostatic optics can be found mainly at the low energy part of an accelerator facility as with the high voltages necessary to change the paths of MeV ions in the high energy part of a beamline, electromagnetic optics are more useful.

Electrostatic deflectors consist of two plates, isolated from each other with a potential difference between them. Their main purpose is changing the direction of the ion beam. They are used for beam steering, i.e. to optimise the beam transmission through the beamline, and to deflect the beam in a beam chopper.

The deflection from the beam axis is

$$y(x) = \frac{qU}{4dE_{kin}} x^2 \quad (3.1.1.A)$$

and the change of direction

$$\dot{y}(x) = \frac{qU}{2dE_{kin}} x, \quad (3.1.1.B)$$

with x the length of the deflector, q the charge of the ion, E_{kin} its kinetic energy, d the distance between the plates and U the voltage applied. At the RBI MeV SIMS setup a chopper which has a maximum voltage of 2 kV on plates with length $x = 10$ cm and distance $d = 10$ mm between them is used. The length of the beamline from the deflector to the slits used for the chopping is 7 m. For an 8 MeV Si^{4+} beam this leads to a deflection of about 35 cm which is more than enough as the diameter of the tube the ion beam travels in is about 4 cm.

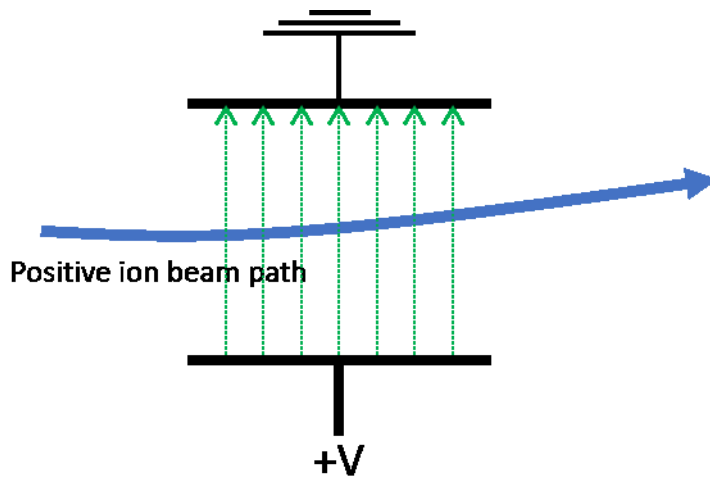


Figure 3-2-1-1: Electrostatic deflector and its working principle; in green the field lines.

One level of complexity higher is the gap lens, a coaxial structure of a combination of charged thin walled cylinders positioned one after another. The electric field in the gaps between the cylinders acts like a lens to ions passing through the gap lens. If there is only one potential difference in the lens, meaning every second cylinder has the same charge and it is an uneven number, it is called an Einzel lens coming from the German word Einzellinse - single lens. The Einzel lens focuses the ion beam while the ions kinetic energy stays the same.

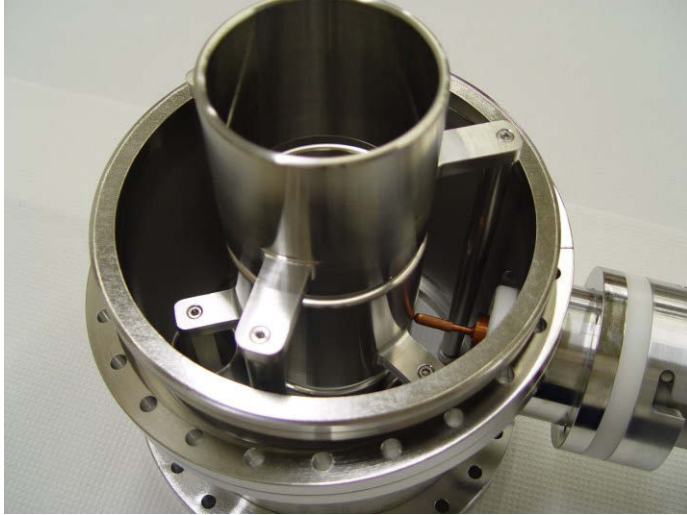


Figure 3-2-1-2: Einzel lens top view

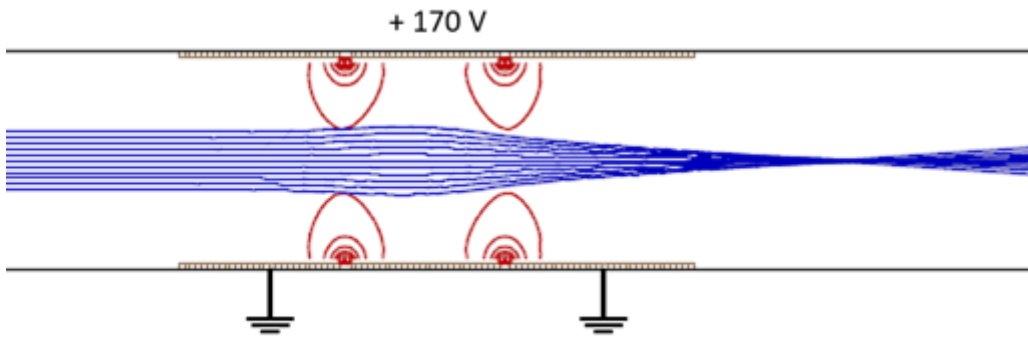


Figure 3-2-1-3: Focusing principle of the Einzel lens shown through a SIMION [45] simulation. In red the electric field lines and in blue the beam profile. The cylinders left, and right are grounded, while the centre one is shorter in length and on a positive potential.

To achieve a focussing effect the centre cylinder has to be shorter than the others. There is no simple formula for the focal length of an Einzel lens. Instead the focal length can be calculated by solving the ray equation [46]:

$$\frac{d^2\rho}{dz^2} + \frac{3}{16} \left(\frac{\Phi(r,z)'}{\Phi(r,z)} \right)^2 \rho = 0 \quad (3.1.1.C)$$

$\Phi(r, z)$ is the axial potential function and $\rho = r\Phi(r, z)^{1/4}$ with the coordinates along the beam paths r and z .

The third electrostatic ion optic device used at the RBI is the electrostatic quadrupole. It is formed by 4 hyperbolic electrodes positioned in a cylindrical symmetry (see figure 3-1-1-4).



Figure 3-2-1-4: An array of electrostatic quadrupoles [47], here in the common configuration of three in a row to focus in x and y direction.

The electrical field formed in such a configuration with $x=y=0$ in the centre axis of the beam line is:

$$E = -\frac{2U_{quad}}{d^2} \begin{pmatrix} x \\ 0 \\ 0 \end{pmatrix} + \frac{2U_{quad}}{d^2} \begin{pmatrix} 0 \\ y \\ 0 \end{pmatrix} \quad (3.1.1.D)$$

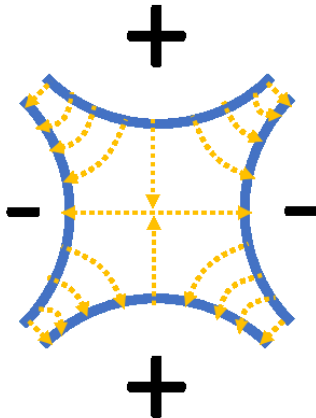


Figure 3-2-1-5: Electric field lines in an electrostatic quadrupole.

Figure 3-2-1-5 shows a schematic view of the electric field in an electrostatic quadrupole. With this configuration a positive ion will be focused in the y plane and defocused in the x plane. The focusing power depends on the electrodes' length, the separation between them and the voltage applied. By adding another quadrupole, forming a so-called doublet, an array that focuses in x and y plane is formed. The focussing power can be further increased by adding additional lenses to form a triplet (three quadrupoles in an array) or a quadruplet (four quadrupoles in an array). At the RBI 1.0 MV Tandetron beamline, a triplet setup is used.

3.2.2 Electromagnetic optics

In the majority of cases the ion beam bending strength of electrostatic elements is too small for MeV energy ions. Accordingly, electromagnetic optics are employed as they rely on the Lorentz force to change the direction of a moving charged particle:

$$F_{Lorentz} = q * v \times B \quad (3.2.2.A),$$

with the magnetic field B the velocity v of the charged particle and q its charge. The proportionality of the force to the velocity of the ion favours the use in the high energy part of a beamline compared to electrostatic optics.

The electromagnetic optic elements in the RBI accelerator facility can be separated into two groups: the magnetic quadrupole lens and the dipole analyser/switching magnet (DAM/DSM).



Figure 3-2-2-1: The dipole analyser and switching magnets used at the RBI. Visible in the front the dipole analyser magnet (DAM) of the 6 MV Van de Graaf (VDG) accelerator and in the back the DAM of the 1 MV Tandetron accelerator. On the left the dipole switching magnet (DSM) of the VDG accelerator and behind the VDG DAM the Tandetron DSM. Notable the 25.6° angle on the Tandetron DAM magnet for vertical focussing.

Figure 3-2-2-1 shows the two DAMs on the right that produce a homogenous magnetic field changing the straight path of the ions on a curved circular path. The radius r of the circular path is:

$$r = \frac{m_I \sqrt{\frac{2qU_a}{m_I}}}{q \times B_{analyser}} \quad (3.2.1.A)$$

with q the charge of the accelerated ion, the acceleration voltage U_a , m_I the mass of the ion, and $B_{analyser}$ the magnetic field in the electromagnet.

Looking at the DAM at the high energy side of the RBI's Van de Graaff accelerator which has radius r of 0.5 m, the required magnetic field strength B is around 1.5 T if one is using a 12 MeV Si^{4+} Ion beam.

The magnet at the RBI is limited to a field-strength of 2 T which is one of the limiting factors for the primary ions available for MeV SIMS, as higher rigidity ions that might produce a higher secondary ion yield cannot be injected into the ion microprobe system.

The basic DAM only focuses the beam in the horizontal plane. In order to also enable vertical focussing and thus improving the transmission of the analyser, an electromagnetic quadrupole (EMQ) is positioned in front of the DAM's entrance with a focus at the same point as the analyser.

Another way to provide focusing in the vertical plane is realized in the Tandetron DAM. The Tandetron DAM is a double focusing magnet which has angled input and output pole edges of 26.5° to the orthogonal of the beam axis. The resulting magnetic field focuses the beam on the same point in the vertical and horizontal plane.

Another important use of the dipole electromagnet is the dipole switching magnet (DSM), which deflects the beam into the desired beamline. It works the same way as the analyser magnet, only that the beam energy has already been selected. In some accelerator facilities analysing and switching magnet are one as the analysing magnet also acts as switching magnet.

The third application of the electromagnetic dipole is the scanning device with one example shown in figure 3-2-2-2 in front of an EMQ lens array.

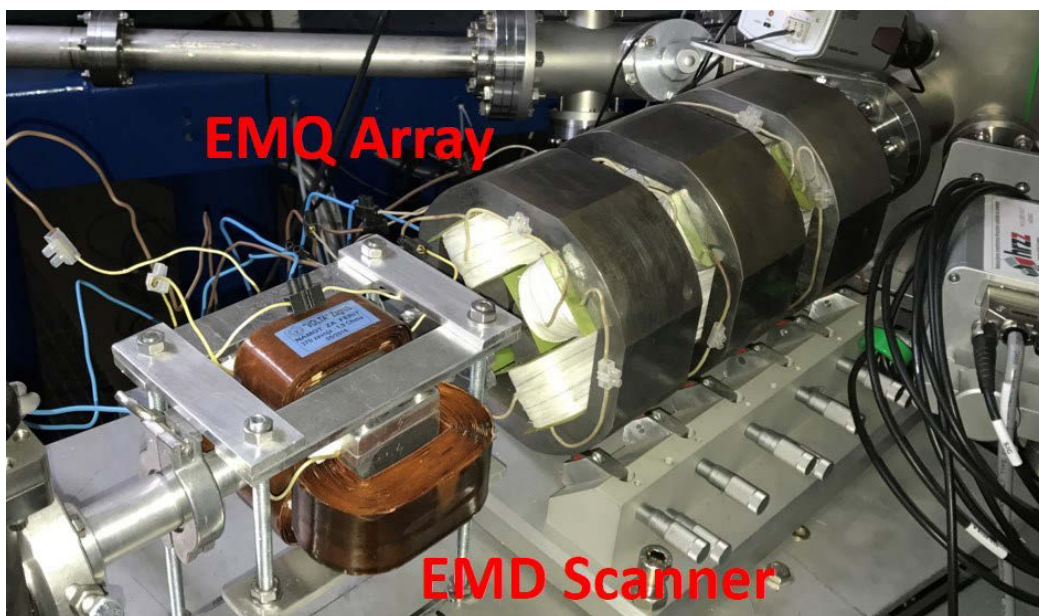


Figure 3-2-2-2: Electromagnetic dipole scanning device used at a recently developed RBI microprobe and an array of electromagnetic quadrupoles behind the scanner.

The dipole scanning device consists of two dipole magnets, each dedicated to deflection in one beam axis (x or y). A periodic current function, usually a triangle wave, is applied producing a scanning pattern. As the scanning speed can reach up to 100 Hz for such magnets, the use of conventional iron cores is problematic due to memory effects and low hysteresis soft ferrite is used instead of an iron core. In figure 3-2-2-3 the schematics of an electromagnetic dipole used for ion deflection are shown.

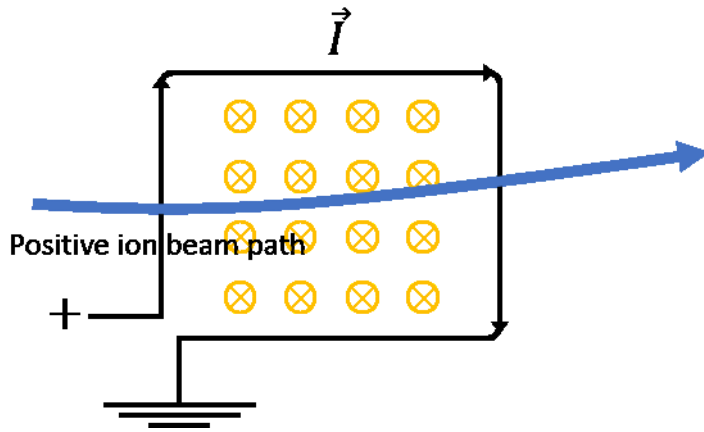


Figure 3-2-2-3: Schematics of an electromagnetic dipole. The magnetic field is denoted by the yellow arrows pointing into the picture plane.

The second type of the electromagnetic ion beam optics element employed in the accelerator facility is the EMQ. It functions similar to the electrostatic quadrupole only using the Lorentz force instead of the Coulomb force.

The resulting force field is similar:

$$F_{Lorentz} = -q \cdot v_{Ion} \cdot B_y \begin{pmatrix} x \\ 0 \\ 0 \end{pmatrix} + q \cdot v_{Ion} \cdot B_x \begin{pmatrix} 0 \\ y \\ 0 \end{pmatrix} \quad (3.1.2.B)$$

Again, the advantage of an electromagnetic optic is the proportionality of the Lorentz force on the ion's velocity, which makes it more efficient for high energy ions like the ones used for MeV SIMS.

The production of the EMQ relies on precision machining and there are always aberrations and deviations from the ideal field due to small errors in manufacturing.

3.3 Ion acceleration

The first step of ion acceleration is the source. A nozzle opposite of the sputtering targets (extractor) on a positive potential in the kV range accelerates the primary ions out of the SNICS chamber.

For the further acceleration up to a kinetic energy in the MeV range an EN Tandem Van de Graaff and a Tandetron accelerator are used:

The Van de Graaff high voltage generator is based on the mechanical transport of charge from the ground potential to a point called terminal where the charge is collected to create a high voltage potential. The medium of charge transport is a rotating belt which collects charge from the ground through a comb-like array of needles. At the terminal there is another needle array that collects the charge from the belt and adds it to the charge already stored in the terminal. Step by step the voltage is increased and can increase to the point where the potential difference is high enough for sparks to occur between the terminal and the housing of the accelerator.

The terminal voltage that leads to sparks depends on the gas surrounding the terminal. Normal air provides ionised channels for sparks to easily, so special isolation gases are used, i.e. N, CO₂ or SF₆. Additional to this limit of the achievable voltage on the terminal, there is a current flowing away from the terminal, which counteracts the charging from the belt. This current can be regulated through changing the distance between an electrode called the corona and the terminal. Additionally, the voltage on the terminal is regulated through the current flowing through the needle array at the ground potential side (the up-charge). The lower the current here, the lower is the voltage on the terminal. Nominally, for the EN Tandem accelerator of the RBI, the maximum voltage on the terminal is 6 MV, although operation at that voltage is not stable due to frequent sparks.

The actual acceleration can be separated into two steps. First the negative charged primary ions move onto the positively charged terminal. Inside the terminal a gas called stripper gas strips electrons of the primary ions turning them into positive ions which are then accelerated away from the positive charged terminal.

The potential field in the accelerator tube is formed along an array of resistors that connect the terminal to both ends of the accelerator. A part of the total voltage between terminal and ground drops over each resistor forming a homogeneous acceleration field in the accelerator ion tube.

The charge of the positive ions produced in the terminal is always distributed around the equilibrium charge state, the most prevalent charge of an ion after passing through a path length in a medium above a characteristic length. A working estimation to determine the

equilibrium charge q_{eq} for a particle with the atomic number Z_1 and the velocity v_1 is the Tomas-Fermi effective charge model from chapter 2:

$$q_{eq} = Z_1 \left[1 - \exp \left(- \frac{0.97 v_1}{v_0 Z_1^{2/3}} \right) \right] \quad (3.3.A).$$

It compares the velocity v_1 of the particle to the Bohr velocity $v_0 = e^2/(4\pi\epsilon_0\hbar)$.

In actual operation using stripper gases the equilibrium charge is slightly lower than in the Tomas-Fermi effective charge model. The gas density has an influence and electron capture processes in low pressure gasses shift the equilibrium charge down. On the other hand, if foils are used for electron stripping the opposite happens and the equilibrium charge is slightly higher than calculated. This shows an influence of stripping medium density which is not present in the Tomas-Fermi model.

The other RBI tandem accelerator, the Tandetron accelerator, operates almost the same way as the EN Tandem. The only difference is the method of charging the terminal. Here a Cockcroft–Walton voltage multiplier [48, 49], that consists of a combination of diodes and capacitors, provides the high voltage. If an AC voltage is applied the voltage over the capacitor array is increased for each step in the “ladder” shown in Figure 3.3.1.

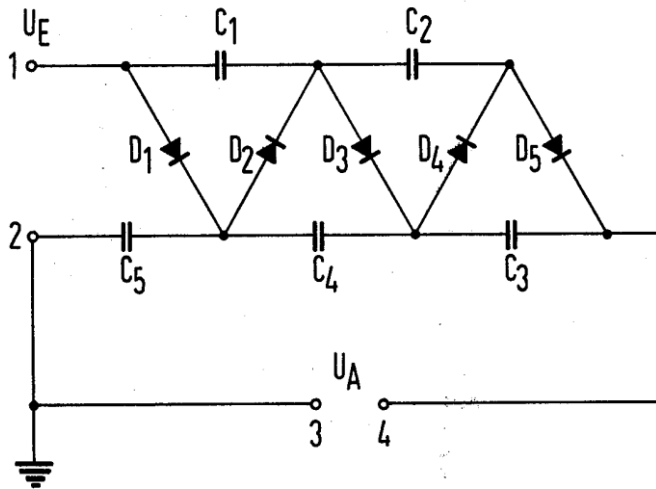


Figure 3.3.1: Schematics of a Cockcroft–Walton array [49]. An input voltage U_E can be used to produce an output voltage $U_A \gg U_E$.

As one can see the Cockcroft Walton voltage multiplier consist of capacitor-diode sets each adding $2 U_E$ to the voltage U_A . In Figure 3.3.1 there are five voltage multiplying cells leading to an output voltage of $10 U_E$. By adding more cells, the output voltage can be increased further.

The impedance of the electronic components and of the isolation gas in the accelerator currently set a limit of 4 MV to voltages achievable with Cockcroft Walton voltage multiplier. In the RBI Tandetron accelerator up to 1 MV terminal voltage can be realised.

3.4 Microbeam setup

A key element of the RBI MeV SIMS setup is the microbeam setup. It uses combinations of two or more electromagnetic quadrupole (EMQ) lenses to focus the ion beam onto a micrometre and sub-micrometre sized spot. Each combination of EMQ lenses has its own distinct advantages and disadvantages. They are compared by their demagnification D which is the quotient of the spot size σ_1 before the lens divided by the spot size σ_2 after passing through the lens. D and σ are vectors as EMQ demagnification is not isotropic.

$$D_{x,y} = \frac{\sigma_{1x,y}}{\sigma_{2x,y}} \quad (3.4.A)$$

The two-lens array (doublet), being the cheapest and simplest variant, provides an asymmetric and relatively low demagnification (e.g. $D_x=40$, $D_y=10$). The magnification can be increased with the addition of a third lens, forming the triplet-setup. If it is run in the high excitation mode, meaning the focus of the first EMQ is inside the EMQ array, an increased demagnification of e.g. $D_x=80$; $D_y=20$ can be achieved. Still the magnification will be asymmetrical. A fourth lens forms what is commonly known as the Russian quadruplet configuration, which provides a symmetrical but weaker demagnification (e.g. $D_x=21$; $D_y=21$) [50] .

Regardless of which number of quadrupoles is used, the ability to reach a small beam diameter depends on a number of factors:

- The energy stability of the accelerator - A huge variation of beam energy with constant focussing parameters (currents on the electromagnetic quadrupoles) leads to increase of the beam spot due to chromatic aberration.
- Vibrations in the beamline - Vibrations of the optical elements (slits, dipoles and quadrupoles) will induce changes in the beam paths increasing the spot size. Vibrations of the sample holder will not change the spot size itself but will decrease the achievable resolution of the measurement.
- Stray electromagnetic fields along the beamline. They deform the quadrupole field and change the beam path.
- The geometry and precision of the machining of the EMQ lenses. Small asymmetries lead to deviations from the perfect quadrupole field (introducing e.g. sextupole or octupole moments).
- The alignment of the EMQ lenses with the beam passing as central as possible in each lens to avoid aberrations.

- The power and stability of the power supplies used for the focussing optics. Oscillations in the current of the EMQ coils will lead to oscillations in the electromagnetic field focussing the beam.
- Finally, the geometrics of the beamline limit the magnification, in particular the opening of the objective slit and the aperture, the distance between them as well as the working distance in the chamber.

The object slits at the RBI are made of tungsten carbide and can be moved separately for the horizontal and vertical direction by stepper motors. The maximum opening of the slit is 100 μm in each direction. Reducing the object slit size will decrease the spot size after the lenses but also the ion beam current.

The aperture slit is positioned 7 m from the object slit. It takes out the halo of the beam and the part of the beam with high divergence. Ideally the aperture slit is infinitely small turning the ion beam into a parallel beam before it enters the EMQ lenses. This of course reduces the current and once again one must find the optimum parameters for each application in terms of ion microbeam current and beam size.

Low current techniques like STIM and MeV SIMS can work with a small slit opening and achieve much higher spatial resolution than high current techniques like PIXE.

The slit opening for MeV SIMS depends on the technique used and the necessities of the experiment at hand. As a high resolution below 5 microns is not needed during the chopped beam MeV SIMS yield measurements and the beam chopping reduces the current significantly, the beam defining slits are left in their most open position for these experiments.

For continuous beam transmission ion triggered MeV SIMS the beam current is increased by several orders of magnitude for the open slit position compared to a chopped beam. At the same time the current needed for any TOF MeV SIMS is still in the fA range. Accordingly, the beam defining slits can be closed almost completely and the current will still be high enough for MeV SIMS. This greatly increases the achievable spatial resolution for an MeV SIMS measurement.

The EMQ lenses are run in either doublet or triplet mode. In Doublet mode one power supply is connected to one EMQ lens each while the third lens is disconnected. In triplet mode the first and second EMQ lenses are connected to the same power supply in reverse polarity, while the third EMQ is connected separately. Currents up to 100 Ampere can be applied with high currents requiring cooling of the EMQs. The EMQs position and orientation can be changed by three screws on each EMQ, facilitating horizontal and vertical movement as well as turning of the EMQ around the beam axis.

While using the triplet setup a high and a low excitation mode of operation can be used. In the high excitation mode, the first EMQ that focuses in the high demagnification plane has its

focus in the centre of the following EMQ minimizing the influence of the second lens on the beam in this direction. For the low excitation mode, a lower current/magnetic field is used, and the focus is outside of the EMQ array.

The distance between the last EMQ and the sample holder (working distance), setting the focal length of the EMQ system, is 140 mm. It is mostly determined by necessities of the setup.

To keep the focal distance short, keeping the demagnification of the lenses high, the beam scanner necessary for imaging purposes is positioned in front of the quadrupoles in most of the microprobe beamlines. This is also the case at the RBI where an OM-40e dual scan coil driver powers the electromagnetic dipole scanners.

While this kind of setup shortens the distance between the quadrupole lenses and the sample, depending on how homogenous the field in the lens is, it can also lead to aberrations in the EMQ lens system because the ion beam is moved away from the lens centre before the focussing.

Figure 3-4-1 shows the setup for the RBI triplet setup with one line showing the low demagnification (x-z) plane beam profile and the other the high demagnification (y-z) plane.

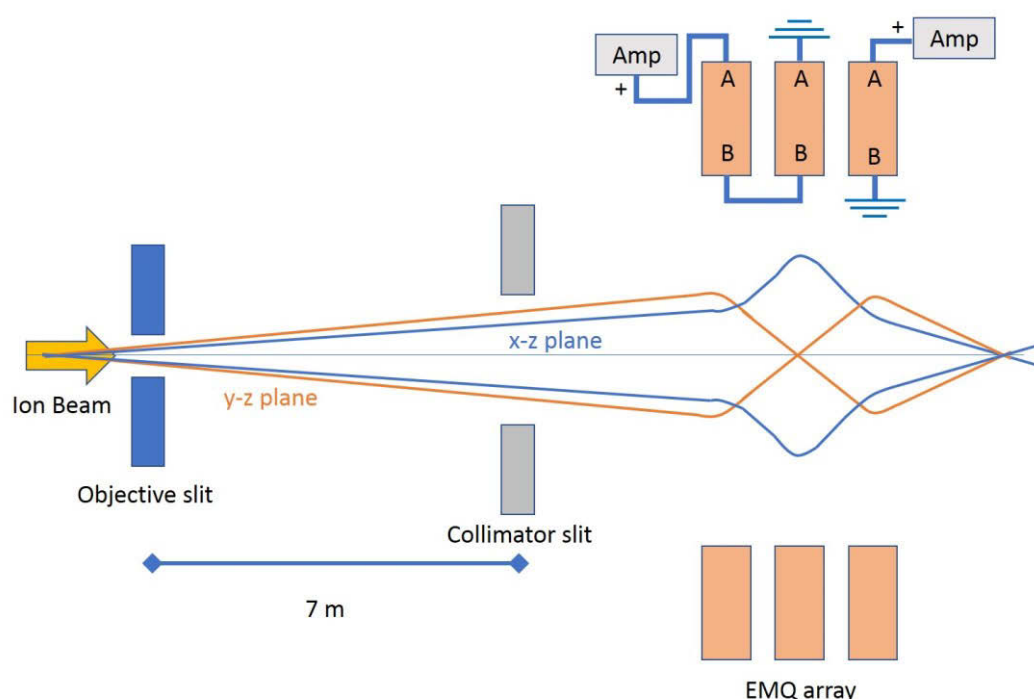


Figure 3-4-1: Schematics of triplet setup of a microbeam like it is used at the RBI. This kind of focussing is called high excitation mode as the beam has a focus point in the EMQ array. The first EMQ focuses the beam in the y-z plane onto the centre of the second EMQ which is poled reversely to the first EMQ, minimising the defocusing effect of the second EMQ in the y-z plane. The third EMQ again focuses the beam in the y-z plane. For the x-z plane the beam gets defocused in the first EMQ, then the beam is strongly focussed in the second EMQ. Finally, the last EMQ weakens the convergence in the x-z plane. The connections of the EMQ to the power sources are shown, with the first two EMQ run by the same power source but with the second EMQ in reverse polarity and the third EMQ run by a second power source.

A ray tracing simulation of the ion beam in a high excitation setup can be seen in figure 3-4-2. It shows how the beam already has a focal point in the EMQ array if the high excitation mode is used.

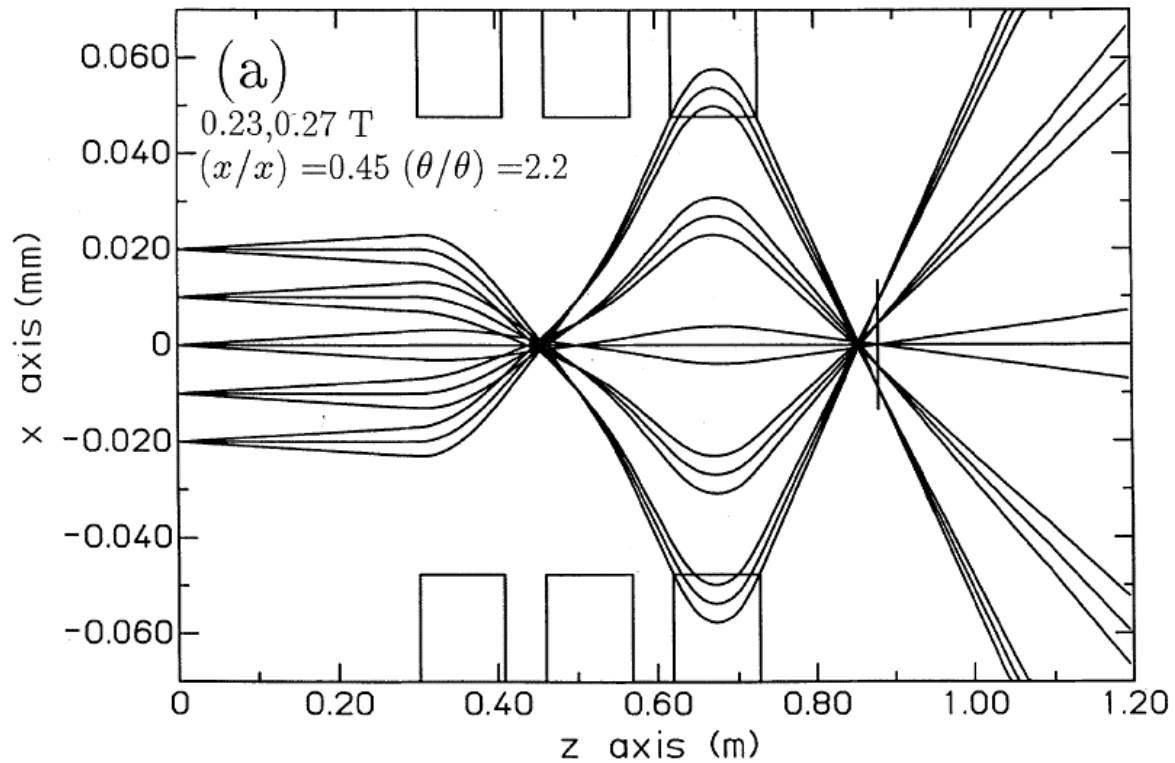


Figure 3-4-2: Ray tracing simulation of a triplet setup using high excitation mode [51]. The beam has its first focal point in the EMQ array.

3.5 Sample chamber

The RBI nuclear microprobe sample chamber is a spherical design. It is equipped with a Pfeiffer vacuum HiPace TC 400 turbo pump and can achieve 10^{-7} mbar pressure in the chamber. Samples are introduced into the chamber through a load lock manipulator from a small sample exchange chamber while the sample holder itself can be moved in the x, y and z directions and the angle along the x-axis (the horizontal axis, orthogonal to the beam direction). Semiconductor detectors for RBS, NRA and PIXE as well as the TOF mass spectrometer are positioned facing the sample holder front. STIM detector, signal feedthroughs, viewports and a Faraday cup are positioned behind the sample holder. For application of bias or charge measurements four SHV connectors (up to 5kV rated) and vacuum feedthroughs are available.

The sample can be seen through a video camera connected to a microscope with a normal and a magnified image. In front of the chamber are the three electromagnetic ion lenses for beam focussing and two pairs of electromagnetic dipoles scanning the beam over the sample

for mapping applications. The scan area can go up to 2 mm x 2 mm depending on the primary ion used. In front of the scanner coils are the newly installed RBS target and a Si-PIN diode connected to a stepper motor. Both are used for monitoring of the beam current (described in chapter 4).

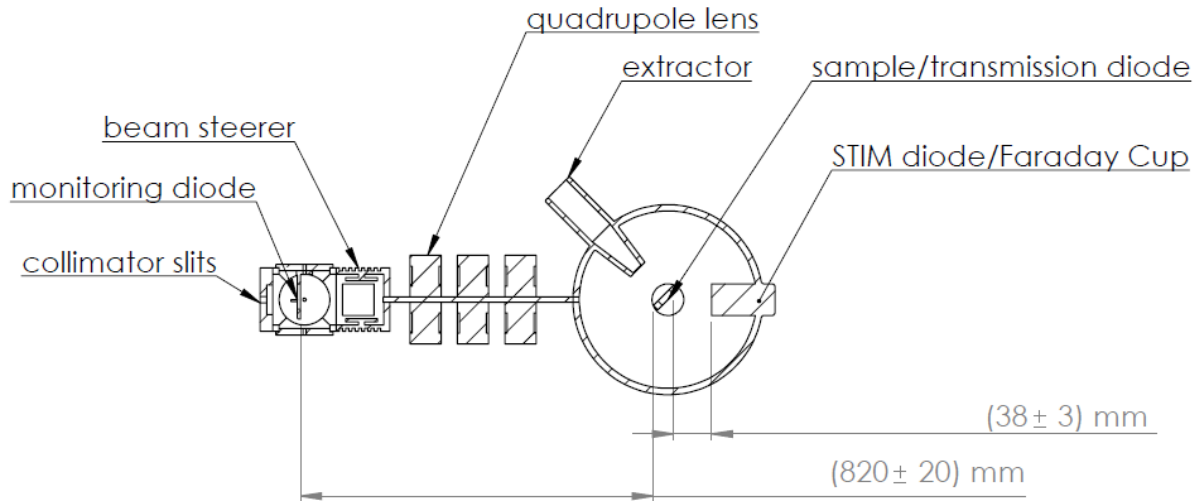


Figure 3-5-1: Sample chamber, electromagnetic lens array, beam scanning deflection plates and the beam monitoring mechanism

3.6 Mass spectrometer

There are four main types of mass spectrometer: The sector field mass analyser [52], the quadrupole mass analyser [53], ion traps [54] and the time of flight mass spectrometer (TOF MS) [55]. At the RBI microprobe system, a TOF MS is employed for mass spectrometry. It works on the principle, that particles with the same kinetic energy have different velocities depending on their mass and thus have different time of flights for travelling the same distance. To measure this time of flight exactly and reliably a well-defined start and stop signal is needed.

3.6.1 Start signal of the TOF measurement

As mentioned before the TOF measurement needs a well-defined start signal. The frequency of this start signal cannot be too high as a high intensity beam, which is used typically for different ion beam analysis techniques like PIXE, would produce so many start-signals and secondary ions that the mass spectrum would be continuous noise.

Ideally, the frequency of start signals should fit to the time window allocated for the TOF measurement in the data acquisition (DAQ) system. If the time window observed is 20 μs the frequency of the start signal should be 50 kHz, preferably appearing in constant intervals. If a low current beam is used this constant interval cannot be guaranteed and the process is of statistical nature. In this case the ion frequency or ion beam current must be lower than 50 kHz (about 4 fA) to assure there is only a minimum amount of overlap between the start signals and their respective time windows for the secondary ion detection. While the start signal itself can be filtered out if it appears in the measuring window of the TOF measurement, the resulting secondary ions cannot and will increase the noise in the mass spectrum.

This problem of the low current beam is avoided by using a pulsed beam [56] which was used for most of the measurements presented in this thesis. An almost always single ion pulse was generated in fixed intervals by moving the ion beam quickly over the collimator slit of the microbeam line.

The movement of the ion beam over said slit is facilitated through the application of a high voltage deflection potential between two parallel copper plates positioned 6 mm apart from each other. A MOSFET fast high voltage switch (Behlke Electronics GmbH, rise time 40 ns) changes the potential on one of the plates between + 1 kV and – 1 kV high (Voltage supplied by Bertan 205B-03R HV supplies) while the other plate is on ground potential.

Due to the fast movement of the beam over the slit some of the passes don't result in an ion passing through the slit. This results in a rate of ions arriving at the sample lower than the pulsing rate. The pulse rate was either 10 kHz or 20 kHz for the experiments presented in this thesis with an ion rate that reached up to 6-8 kHz for measurements with high primary ion intensity. Decreasing the deflection potential slows the movement of the beam over the slit and thus produces a higher rate of ions on the sample. It also increases the chance for multiple ion events in a single pulse even though the probability for this to happen remains low. Additionally, the time the ion beam needs to pass over the slit and thus the ion rate can be varied by the collimator slit opening.

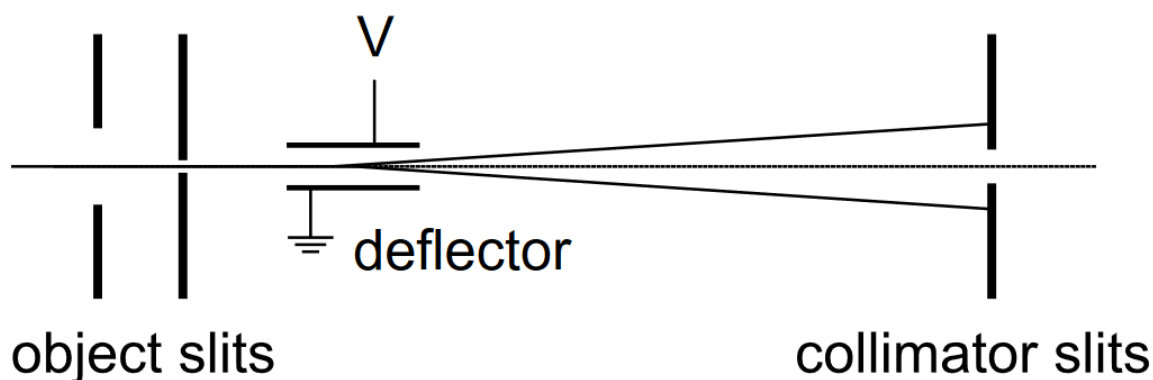


Figure 3-6-1-1: Schematics of the beam pulsing setup [56].

This pulse length of the beam is one of the parameters influencing the mass resolution. The width of the $m=1$ Da (Da - Dalton is a mass unit equal to 1 u (unified atomic mass unit)) peak can be used to determine an upper limit for the pulse length. The standard operation settings for the DAQ settings are a channel width of 5 ns for a 4096-channel spectrum which translates into a time window for the TOF detection of 20 μ s. The hydrogen peak is usually between one and two channels wide. Thus, the pulse width must be below 5 ns, considering the effects of the TOF tube and detection electronics on the mass resolution.

Another important difference between low and high deflection voltage is the halo of the beam. It is produced by scattering of ions in the beam line due to high pressure (i.e. 10^{-5} mbar compared to 10^{-7} mbar in the experimental chamber) and grows or disappears depending on the pressure in the beam line. At low deflection voltage this beam halo is transmitted through the slit and leads to increased noise in the mass spectrum. The halo effect is more pronounced for oxygen primary ions compared to silicon.

Apart from the beam passing over the slit one can also operate in a long pulse mode [16]. In this mode the beam stays on the slit for a set time - in the case of the JSI setup presented in [16] between 50 ns and 200 ns. This produces much longer pulse lengths and leads to the beam being in the chamber when the pulsing mechanism is not used. It can be used if the ion beam current is low and good mass resolution is not needed. Additionally, it needs one less HV supply and is more economical which might be of interest for some laboratories.

3.6.2 Stop signal of the TOF measurement

The stop signal for the TOF measurement is produced by the secondary ions desorbed through primary ion impact. The TOF is determined for the passage through a field free drift region in the TOF MS drifting tube. The kinetic energy of the secondary ion in this field free drift tube is determined through the acceleration of the particle in the electric field between the sample (-holder) and a steel extractor nozzle at the entrance of the drift tube. At the end of the drift tube the ions hit a multi-channel plate (MCP) detector producing the stop signal for the TOF measurement.

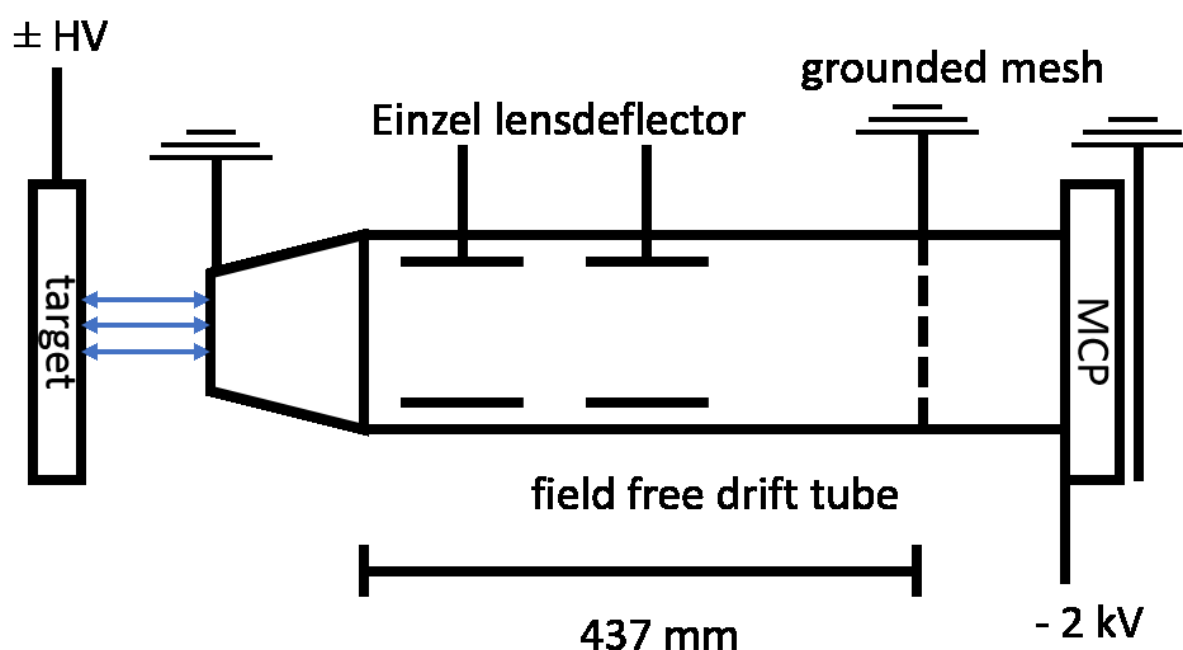


Figure 3-6-2-1: TOF tube schematics; inside the tube are deflector plates and an Einzel lens. Both are not in use currently. The TOF-tube is grounded while the target is charged to produce an accelerating electric field for the secondary ions.

The MCP detector [57] (figure 3-6-1) at the end of the chamber consists of an array of thousands of parallel micro channels with a diameter in the micrometre range. The channels' walls are coated with a material with a low ionisation potential to produce a high number of secondary ions from each impacting ion. All the channels are slightly angled to the incoming beam direction (up to 12°) so an incoming ion creates secondary electrons that are reflected to the opposite channel wall and back various times to achieve a high signal amplification. A typical channel with a ratio of channel length to channel diameter of 40:1 can achieve a signal multiplication of more than 10000 [58].

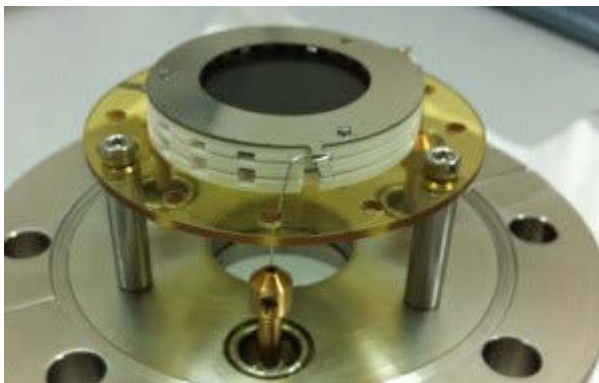


Figure 3-6-2-2: An example of an MCP mounted on a flange as offered by GIDS-GmbH [59].

Theoretically, any particle detector like a semiconductor detector or a proportional counter [60] could be used to generate the stop signal for the TOF measurement. Still the MCP detector has advantageous characteristics:

- The timing characteristics (TOF measurement resolution) depend on the rise time τ of a signal produced for the stop signal. For MCPs τ is in the picoseconds range [57] as opposed to nanoseconds for gas detectors and semiconductor detectors [61].
- The signal amplification in the MCP detector: The charge produced by an impinging ion can be amplified up to 10000 e while it is only about 1000-2000 e for a semiconductor detector with a band gap of 4 eV and a secondary ion energy of 5-10 keV after acceleration.

Another important aspect of the usage of an MCP during mass spectroscopy has been investigated by Gilmore et al [62]: The efficiency of an MCP increases with the acceleration voltage applied. A voltage of 20 kV for the impinging ions has been shown to be enough to provide an efficiency of close to 1 for all masses up to 4000 Da.

The MCP used at the RBI has two stages. A total potential difference of 2 kV is applied with a grounded mesh in front of the MCP entrance to provide a field free drift region in the TOF-tube. This potential accelerates the secondary electrons produced by the particles hitting the MCP entrance. The electrons are then collected in an anode and move into the preamplifier.

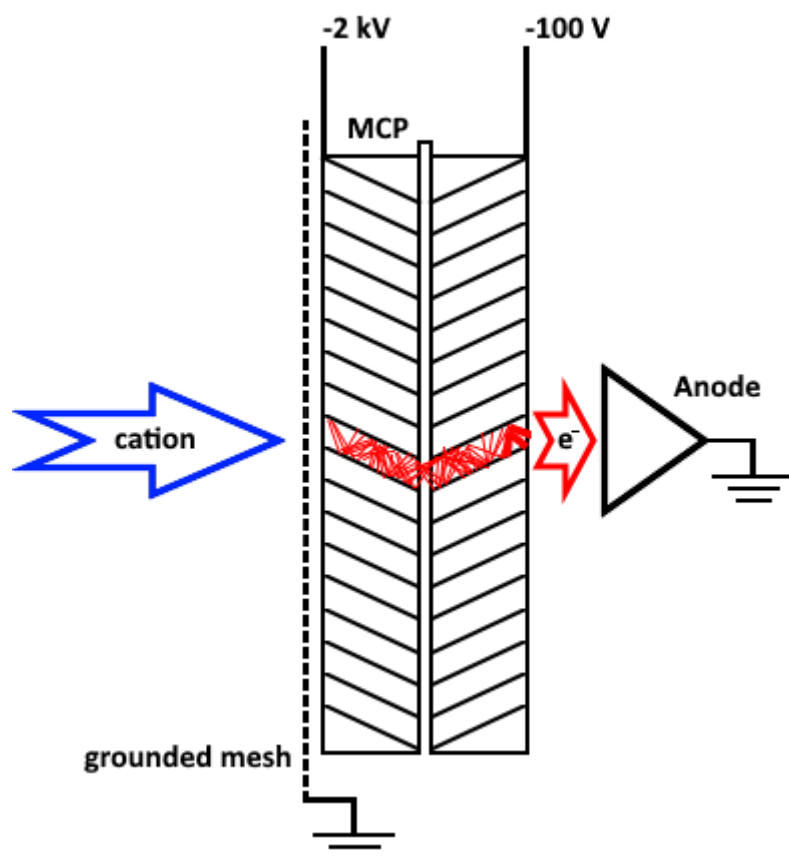


Figure 3-6-2-3: Sketch of the operating principle of the RBI MCP. The grounded mesh provided the field free drifting zone in the TOF tube. The incoming cations pass through the mesh hit the MCP detector walls where they induce an avalanche production of electrons that are collected by the grounded anode and move to the preamplifier.

In commercially available TOF spectrometers an acceleration potential of 20 kV is applied in the TOF tube. At the RBI the voltage is applied to the sample holder, introducing the challenging task to provide sufficient isolation and appropriate equipment to be able to put the sample holder on this potential. Using this Setup an acceleration potential of 8 kV has been tested but usually 5 kV are used. This means the efficiency of the detection system will strongly depend on the secondary ion mass, favouring the detection of low mass secondary ions. An investigation of this dependence is presented in [23] and in chapter 6.

3.6.3 Calibration of the TOF measurement

As all the charged particles are accelerated in the same electric field, they receive the same amount of kinetic energy

$$E_{kin} = \frac{1}{2}mv^2 = E_{pot} = qU \quad (3.6.A).$$

M is the mass of the particle, v its velocity, q its charge and U the potential difference or acceleration potential. After acceleration the charged particles enter a potential free tube where they fly into the particle detector at the end. The time of flight t for a particle with mass m through the distance s of flight in the potential free tube can then be calculated with:

$$t = \sqrt{\frac{ms^2}{qU}} = K\sqrt{\frac{m}{q}} \quad (3.6.B).$$

K which is made up made up of the setup parameters of the MS is the proportionality constant for the relation between the mass of a particle with charge q and mass m is and the square of the time of flight t:

$$\frac{m}{q} = Kt^2 \quad (3.6.C).$$

Formula 3.6.C shows that the TOF is not purely dependent on the mass of the particle measured but also on its charge. It is not possible to distinguish between a particle with mass m and charge q and a particle with mass $n \times m$ and charge $n \times q$ as they booth will have the same time of flight.

Additionally, to the simple second order dependence of the mass to time calibration, there is also a first and zero order dependence in the final calibration function. Both stem from the time delay t_0 between the start of the time measurement and the creation of secondary ions. The reason for this delay depends on the method of secondary ion and start signal creation. At the RBI two methods for the start signal are used: a beam chopping through periodical movement of the beam over a small slit and a start signal from the impact of the primary ion into a detector after passing through the sample.

For a chopped beam t_0 is the time the primary ion needs to fly from the slit to the sample plus the secondary ion creation time. In the second case it is the time of flight from the sample to the detector subtracted from the secondary ion creation time.

Theoretically this would provide a way to determine the secondary ion creation time, in the actual experiment the electronic components used to measure the time of flight of the secondary ion ((pre-)amplifiers, constant fraction discriminators (CFDs), cables, time to amplitude converters (TACs), measurement computers) make an exact determination of this time very difficult, no to say impossible.

Including t_0 the relation between the TOF and the mass over charge ratio is:

$$\frac{m}{q} = K \times (t - t_0)^2 = K \times t^2 - 2Kt_0 \times t + Kt_0^2 \quad (3.6.D).$$

Additional factors that influence the TOF are the initial velocity of the secondary ions and the added time for the acceleration of the secondary ion in the electric field between extractor and sample. The initial velocity of the secondary ion is variable and increases the uncertainty of the TOF measurement. It cannot be included in the calibration function. On the other hand, the time needed for secondary ion acceleration has influence on the mass-time calibration function by decreasing the K factor. Formula 3.6.C shows the possibility for ions with the same $\frac{m}{q}$ to interfere and appear in the same peak, but as can be seen in figure 3-6-2 most of the secondary ions detected in an MeV SIMS experiment have the charge $q = 1$. The peak of the protonated main molecule at 1179 Da appears in the mass spectrum of the organic compound Irganox 1010. If there would be a significant number of molecules with charge $q = 2$ or higher there must be peaks visible at the m/q of 1179/2, and 1179/3 but as can be seen there are no peaks

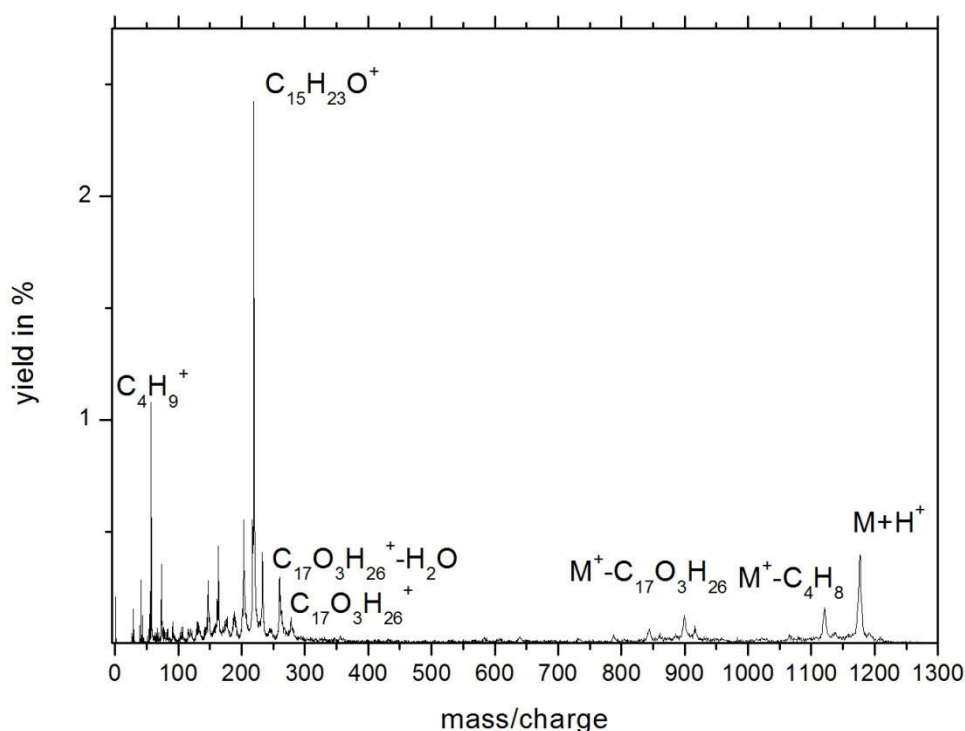


Figure 3-6-3-1: MeV SIMS spectrum of Irganox 1010 using 8 MeV Si^{4+} . The molecular peak is visible. Additionally, visible the molecule minus one of the C_4H_8 groups and minus one of the complete $\text{C}_{17}\text{H}_{26}\text{O}_3$ groups but no peaks at 589.5 Da or 407 Da which would represent double and triple charged Irganox 1010 molecule.

Accordingly, in this thesis a charge of $q = 1$ will be assumed and thus the x-axis will be labelled mass in Da.

3.6.4 Further possible improvements for an MeV SIMS

Several ways exist to improve a mass spectrometer's performance in detection efficiency and mass resolution:

- The addition of deflectors and other beam optic components within the flight tube may improve the transmission of the spectrometer.
- A longer drift tube increases the mass resolution, as the time separation of ions with different mass to charge ratio increases.
- Delayed extraction (DE) of secondary ions [63] to negate the effect of a secondary ion initial velocity distribution on the TOF measurement. The potential between TOF tube and sample is activated a short time after the ion production process. This leads to the ions that already have a higher momentum towards the TOF tube nozzle to be closer in the moment of field activation. Accordingly, they receive less acceleration in their way into the tube compared to secondary ions with the same mass over charge ratio and a lower initial velocity, decreasing the momentum difference for these particles.
- The reflectron setup using an electrostatic mirror [64, 65] to negate the initial kinetic energy difference between secondary ions with the same mass. Instead of applying less acceleration to ions with more kinetic energy (\rightarrow delayed extraction) the electrostatic mirror increases their flight path length compared to ions with the same m/q ratio and less initial momentum. The result is the same as for DE, decreased TOF spread for ions with the same m/q value.

3.7 Data acquisition

The data acquisition (DAQ) for the RBI MeV SIMS setup runs through Xilinx Virtex 4 Field programmable gate array (FPGA) card.

An FPGA card holds a customizable chip that can be designed to exactly fit the needs of an application. In contrast to normal programmable chip that cannot be modified, in the FPGA the actual connections between the transistors can be set. The results are higher computing speed and lower energy consumption for a given task.

The FPGA card is run with in-house developed software called SPECTOR [41, 66] that collects the measurement data. For chopped beam applications it also creates the switching signal for the beam chopping on the deflectors which is also the start of the TOF measurement. Once a secondary ion hits the MCP at the TOF tube end, the signal is sent through a fast timing amplifier, constant fraction discriminator and further amplifier that sets the signal height to a value acceptable for the FPGA card (running on 3.3 V logic) supplying the stop signal for the TOF measurement in Spector. For other (energy-) detectors the signal goes through pre-amplifier, amplifier and analogue to digital converter (ADCs) to the computer.

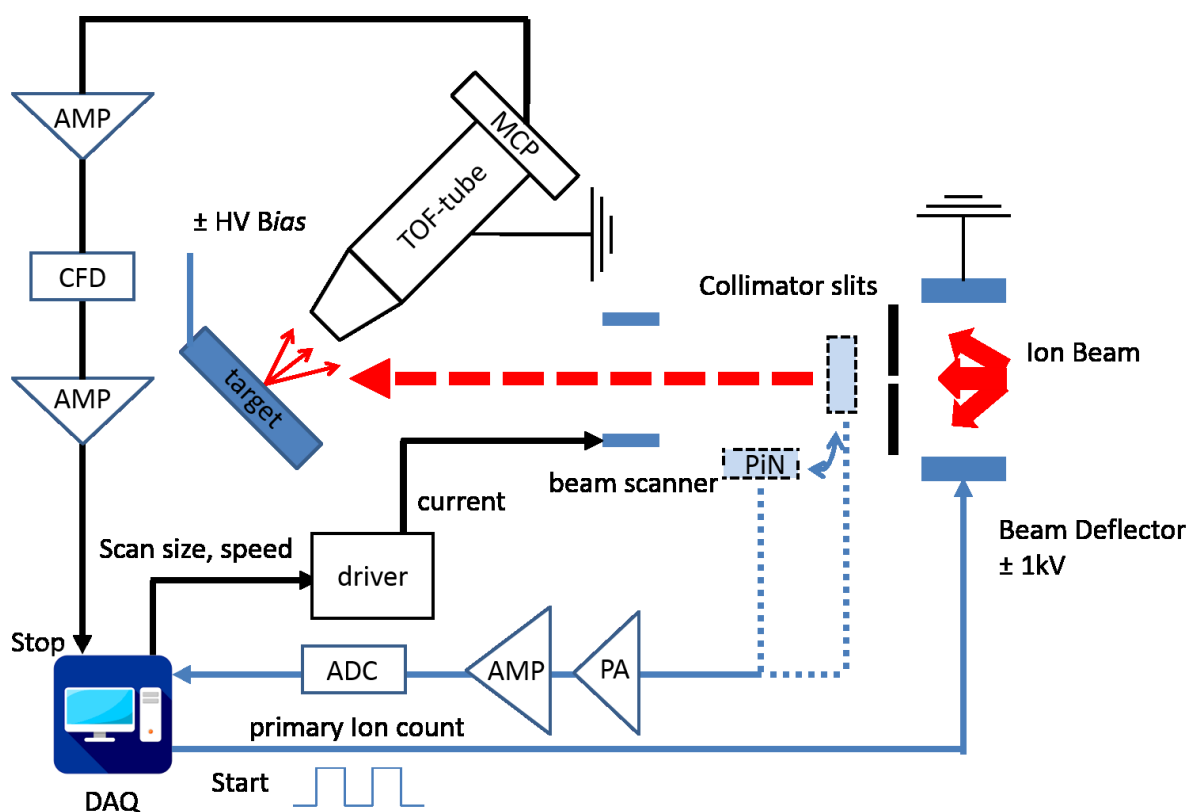


Figure 3-7-1: DAQ schematics for the setup used. Also included the connections for the ion beam monitoring explained in chapter 4-1. Incoming signals are the primary ion signal and the stop signal from the MCP. Outgoing signals are the start signal for the beam chopping and the scan size and speed for the beam scanner driver.

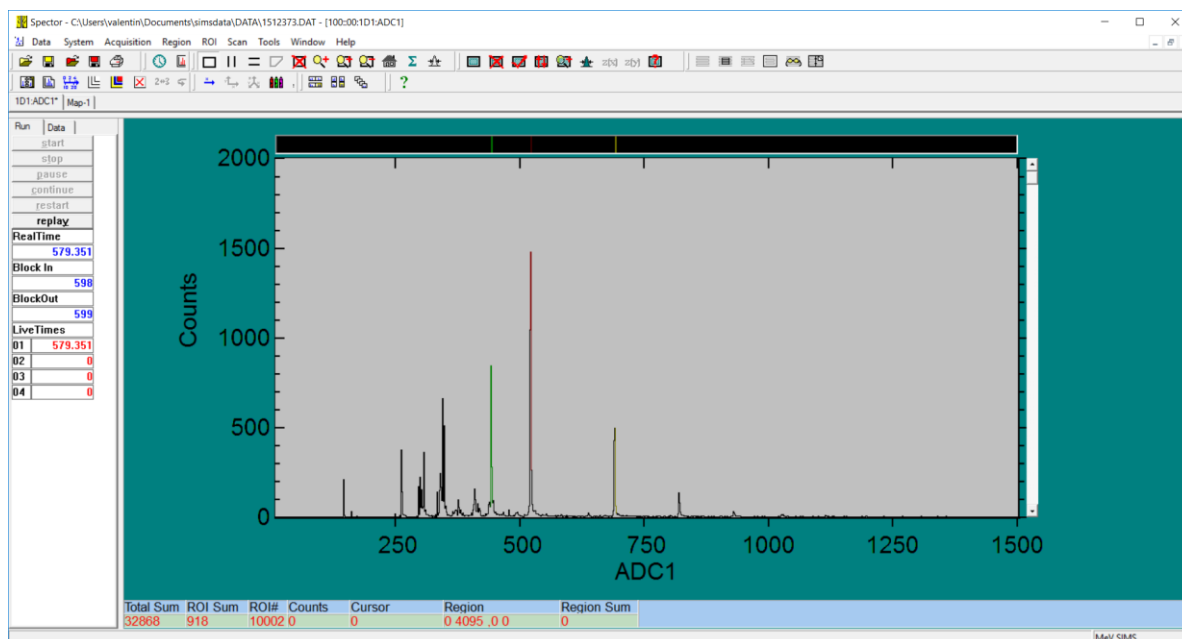


Figure 3-7-2: Visual Interface (VI) of the Spector program for spectrum acquisition.

4 Upgrades of the setup

Three significant upgrades to the original MeV SIMS setup have been realised and tested:

1. An ion beam intensity monitor, to watch the beam current during measurements.
2. A new type of glass capillary for future use in MeV SIMS and other IBA techniques.
3. A STIM detector mounted behind a sample deposited on thin carbon foil as an alternative starting signal for TOF measurements.

In the following chapters the upgrades will be described in detail.

4.1. Ion beam intensity monitor

As the main goal of this thesis is to gain more insight into the dependence of the secondary ion yield in MeV SIMS on different experimental parameters, an accurate measurement of the number of ions hitting the sample is needed. One way to do that is using a thin sample through which the primary ions can pass in order to be detected behind the sample. This solution complicates sample production, due to the fragility of thin samples and sets limits to the type of sample that can be used.

Therefore, it was decided to use a device that can measure the ion beam intensity periodically, intercepting the beam to estimate as accurate as possible the number of ions hitting the sample. The roughest approximation applied usually is measuring the current before the beam chopper and calculating through the chopping frequency and length, the number of ions hitting the sample [17].

The problem of that approach is to know the length of the time the beam is being transmitted through the slit (chopping length). It depends on the rigidity of the beam, the width of the slit and the deflection voltage used and can be approximated by the beam width of the hydrogen peak in a mass spectrum which indicates an upper boundary for the chopping length. As the peak width is the sum of the time of secondary ion creation, variations in time of flight, the error of the DAQ-System and the chopping lengths, the approximated beam current will be too high.

For the RBI setup the chopping frequency was set to 20 kHz, however usually the ion beam current was not high enough to provide 20000 ions/second for a 20 kHz chopping frequency. The chopped beam current can be measured with a detector in place of the sample before the measurement starts and in between. For a perfectly stable beam this method would be sufficiently reliable, but it can be safely assumed that this is not the case during real experiments, especially those performed at the RBI Tandem Van de Graaff accelerator. Periodical and random beam fluctuations appear and make it necessary to monitor the beam continuously.

A more accurate way is measuring the intensity of the chopped beam directly, with an ion detector inserted periodically in place of the SIMS target. This method sets a limit to the primary ion current, as a detector such as the Si-PiN diode can only withstand femto- and low picoampere currents long enough for realistic measurement times. For higher primary ion currents, it will be damaged quickly, which leads to decreased charge collection efficiency and energy resolution within a few minutes of measurement.

For high current ($I > 1 \text{ pA}$) beam applications, i.e. irradiation of the sample, the beam intensity is measured through indirect measurements by RBS or PIXE.

4.1.1 Mounting and movement of the ion beam intensity monitor

Beam monitoring at the RBI is performed by a Si-PIN diode of the type Hamamatsu S1223-01. The Hamamatsu S1223-01 is a low-cost detector which can be easily replaced once it has been degraded too much by the ion beam.

As ion beam current monitoring is also necessary for high current beams, an RBS target is fixed above the diode. The back scattered ions from the target are collected by another Si-PiN diode opposite of the target in an approximately 45-degree angle.

The setup can be seen in figure 4-1-1-1.

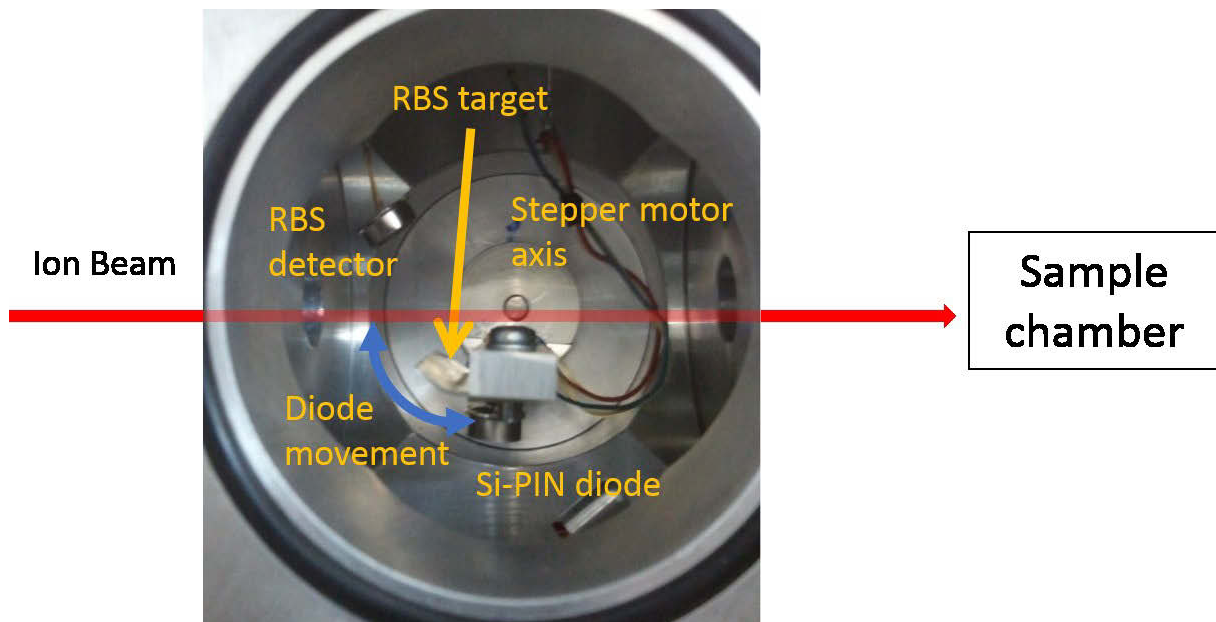


Figure 4-1-1-1: Ion beam monitor setup. Visible are the cables connecting the Si-PiN diode to the pre-amplifier. The diode itself and the RBS-target are mounted on an aluminium arm. The RBS-target consists of a steel plate with a gold layer evaporated on top.

In order to periodically measure the beam intensity, the detector has to be moved in and out of the ion beam. Due to the cables necessary for the detector a direct motor driving a simple rotation cannot be used for the diode holder. Instead a stepper motor supplied through a “Big Easy” stepper motor driver and controlled by an “Arduino Uno” microcontroller is used.

As a motor inside the beamline might cause complications with the cooling of the motor and vacuum graded motors are expensive and of high complexity, it was decided to mount the motor outside the beamline and use a rotary vacuum feedthrough. The model selected for the task is a 12 V 80mA Matsushita stepper motor which rotates 1.8° per step. The prices for these

mass-produced steppers are usually very low. The step size is important for positioning the detector in the beam. As it will be presented in the paragraph detailing the verification of the current monitoring method, our tests show the resolution is sufficient.

The second important value for a stepper motor is the torque it can provide. It determines how fast the detector can be moved in and out of the beam. This was well visible as the maximum speed of the movement depended on how far away from the stepper motor axis the diode was mounted. If the torque is too low to provide a set speed of movement, the motor loses steps, which makes periodical, precise movement between two points impossible. As the movement of the diode in and out of the beam introduces a slight error into the measurement, a future upgrade can include a higher torque motor. For the purpose of this investigation though other errors like the variation of the secondary ion yield were dominant and the power of the current motor was deemed sufficient.

The detector is placed in the microbeam line to intercept the beam axis immediately after the collimator slits (defining typically a $1 \times 1 \text{ mm}^2$ beam area) and prior to the scanning coils and focusing quadrupole triplet (Figure 3-5-1). With its sensitive area of $3.6 \times 3.6 \text{ mm}^2$, this diode (when well aligned) has 100% efficiency for all ions that enter the microprobe focusing system.

This vacuum feedthrough is particularly simple and inexpensive, it consists of a simple radial shaft seal (O-ring). Still no degradation of the vacuum could be measured along the beamline and tests have shown that 10^{-7} mbar pressure can be maintained. Influence of the possible stray magnetic fields (i.e. from the stepper motor coils) that may degrade microbeam focusing were not detected.

Thanks to the use of cost-effective solutions, the cost of the whole system is less than 1 % of the cost of a setup employing specialised equipment, while being equally reliable.

4.1.2 Calibration of the ion beam intensity monitor

During a typical MeV SIMS measurement using the described setup, the monitoring diode first measures the ion current for a time of 0.5 seconds. Afterwards it moves out of the beam and holds for 0.5 seconds before rotating back into the beam. As 280 ms are needed for the movement in and out, this time must be added for a total measurement cycle period of 1.28 s. Hence, the time the monitoring diode measures the beam intensity is not equal to the time the beam hits the sample. This, in addition with other possible effects like the beam shape and position on the Si-PiN diode as well as transmission losses along the way through the ion lenses (the distance between monitoring diode and sample holder is $820 \pm 20 \text{ mm}$), makes it necessary to experimentally determine a calibration factor that relates the number of ions detected by the Si-PiN diode to the number of ions that actually hit the sample.

In order to find this factor, a particle detector normally used for STIM is utilised. The detector, with an active area of 50 mm², is positioned 38 ± 3 mm behind the microbeam focal plane and in front of the Faraday cup.

A calibration is performed by hitting that detector instead of the sample when the monitoring diode has moved out and is not intercepting the beam. The calibration factor k is then determined as a ratio between the number of counts measured by the STIM detector and the number of counts measured by the monitoring diode. It is assumed that the number of ions hitting the STIM detector is the same as the number of ions hitting the sample.

For the high current measurement setup, the RBS signal is compared to the current collected from the Faraday cup at the end of the chamber. The Faraday cup is connected to a current integrator and a counter. At the end of the calibration measurement the number of ions per RBS count can be calculated from the charge collected during the measurement.

4.1.3 Validation of the beam intensity measurement

In order to validate the accuracy of the calibration factor determination, and its dependence on the position of the STIM detector relative to the assumed beam centre, the STIM detector was moved through the beam axis. To assure that the entire beam is always detected, the beam diameter must be small compared to the STIM detector diameter. With a 5 MeV Si⁴⁺ beam, the area of constant signal was wide enough to easily position the STIM detector in the beam axis. As beam divergence could be different in some circumstances, for each calibration measurement the correct position of the STIM detector needs to be determined. The same calibration test was performed for the Si-PiN diode and there also exists an area of constant signal big enough to reliably position the detector, so it catches the whole beam (figure 4-1-3-1).

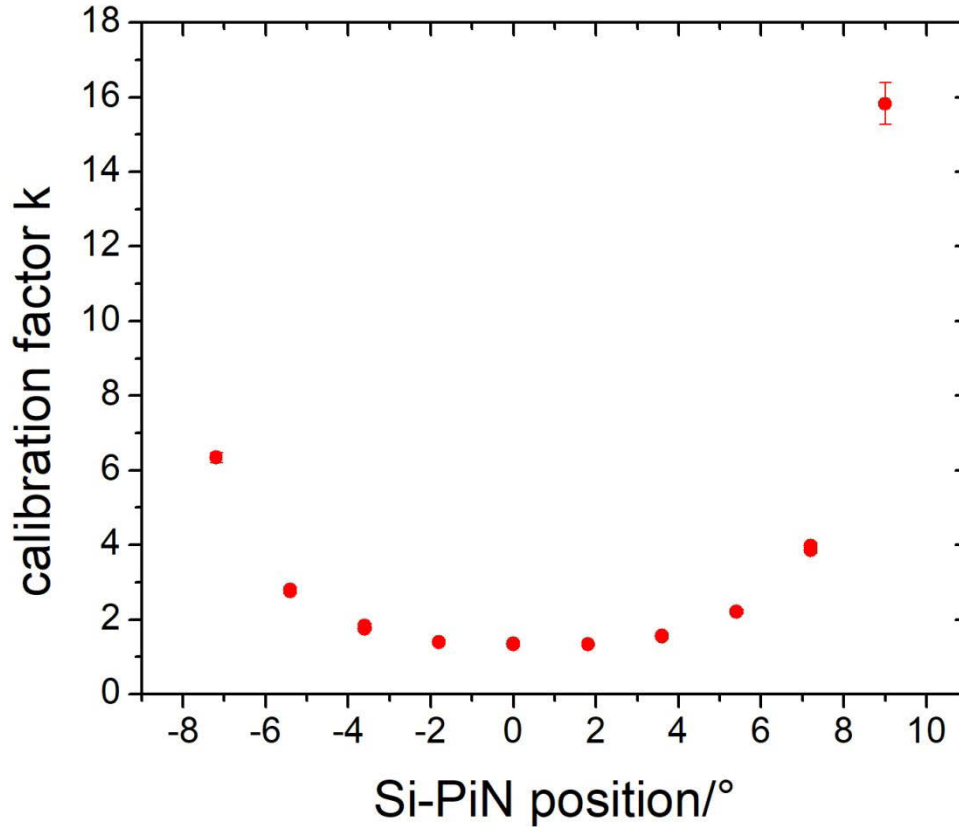


Figure 4-1-3-1: Dependence of the calibration factor k on the Si-PiN detector position. Clearly there is an area big enough to position the diode in position that detects the whole beam.

To make sure that the STIM detector positioned behind the sample holder collects the same number of ions as would hit the sample, another Si-PIN diode was placed directly at the sample position and the calibration factor was measured again. The calibration factor was determined to be 1.34 ± 0.01 in both cases, proving that the entire beam hitting the sample is detected by the STIM detector.

The calibration factor uncertainty stems from the statistical uncertainty of the measurement and the effect of incomplete measurement cycles. A measurement cycle of 1.28 s consists of first measuring the incoming ions for 0.5 s with the monitoring diode and then letting the beam through for 0.78 s to the sample/calibration diode.

An incomplete measurement cycle may occur if the beam was not measured for the whole 0.5 s on the monitoring diode and 0.78 s on the sample in that cycle because the measurement was stopped before. As start of measurement and movement in and out of the beam of the monitoring diode are not synchronised this always happens to some extent. However, there can be at most one incomplete measurement cycle. Increasing the number of the measurement cycles in the calibration factor measurements decreases this variance.

To further validate the method using another technique, a thin Leucine transmission sample, was used with a particle detector positioned closely behind the sample. The yield achieved by counting the transmitted ions was compared to the yield determined with the previously used technique. The ratio between ions detected by the monitoring diode and the transmitted particle counting diode for this measurement was 1.26 ± 0.01 .

Figure 4 shows the evolution of this ratio during the measurement. Unfortunately, the spectrum cannot be separated into equal time intervals but only into parts with the same number of counts. For figure 4 the spectrum was separated into ten parts.

Assuming the current was stable, each part is 125 seconds long as the whole measurement was 1250 seconds long. As the measurement progresses the measured ratio oscillates around the value of 1.26 ± 0.01 in contrast to the calibration factor determined without a sample in front of the diode of 1.34 ± 0.01 .

The reason for this discrepancy can be attributed to the heavy ion straggling and multiple scattering effects in the sample, causing a part of the ions not to reach the diode.

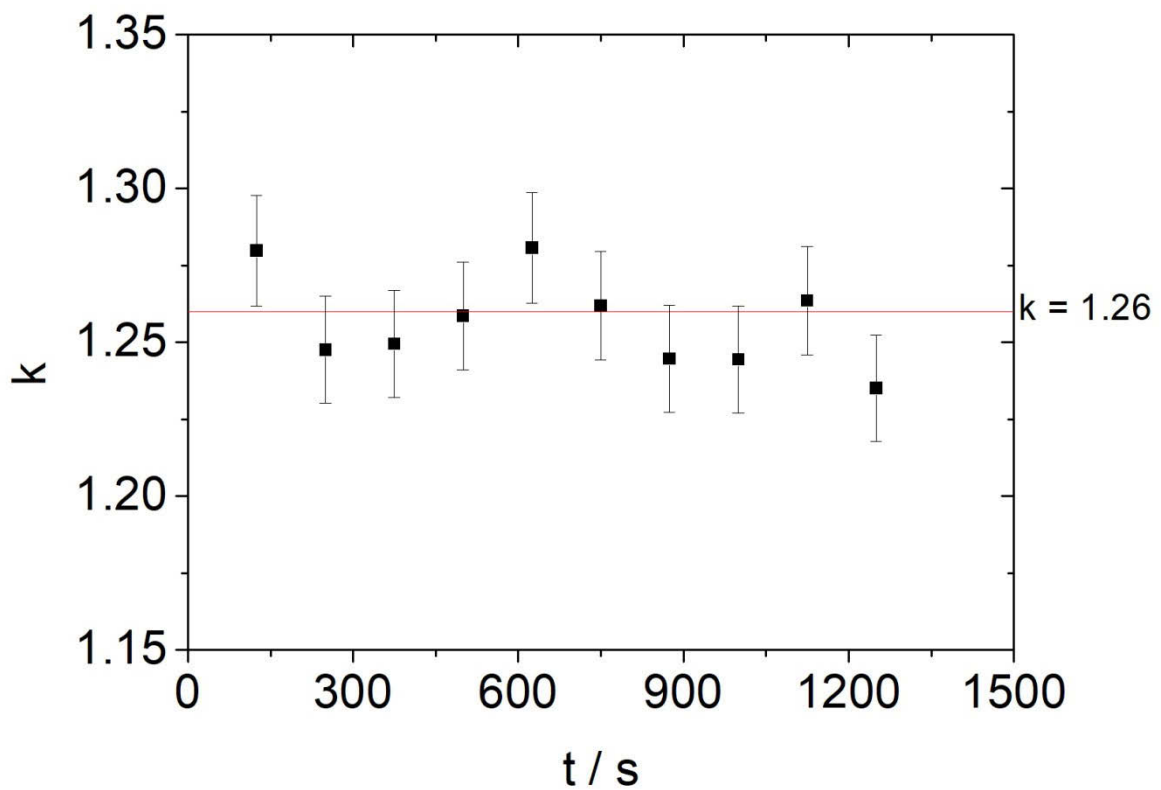


Figure 4-1-3-2: Evolution of the ratio between the intensity detected behind the sample to the intensity on the ion beam monitor. The ratio oscillates around the calibration factor of 1.26.

4.1.4 Systematic error of the primary ion measurement

Due to an inbuilt error of the DAQ the primary ion counter lost a number of primary ion counts depending on the amplification set in the amplifier before the ADC. Preliminary testing showed a loss of 14 % for an 8 MeV Si^{4+} beam, comparing the signal detected for the two independent DAQs used for the MeV SIMS measurements and the primary ion intensity. Further testing with a 50 Hz function generator as an input revealed that the loss of counts increased with the voltage of the input signal.

This systematic error is stable for a set amplification and all measurements done with the same amplification, as is the case usually for measurements in the same day, have the same error and can be compared.

The error is more significant for the secondary ion yield dependence on the primary ion energy and type measurements. These measurements happened on different days and can show a different systematic error.

Fortunately, the practice of choosing the amplification so the peak of the primary ion beam appears in a channel which is close to the middle of the spectrum, lead to a stable systematic error during most yield measurements. This shows itself well in the small variation of the oxygen primary ion yield measurements. For Silicon primary ions the variation is bigger which can be explained by the more important influence of the varying surface conditions of the samples on the yield for Silicon and is not necessarily caused by the systematic error introduced by the DAQ.

As the systematic error is not precisely known it will be approximated by 15 % lower yield and 5 % error on top the statistical error that will be investigated in the next chapter.

4.2 Thick wall capillary for ion beam collimation

Glass capillaries for ion beam collimation are an interesting new development for MeV SIMS, with the capability to make this technique widely available. Capillaries have already been used in various scientific instruments, i.e. to deposit small amounts of liquids [67], for chemical analysis using capillary electrophoresis (CE) [68] and for focussing of x-ray beams [69, 70]. Recently a new application, ion beam collimation with glass capillaries, has been implemented at various ion beam analysis (IBA) laboratories [71, 72, 73, 74, 75, 76, 77]. Some publications [78, 79] reported a much discussed and controversial gain in fluence after the capillary exit, which so far has not been confirmed by further measurements.

Compared to the usually used electromagnetic lenses a capillary offers a cost-effective alternative for micrometre diameter ion beam generation. They require little space, no energy, are easy to install and good for targeting. Additionally, ion beam rigidity does not limit the range of usable ion masses or energies. For ambient pressure applications a capillary can even be used to replace two components: the collimator and the air-vacuum interface.

Investigations into the capillary transmission characteristics show that slightly tapered capillaries with tilt angles of few mill radians improve the ion beam transmission [78] and that, if a conical profile is used, the beam focusing ratio can be enhanced by a factor of two compared to conventional tapered capillaries with a convex inner wall [77]. A possible explanation is Rutherford scattering at the inner glass wall of the capillary occurring at small angles. While even the most efficient profiles only achieve beam focusing ratios close to unity [79], the capillary optics are very attractive for low current techniques like STIM, single cell irradiation and MeV SIMS. PIXE is also possible, but due to the low beam currents the acquisition time for a spectrum can increase considerably.

The low current obstacle can be removed if there are electromagnetic lenses present in the beam line. They can increase the current density hitting the capillary entrance and in return the capillary can enhance the focussing ability of the lenses [71]. This way a beam line using older EMQs or high rigidity ions that would be limited to i.e. 40 μm beam resolution can achieve 1 μm beam diameter or less.

Regarding the ability of capillaries to act also as air-vacuum interface, previous experiments have proven that a long micrometre diameter capillary limits the gas intake sufficiently to keep a stable vacuum in the beam line [71].

4.2.1 Production and usage of the capillary

The new type of capillary used for ion beam collimation is produced by pulling of a borosilicate glass tube at high temperature in a heating furnace. The manufacturing process has been implemented at the National University of Córdoba (UNC), and is normally used to produce x-ray capillary optics [80]. The process of drawing has been carefully developed to produce capillaries with high quality conical inner profiles combined with thick walls. The resulting capillary is very robust even with outlet diameters in the micrometre range. A picture of one of the prototypes can be seen in Figure 4-2-1-1.

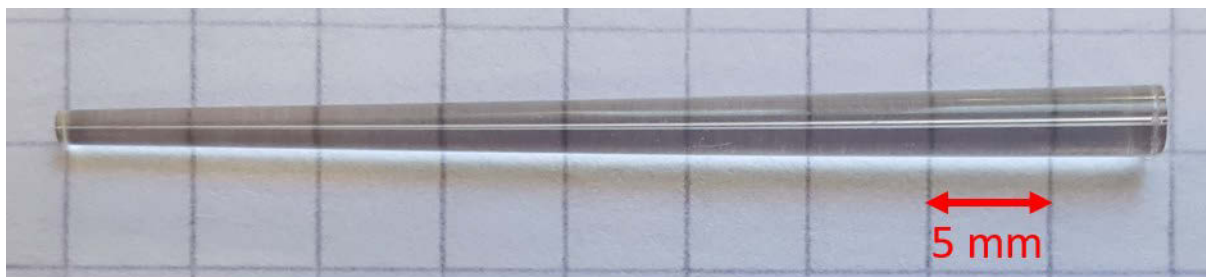


Figure 4-2-1-1: One of the capillaries produced in the UNC. Notable are the thick capillary walls and the different inner and outer profiles. For reference, the squares on the paper on the back are 5 mm x 5 mm.

Three different capillary types have been tested, one short and cylindrical (KV2) with an outer diameter of 1700 μm at the tip and two long, conical ones with outer diameters 750 μm (KV5) and 710 μm (KV6).

To check if the capillaries can be used as ion beam optics, they were brought to the Laboratory of Ion Beam Physics at the Eidgenössische Technische Hochschule Zürich (ETHZ). Here a setup for the use of capillaries in ambient Ion Beam Analysis applications has been developed recently [71]. It is installed at the end of one of the beam lines connected to the 6 MV EN tandem accelerator.

The capillary is fixed onto a vacuum flange mounted on a bellow that can be aligned to the beam position and direction by a 2-axis goniometer on an XY stage. The chamber in front of the ambient pressure setup has an inner diameter of 5 cm and is pumped by a turbo molecular pump. Because the capillary opening is fixed in space, imaging is performed by mounting the sample on an XY stage driven by two stick-slip piezo motors. The maximum scanning range of the piezo drives is 7 mm with a closed loop positioning resolution of 50 nm. Adjustments of the sample distance to the capillary tip are done manually employing a micrometre screw.

After fixing the capillaries in this adapter to connect them to the beam line, a test regarding the influence of the capillary opening on the pressure in the beam line was performed. A sufficient vacuum was obtained for all the three capillaries tested with the pressure remaining in the 10^{-6} mbar range.

For the following measurements each capillary was prepositioned using a Laser beam running through the beam line. Angles must be aligned carefully towards the beam direction in order to allow the beam to transmit through the small opening. Afterwards the unfocussed 2 MeV proton beam was sent through the capillary and detected by a Hamamatsu S3590-09 large area PiN diode (10 \times 10 mm detection area) placed behind the opening. While monitoring the intensity detected by the diode, the capillaries' position and inclination were further optimized.

After intensity optimization, energy spectra of the ion beam after passing through the capillary were taken with the PiN diode. The same detector was used for Scanning Transmission Ion Microscopy (STIM) measurements of a gold mesh (mesh dimensions: 50 μm thick bars with 200 μm space between each bar). Furthermore, spectra for in-air PIXE were taken using an Amptek X-123 SDD x-ray spectrometer with a detection angle of 45° to the sample surface.

4.2.2 Testing of capillary characteristics

Energy spectra of a 2 MeV proton ion beam after passing through the three tested capillaries (KV 2, KV 5 and KV 6) taken with the Hamamatsu diode are shown in figure 4-2-2-1. The spectra are normalized to the intensity of the high energy peak for comparison.

All tested capillaries show two characteristic features when compared to the ion beam before passing through the capillary: An increase of the energy peak width (FWHM) and a low energy tail. Both effects can be explained by scattering of the ion beam at the capillary tip and scattering due to the increased pressure in the capillary. The differences in peak broadening between the capillaries originate from the different ratio of scattered to directly transmitted ions depending on capillary position and shape. Additionally, a smaller exit diameter leads to fewer directly transmitted ions and a higher influence of scattered ions. The capillary with the widest energy peak and the most pronounced low energy tail is KV 6 which hints to a smaller exit diameter for this capillary but could also be explained by bad positioning.

The energy distributions of the capillary collimated beams show the potential of the capillaries for in-air Ion Beam Analysis as mostly non-scattered ions are transmitted which can be used for STIM or PIXE.

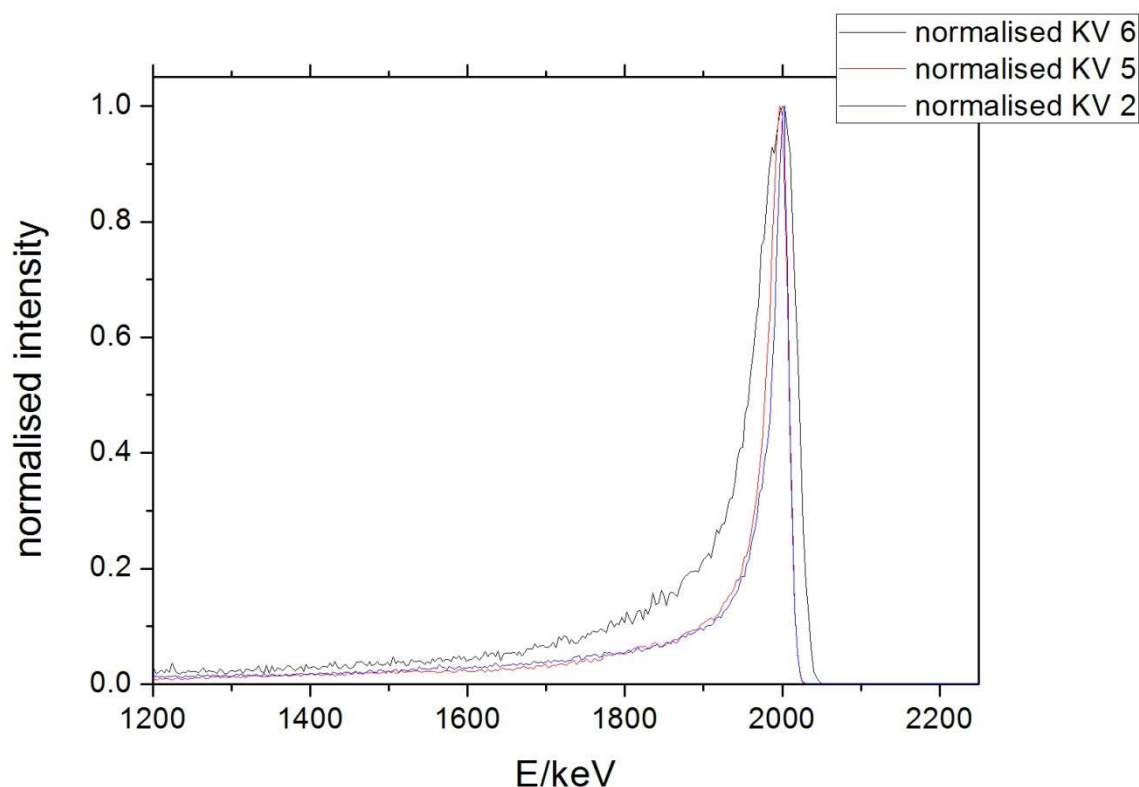


Figure 4-2-2-1: Normalized energy spectrum of a 2 MeV proton beam measured in air after passing through the thick-wall capillaries.

Imaging capabilities were also tested using a small gold mesh that was raster-scanned with the piezo positioners between the tip of capillary KV 5 and a Si-PIN diode detector. In figure 4-2-2-2 the resulting intensity profile is displayed. The diameter of the ion beam has been determined by convolution of a Gaussian beam profile with the mesh while varying the FWHM of the beam profile with the result of the fit being $(30 \pm 2) \mu\text{m}$. The error of the fit results from low statistics of the obtained data and beam fluctuations during the measurement. Further decrease of the ion beam diameter is possible with newly produced capillaries.

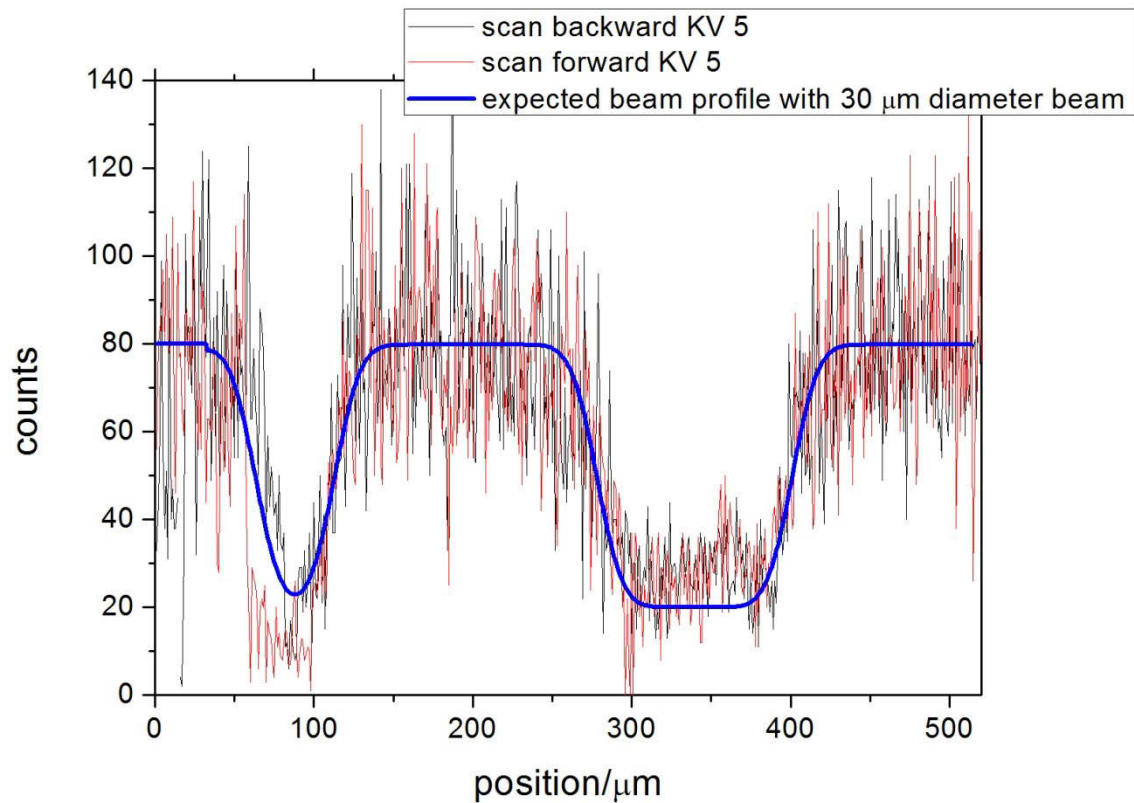


Figure 4-2-2-2: STIM raster scan of a gold mesh. In red the histogram of the scan in one direction and in black the histogram of the scan on the way back. In blue the expected scan profile for a beam with 30 μm FWHM.

Lastly, the capabilities of the thick wall capillaries for PIXE applications have been studied. Spectra obtained from an iron target using capillary KV 6 with and without steel shielding between the detector and the capillary tip are compared to a spectrum taken with a thin wall capillary from ETHZ (figure 4).

The low energy background present in the PIXE spectrum measured by the ETHZ capillary, which is most likely produced by excitations in glass near the capillary outlet, disappears completely for thick walled capillaries. The outer diameter of the capillary KV 6 tip is 710 μm which leads to a wall thickness of at least 300 μm around the ion transmitting channel, assuming that the channel's diameter is similar to KV 5's. This is well above the sum of the range of 2 MeV protons in glass (44 μm for 2 MeV protons in Borosilicate glass according to SRIM [25]) and the approximately 5 μm attenuation length [81] for Si K-line X-rays in SiO_2 . Thus, the wall thickness can explain the missing characteristic Si X-ray background, the major background source in PIXE measurements using thin wall ETHZ capillaries. A few new background events, not visible in the ETHZ capillary's spectrum, appear in the higher energy range. They can be attributed to characteristic X-ray emission from arsenic and rubidium. The addition of a steel shield between the detector and the capillary eliminates these peaks (figure 4-2-2-3).

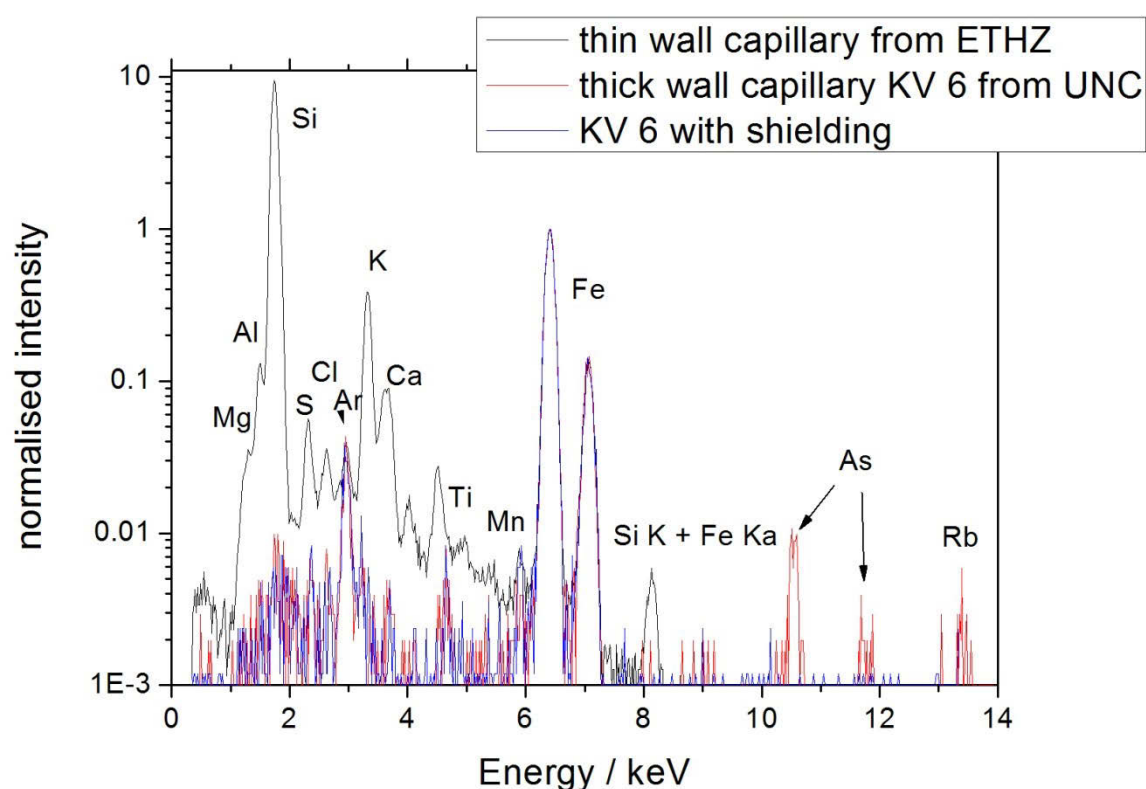


Figure 4-2-2-3: Comparison of PIXE spectra normalised to the Fe-K α peak from an iron sample using a common thin wall capillary from ETHZ (black), a UNC thick wall capillary (red) and a UNC thick wall capillary with shielding in front of the detector (blue). Spectrum acquisition durations were about 30 minutes for the KV 6 spectra and 2 minutes for the ETHZ capillary. Clearly visible: the suppression of the capillary wall material induced characteristic X-rays when using the thick-walled capillary and the deletion of the thick wall capillary background after introducing a shielding.

This proves that the arsenic peaks originate from impurities in the capillary material as exactly these peaks disappear after adding a steel shielding between detector and capillary. The attenuation length for the characteristic As K-lines is about 300 μ m for As K-lines at 10.5 keV according to [81]. A slightly thicker capillary, i.e. KV2, should suffice to suppress this background without shielding in front of the detector.

The overall low background is very useful for PIXE of light elements, making it possible to work without additional shielding.

4.3 Transmission triggered MeV SIMS

An alternative for triggering the TOF measurement for MeV SIMS through beam chopping is triggering through the signal produced by the impact of the primary ion in a detector. This can be achieved by using only samples that are sufficiently thin to transmit the ion beam and by detecting each transmitted ion after it has passed through the sample. While this approach limits the type of sample that can be used, it greatly increases the achievable spatial resolution. Additionally, information about the sample density is available as well, since the change in the primary ion's energy after passing through the sample that is related to the sample thickness at that particular position, can be measured.

4.3.1 RBI setup

A transmission-triggered setup has been designed and constructed at the RBI [20] by Dr. Zdravko Siketić (schematics in figure 4-3-1-1). The samples are deposited on a silicon nitride window of 50 nm thickness. Behind the sample the same Si-PIN diode as used for the ion beam intensity monitor, the Hamamatsu S1223-01, is positioned. It is mounted directly onto the sample holder behind the sample using a frame printed out with a 3D printer. Alternatively, the experimental chambers STIM detector can be used. However, as it is mounted further behind the sample, less of the ions traversing the sample are detected.

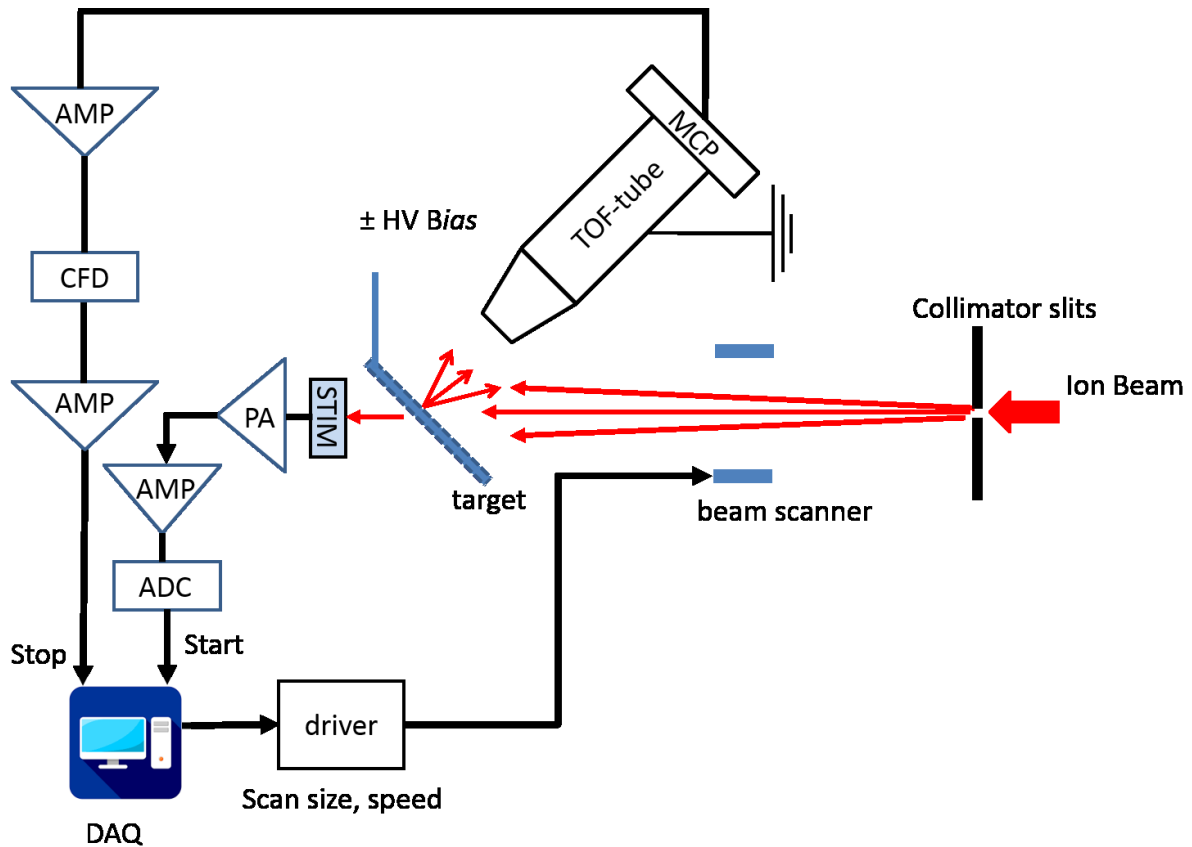


Figure 4-3-1-1.: Setup of the system for transmission-ion triggered MeV SIMS. The PiN diode behind the sample provides the energy of the primary ion after transmitting the sample and the start signal for the TOF measurement. The stop signal comes from the MCP detector at the end of the TOF tube.

The beam focussing for this experimental setup is done in two steps:

- First the high intensity beam is focussed on a fluorescent scintillator target while the object slits opening is 100 μm and the aperture slit opening is 1 mm.
- When the beam has been focussed the object and aperture slits are closed almost completely. Afterwards the STIM diode is used to measure the ion beam current, while the object slits are opened or closed, to change the ion beam current to the needed value.

Due to the low current typically used for MeV SIMS, both slits can stay in an almost closed position, which greatly decreases the ion beam spot size due to the significant decrease of the beam divergence in the system. Smaller beam divergence significantly reduces influence of focussing system aberrations (e.g. spherical aberration) when compared to the high current operational mode.

An example of a scan over a grid area can be seen in figure 4-3-1-2 for the high excitation triplet focussed transmission-triggered and figure 4-3-1-3 for a doublet focussed chopped beam triggered MeV SIMS. Figure 4-3-1-4 compares the beam profiles for both modes, illustrating further the difference in microbeam spatial resolution.

One has to take into account though that the scan in figure 4-3-1-3 is not the optimum focussing achievable for a chopped beam setup. It presents the routinely achievable beam spot used for measurement where good resolution is not necessary and beam intensity is kept high. Still the resolution achieved with transmission triggered SIMS cannot be rivalled by standard chopped beam SIMS.

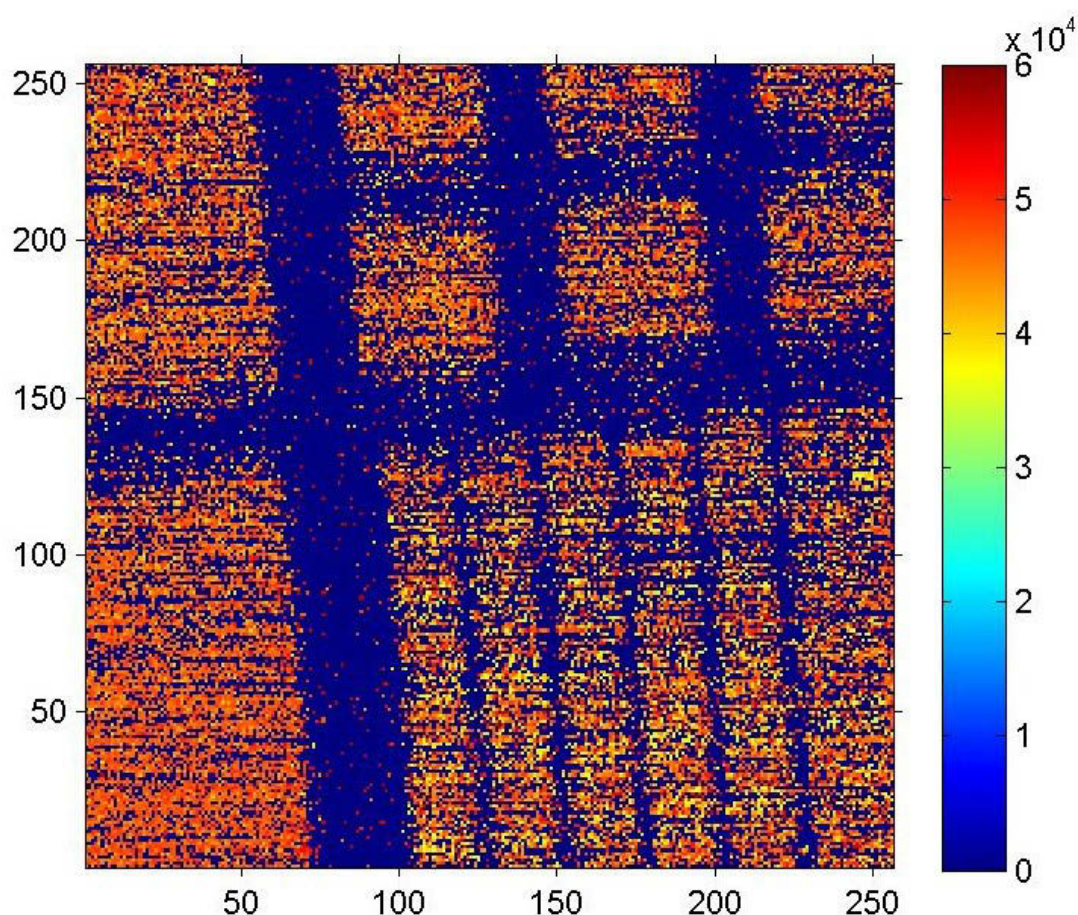


Figure 4-3-1-2: Resolution test for the transmission triggered SIMS using a 9 MeV O^{4+} on a Ni-plated grid [20]. The lateral thickness of the smallest grid bars is 400 nm and the scan size of the map $27\ \mu\text{m} \times 27\ \mu\text{m}$. The resolution achieved was 300 nm in the x and 500 nm in the y direction due to the 45° angle of the sample relative to the primary ion beam.

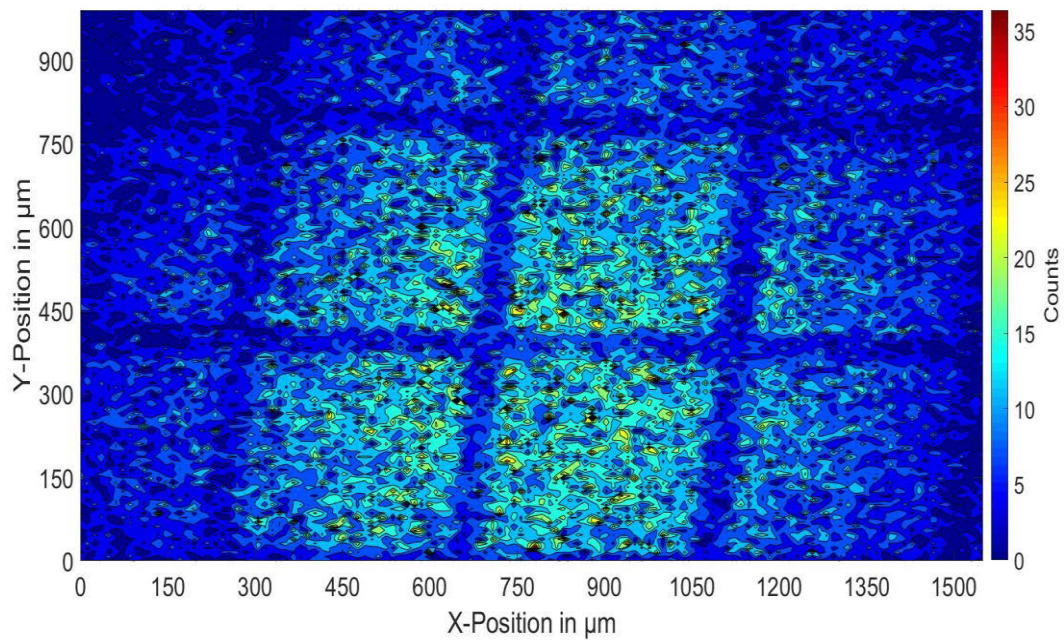


Figure 4-3-1-3: Scan of a copper phthalocyanine grid with scan size 1 mm x 1.5 mm using a chopped 8 MeV Si^{4+} beam. The microbeam resolution for this scan is 20 μm . Also visible is a dependence of the counts detected on the position on the sample, even though the material distribution should be homogenous. This effect will be investigated in chapter 5. The angle-dependence of the extraction leads to a strong variation in yields even though the sample is homogeneous.

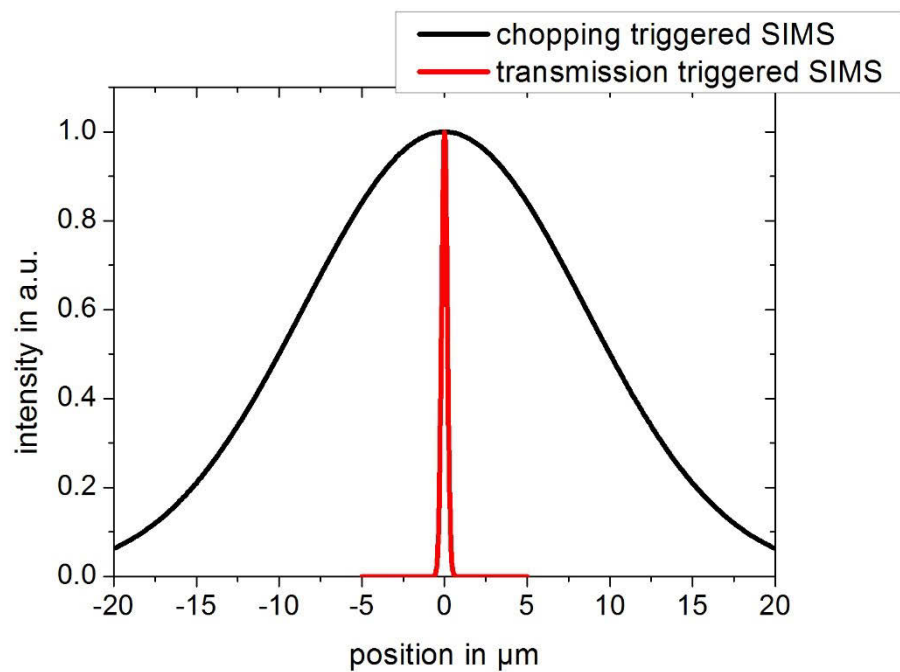


Figure 4-3-1-4: Comparison of the beam profile obtained from knife edge scan fits of the mappings of Figure 4-3-1-2 and Figure 4-3-1-3 illustrating the difference of resolution between the two modes.

5. Secondary ion yield dependence on experimental parameters

In this chapter the dependence of the secondary ion yield on different experimental parameters will be discussed. Each of the parameters such as the angle between the sample surface and the extractor, the distance between extractor and sample surface, the scan area, the extraction voltage and the beam position on the sample, influence the measured yield and are studied in detail here. In addition to these purely instrumental parameters, primary ion dependent parameters such as the yield dependence on the primary ion fluence and ion type have been studied as well.

5.1 Secondary ion yield dependence on setup parameters

The first experiments done with the RBI MeV SIMS setup showed that the measurement cannot be considered reliable and reproducible when simply positioning the sample in the ion beam and applying an acceleration voltage between sample and TOF tube extractor nozzle. It has been observed many times that the angle between extractor and sample must be varied, to detect a statistically significant number of secondary ions. Additionally, in many cases the sample needs to be moved, letting the beam hit different spots.

This motivated a more detailed and methodical study of the secondary ion yield dependence on parameters of the experimental setup. While many studies have been performed studying the effect of heavier and higher energy primary ions on the secondary ion yield [1, 3, 40] the optimisation of the setup has not been as thoroughly studied even though it provides ways to significantly improve the secondary ion yield.

The following chapter will therefore be devoted to the study of the variance of the secondary ion yield measurement itself and the dependence of the secondary ion yield on:

- the position of the ion beam on the sample
- the angle between sample and extractor
- the distance of the sample to the extractor,
- the scan size of the measurement
- the acceleration potential between sample and secondary ion extractor

The samples used have been either produced at the RBI or were sourced from cooperating laboratories.

For the samples produced at the RBI powders of the molecules investigated were used and some of them can only be dissolved in low concentrations. That is why evaporation through heating under low pressure on silicon wafers was chosen for sample mounting. The wafer size was between 10mm x 10mm and 20mm x 20mm and the evaporator at the RBI is an Univex 300 by Oerlikon-Leybold and with a pressure during the evaporation process of 10^{-3} mbar.

The samples not produced at the RBI were kindly provided by Vanina Cristuado from the KU Leuven, the Sprite Work package 4 colleagues Lidija Matjacic and Julien Demarche from the Ion Beam Centre, University of Surrey, and the group of J. Matsuo from the University of Kyoto.

5.1.0 Variance of the yield measurement

The MeV SIMS system as described in chapter 2 has various sources of variance regarding the mass (TOF) value of a signal. For the yield measurements, the whole mass peak for a given mass was chosen negating the influence of this error.

Now regarding the error of secondary ion yields, H.W. Werner summarises the error for keV-SIMS [82] and lists several error sources for a SIMS measurement. For the MeV SIMS measurements in this thesis most of the factors caused by sample inhomogeneity and beam current fluctuations are not present because pure samples and primary ion current measurement were used.

Instead the error of the diode primary ion counting as it has already been determined in chapter 4 must be considered. This error, together with the error of the secondary ion detection in the TOF tube and the variation in secondary ion production in the sample produces the error of a yield measurement, which can be observed in the experiment.

The value of this error for spectra obtained from a Glycine/Leucine mix target using an 8 MeV Si^{4+} primary ion beam scanned over an area of $160\text{ }\mu\text{m} \times 160\text{ }\mu\text{m}$, has been determined by repeated measurements at the same position and can be seen in Table 5-1-0-1.

Measurement Nr.	Glycine Yield in %	Leucine Yield in %	Total yield in %
1	2.1	2.30	19.0
2	2.0	2.21	18.4
3	1.9	2.13	17.9
4	2.0	2.30	19.0
5	2.1	2.30	19.0
Average yield	2.0	2.24	18.7
Standard deviation	0.1	0.08	0.5
Standard deviation in % of the yield	5	3	3

Table 5-1-0-1: Yield variation for measurements at the same spot. The total number of counts was about 400.000 for all measurements with 7000 counts in the Glycine peaks and 10.000 counts in the Leucine peaks.

The standard deviation observed decreased with the number of counts but is not proportional to the square root of the counts, which were about 400k for the primary ions and between 7k and 10k for the molecular ions. For this number of counts the part of the statistical error alone should be no higher than 1.5 % which indicates that counting statistics are not the only source of error.

5.1.1 Dependence on the position on the sample

When comparing secondary ion yields for different samples the variation of the yield that depends on the beam position on the sample becomes an important factor. In the following measurement a Leucine layer evaporated on the surface of a 10 x 10 mm silicon wafer was irradiated by a 11 MeV O^{4+} primary ion beam with a scan size of 1.5 mm for each spectrum taken. Between measurements the sample was moved manually in 1 mm steps through the ion beam in directions as indicated in Figure 5-1-1-1. The paths of both line-scans meet in the centre of the sample.

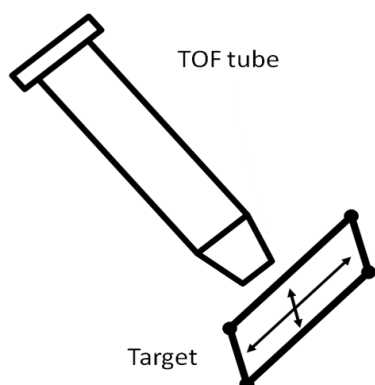


Figure 5-1-1-1: Schematics of the position dependence measurement. The sample holder was moved, and the yield was measured. The scan size for each measurement was 1.5 mm x 1.5mm.

The secondary ion yields of the 132 Da protonated Leucine peak recorded during this experiment are shown in Figure 5-1-1-2. Red circles show the results for the scan along the x-direction and black squares the scan along the y-direction.

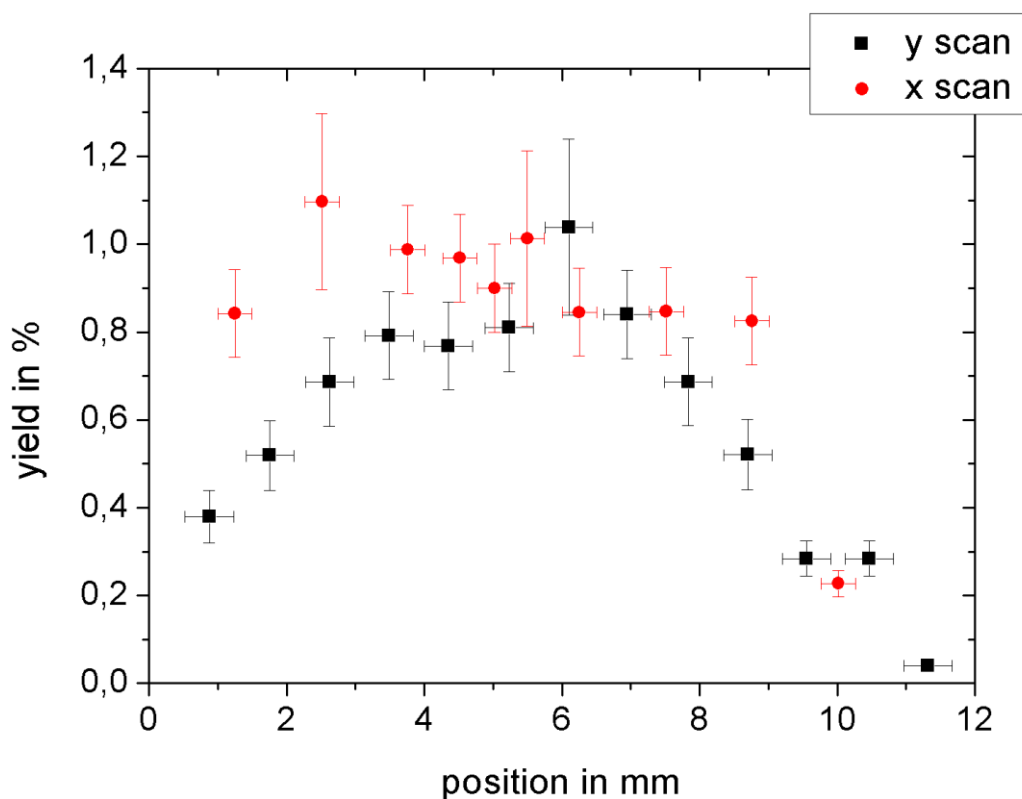


Figure 5-1-1-2: Scan over the sample surface on a Leucine sample using 11 MeV O^{4+} Ions and a scan size of 1.5 mm for each point. The signal is stable around the centre of the sample.

As can be seen in figure 5-1-1-2 the highest yield is achieved around the centre of the sample. The yield decreases towards the edges, before reaching zero at the sample edge. While one has to be aware of the effect of the scan size and a decrease of the secondary ion yield is expected at the sample edge, the yield-decrease for the y scan recorded is much less abrupt than what one would expect for a 1.5 mm scan size. An explanation for this behaviour can be found in distortions of the electric field at the sample edges:

Here the electric field diverges from the homogenous field which is present at the sample centre and the secondary ions will be accelerated on a bend path to the extractor nozzle. Accordingly, the secondary ions enter the nozzle at a small angle and might hit the nozzle wall instead of reaching the multichannel plate at the end of the TOF tube.

The additional use of ion optical elements in the TOF tube can help mitigate this edge effect, however it will have to be optimized for each sample geometry and it might be more practical to take only measurements from the centre of the sample if possible.

Returning to the question of the variation for a secondary ion yield measurement used in comparison with other measurements the relative standard deviation for the yields obtained from the stable centre region of the sample is 10 % for both scans and in the following measurements this error will be used when comparing yield measurements from different samples.

5.1.2 Angle dependence

The most sensitive and most easily recognized experimental parameter influencing the secondary ion yield in the MeV SIMS measurements at the RBI is the angle between the sample and the ion extractor. To study it, the angle on the horizontal axis perpendicular to the ion beam has been varied as is shown in Figure 5-1-2-1.

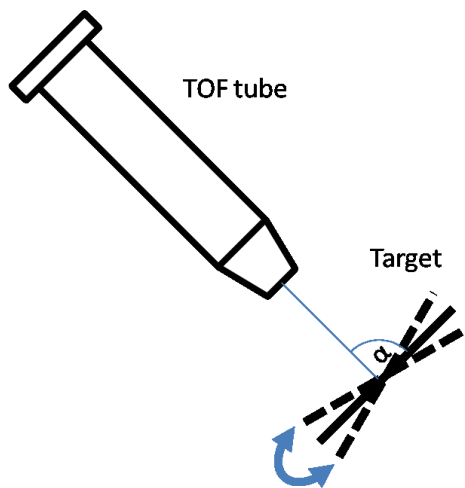


Figure: 5-1-2-1: A visualisation of the experimental parameter changed. Only one angle between the target and the TOF-tube can be changed. The other angle depends on the mounting of the sample.

An example of the yield variance from an experiment can be seen in Figure 5-1-2-2 showing two spectra from a Glycine/Leucine mixture using 8 MeV Si^{4+} primary ions. The absolute secondary ion yield per primary ion hitting the sample obtained in optimum geometry is compared with the yield obtained for an angle that differs by just 3.5° . Even though all other experimental parameters remain the same, the maximum yield is about four times higher for the optimum angle.

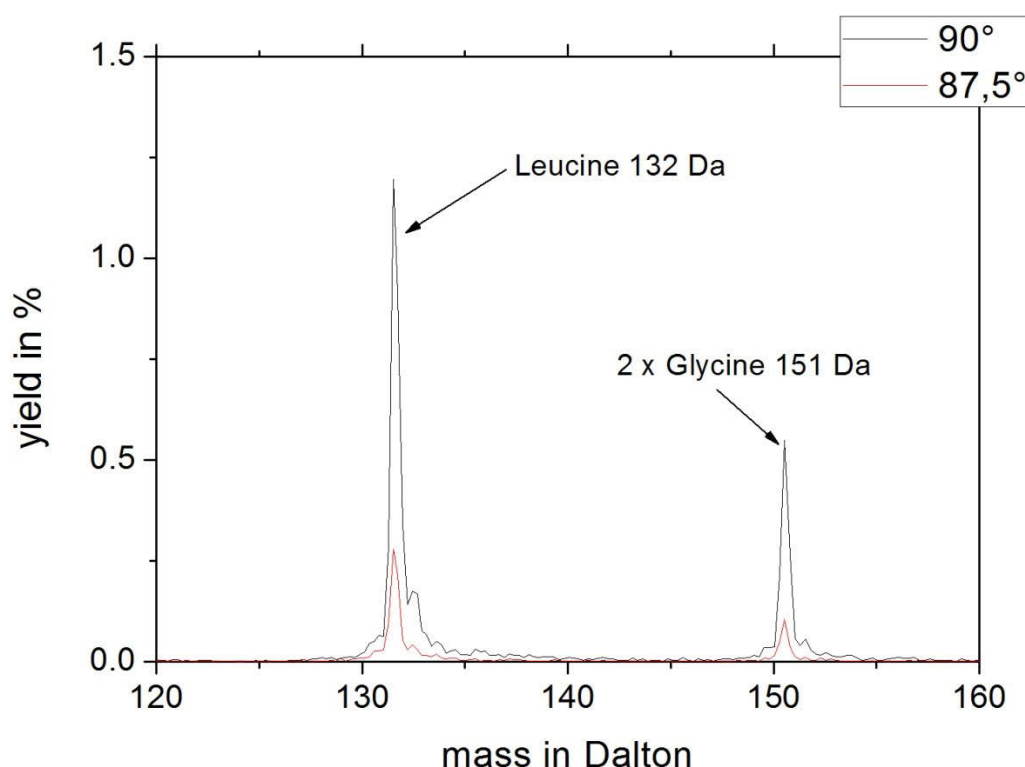


Figure 5-1-2-2: Comparison of the yield obtained from a mixed Glycine/Leucine sample for two different angles between the extractor and the sample surface. A slight deviation of 3.5° causes a yield drop of 80 %.

Hakansson et al. [3, 83] reported an increase in the secondary ion yield with the angle of incidence for glycylglycine, ergosterol and caesium-iodide samples. The angle between the sample and the secondary ion extractor is not reported in the publication, however from the sketch included, one can assume that the angle between the beam and the extractor was constant at 45°, which is similar to the RBI setup.

In our data the acceptance function of the extractor appears to dominate. The yield does not increase with an increasing angle of incidence. Instead the yield-angle dependence can be fitted to a Gaussian function, centred at an orientation of the samples surface perpendicular to the TOF tube extractor nozzle and at a 45° angle between surface and ion beam. For a Leucine sample, using 9 MeV O^{4+} primary ions, the FWHM of the secondary ion yield curve is 4.2°. A slight deviation of about 3° reduces the collection efficiency by more than 80 % (Figure 5-1-2-3). The effect applies to the whole mass spectrum and shows how important it is to have a variable angle between extractor and sample in the setup, to be able to achieve the highest possible yield.

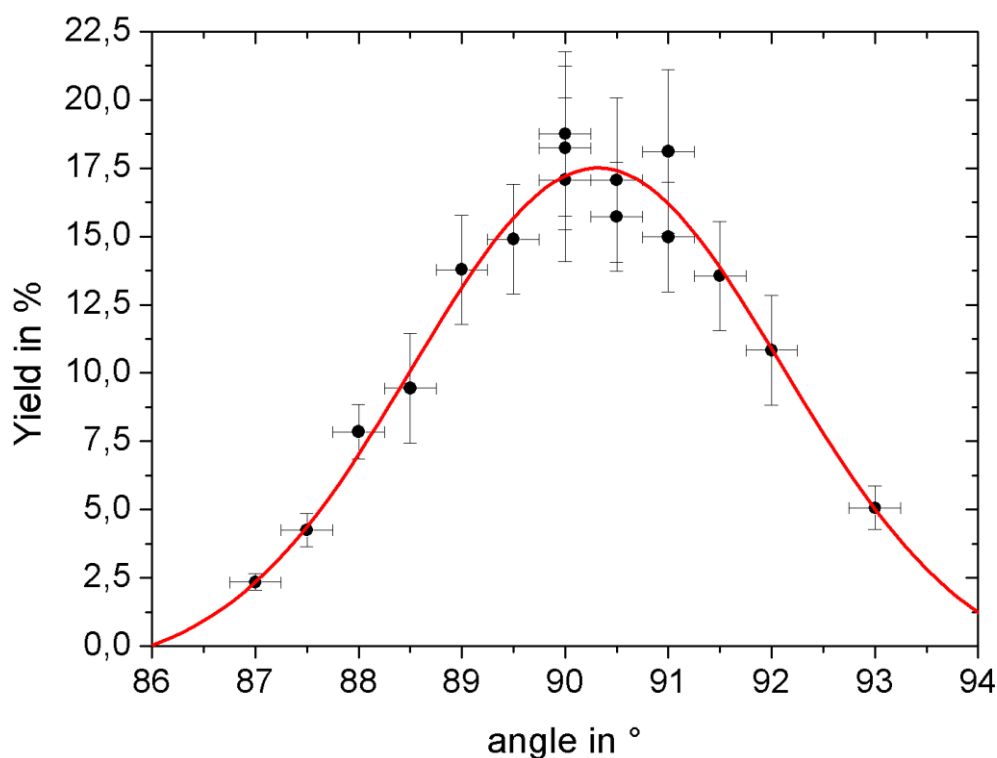


Figure 5-1-2-3: Total secondary ion yield from Leucine evaporated on a silicon wafer using 8 MeV Si^{4+} primary ions. It can be approximated by a Gaussian with the FWHM of 4.2° and the height of the 21 % yield.

While taking mass spectra of Irganox 1010, which has a much wider mass range with the main molecular peak at the high mass of 1179 Da, it became apparent that the optimal angle to achieve a high yield for this peak, does not coincide with the angle for the maximum of the total secondary ion yield for the sample. This prompted a closer look into the mass dependence of the yield-angle function.

Papaléo et al. [84] have shown that the secondary ions have a velocity distribution depending on the secondary ion type and mass. An oscillating mass dependence of the radial velocity has been observed.

Similar MeV SIMS experiments performed at the RBI show different angular yield dependencies for each secondary ion mass. Heavier particles are collected more efficiently in angle away from the incident ion beam (Figure 5-1-2-4). Additionally, the angular collection profile for secondary ions is narrower (lower FWHM) for higher masses (figure 5-1-2-5). Accordingly, the widest distribution is measured for hydrogen secondary ions.

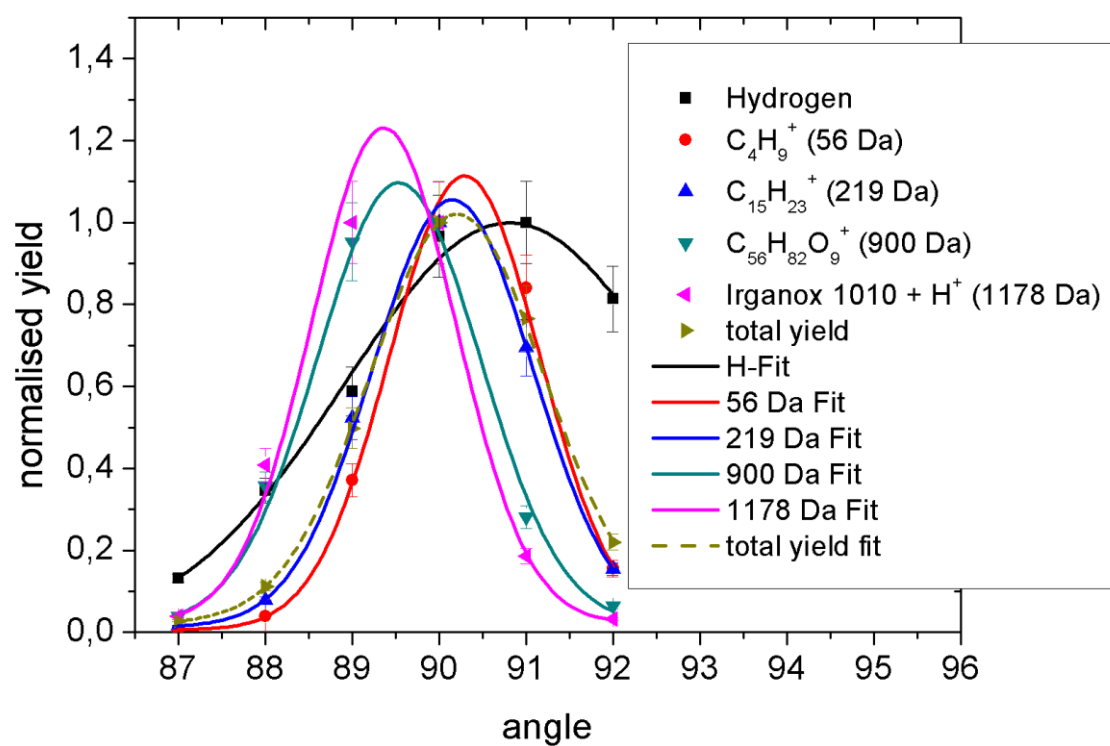


Figure 5-1-2-3: An example for the different yield-angle dependencies for the molecular peak of Irganox 1010 and various fragment masses, in the dashed line the total yield. Heavier mass secondary ions tend to be collected from an angle further away from the incident beam while the opposite is true for light mass ions like hydrogen.

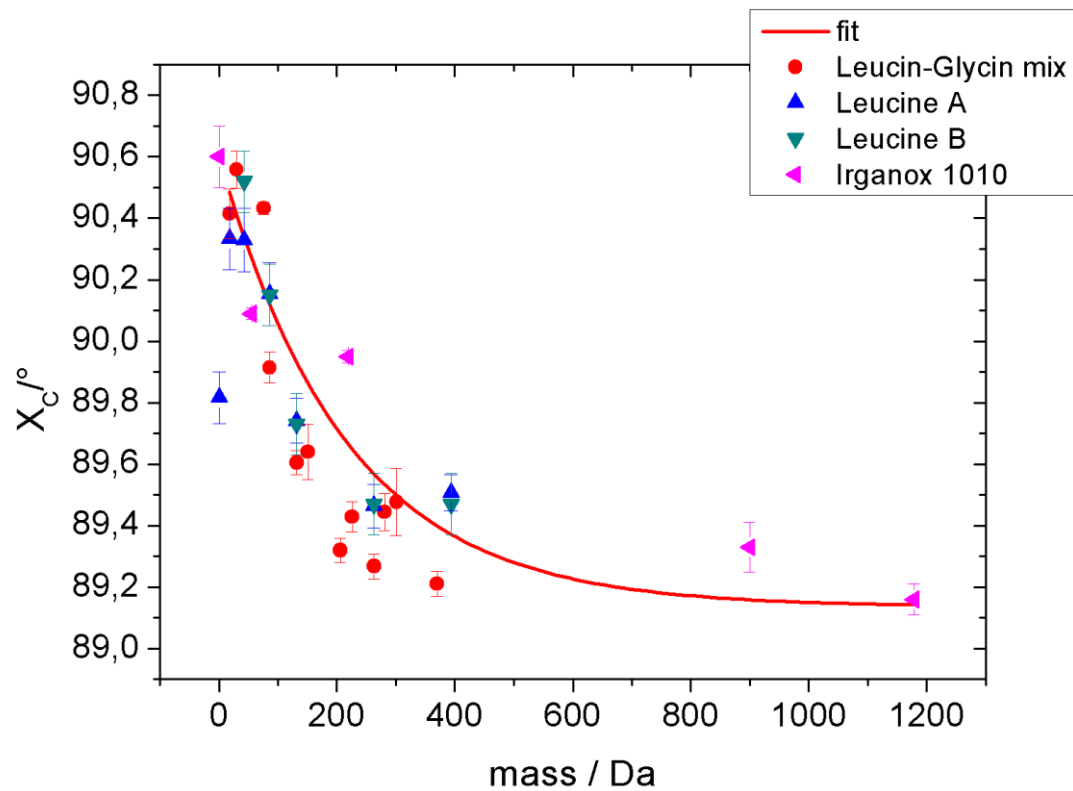


Figure 5-1-2-4: Mass dependence of the angle of maximum secondary ion collection. Two Leucine-, one Leucine-Glycine mix- and one Irganox 1010-sample were investigated. The angle of maximum secondary ion collection moves away from the primary ions beam direction with increasing mass. In red an exponential decay fit to guide the eye.

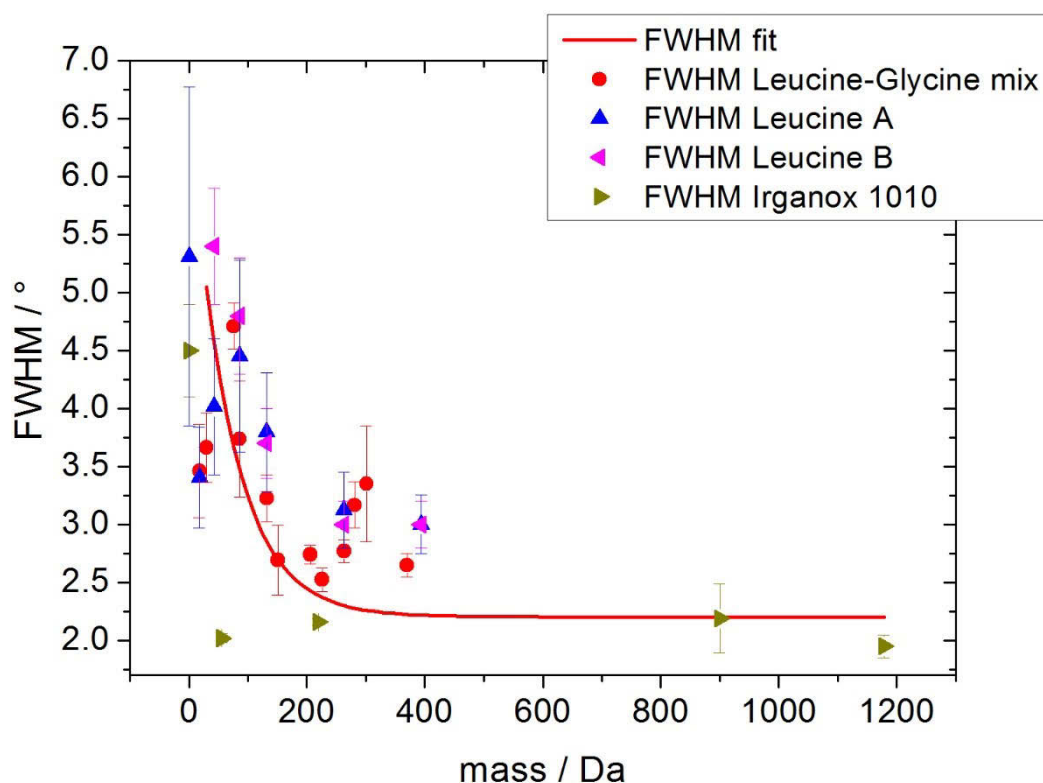


Figure 5-1-2-5: Mass dependence of the FWHM of the secondary ion collection angle dependence. Two Leucine-, one Leucine-Glycine mix- and one Irganox 1010-sample were investigated. The FWHM decreases with increasing secondary ion mass. An exponential function has been added to guide the eye.

Due to the nature of the Gauss fitting process the FWHM is not as reliable for Irganox and the Leucine-Glycine mix because a smaller number of data-points (angles) was available for the Gaussian function fit. The approximate centre of the secondary ion detection distribution is less affected by that lower number of data-points.

As mentioned earlier heavier secondary ions tend to be ejected in an angle further away from the primary ion beam. A similar bias for emission angles has been predicted by Molecular dynamics simulations [85] and was observed in experiments [86]. As is mentioned in these publications a directional bias of desorption is an indicator for a non-thermal effect and favours a pressure pulse like model of ion sputtering. The results presented here add to these previous results as they show the mass dependence of the angle dependent collection efficiency in more detail.

5.1.3 Dependence on the scan area size and the distance between extractor and sample surface

The angle dependence of the yield is a feature that has been observed in all measurements involving a large scan area. As an example, figure 4-3-1-3 shows a map of a phthalocyanine grid. The scan area is 1.5 mm x 1 mm with the distance extractor nozzle – sample surface of 1 cm, this results in an angular spread of $\pm 4^\circ$ for the whole scan, which is large enough to show a yield decrease at the edges of the scan area.

Considering the results from chapter 5.1.1, one must correct for the angle dependence of the secondary ion yield for any scan-size that leads to an angular spread of more than $\pm 0.5^\circ$.

This correction can be obtained by measuring a homogeneous sample of the material of interest. From this mapping a calibration function for the material in an inhomogeneous sample can be taken.

An example on how such a calibration function could look is shown in figure 5-1-3-1. Taking a cross section of the scan through the centre in y and x direction, the dependence can be approximated by a two-dimensional Gaussian function.

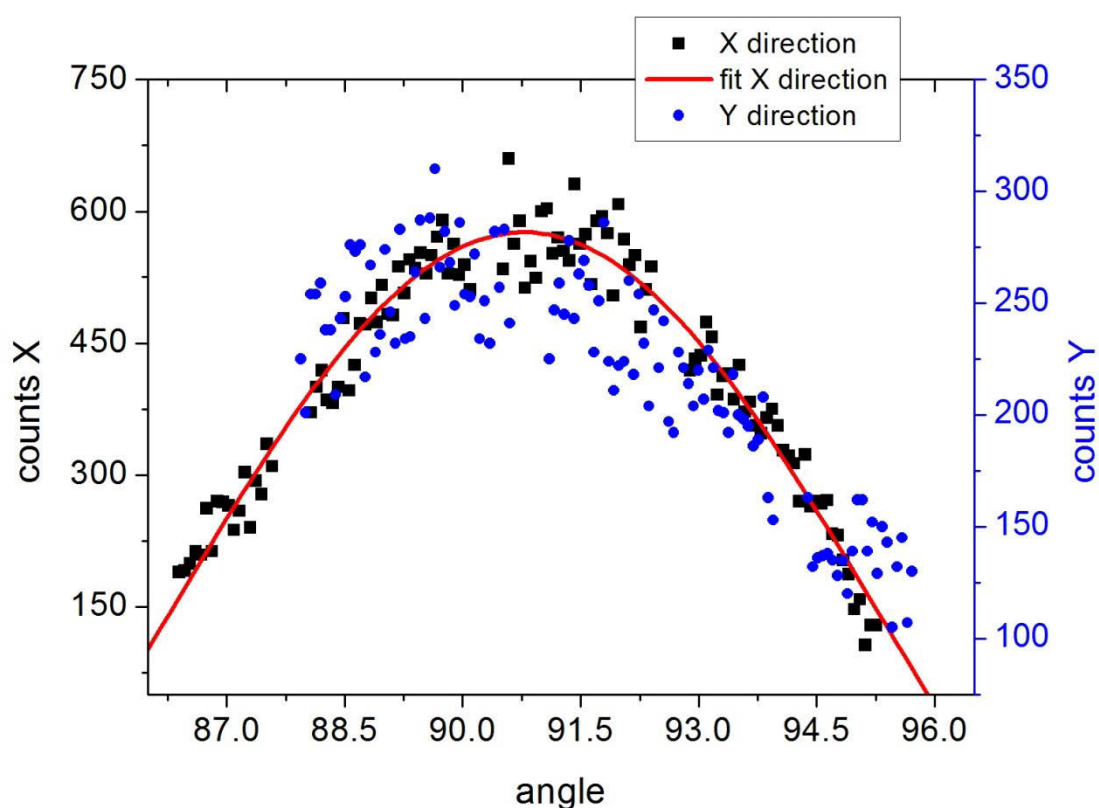


Figure 5-1-3-1: Angle dependence of the total yield as calculated from the scan from figure 5-1-3-1.

As the angular secondary ion yield dependence is a function of the secondary ion mass, a calibration function must be obtained for the different secondary ion masses present in a sample. For samples with mass spectra that have most of their mass in a narrow interval a total yield calibration function might be sufficient. In most cases though, several calibration functions will be necessary, one for each mass interval of interest.

Otherwise a non-calibrated mapping will show a variation of the ratio between peaks that can be misinterpreted as a change of concentration. Returning to Figure 5-1-2-3 one sees the maximum of the total yield is about 2° of the maximum for the Irganox 1010 molecular peak. A scan of 2 mm x 2mm would result in an angle variation of 6 degrees in both directions. The ratio between the different peaks in the Irganox spectrum will vary accordingly.

In some cases, certain molecular peaks will even disappear, leading to false negatives in qualitative investigations with the lower limit of detection (LLD) depending heavily on the sample surface roughness.

Figures 4-3-1-3 and 5-1-3-1 show that the angle dependence also exists in the y direction. To achieve the optimum yield in all circumstances a sample holder that can change the angle perpendicular to the x- and y-axis can be useful. A feature particularly useful if the sample has a very rough or inclined surface.

This inhomogeneous collection efficiency for mappings prompted an investigation into the relationship between the yield and the scan size as well as the influence of the distance between the sample surface and the TOF tube extractor nozzle (schematics in figure 5-1-3-2). The angular dependence of the secondary ion yield should manifest itself in yield variations for these parameters as well.

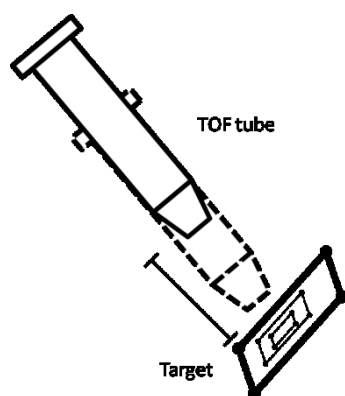


Figure 5-1-3-2: Schematics of the tested parameters. The TOF tube was moved back and forth and the scan size on the sample was varied.

The influence of the distance between extractor nozzle and sample surface on the secondary ion yield is shown in figure 5-1-3-3 for a Leucine and an Irganox 1010 sample. The results show the change of yield with distance is different for each sample.

For the Leucine sample (molecular ion mass 132 Da) the yield maximum was 2 cm from the sample surface. For the Irganox 1010 sample (molecular ion mass 1178 Da) the maximum yield was observed even further away at about 7 cm from the sample. Quite surprisingly, the total yield from a sample can increase with the distance.

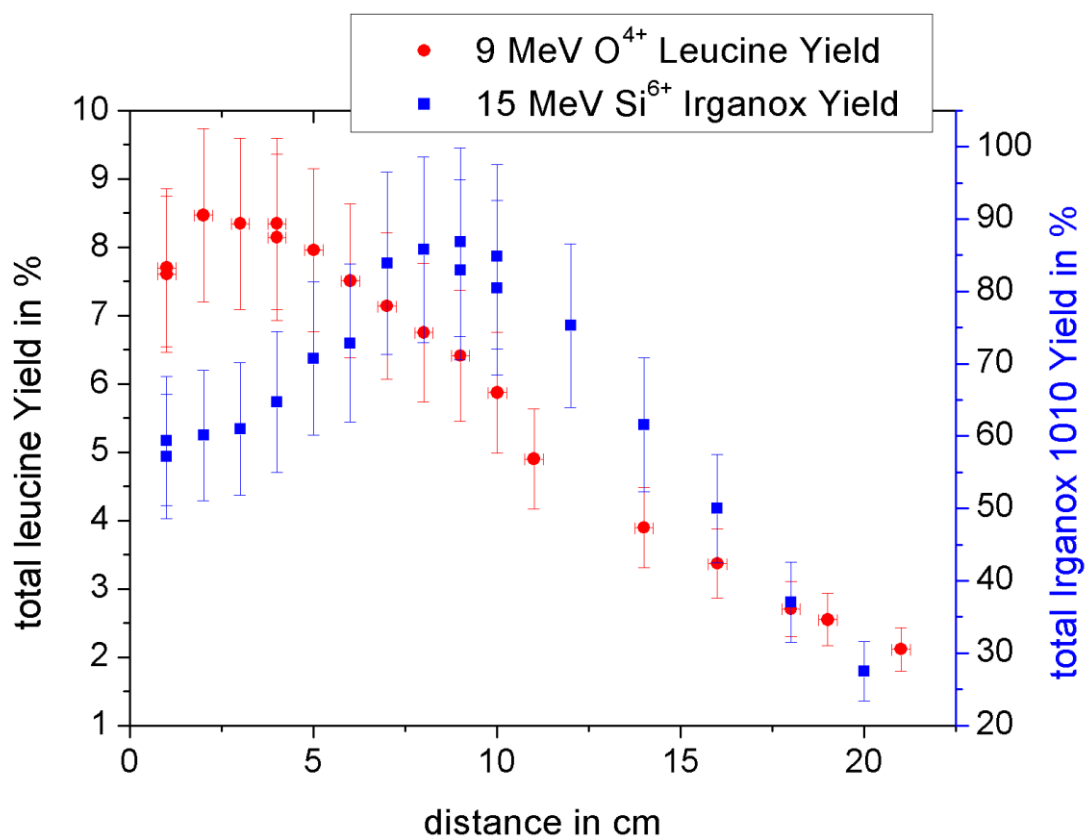


Figure 5-1-3-3: Yield from a scanned beam measurement on a Leucine sample using 9 MeV O⁴⁺ Ions (scan size 2mm x 2 mm) and Irganox 1010 (1 mm x 1mm) using 15 MeV Si⁶⁺. Especially for Irganox it is clearly visible that the scanning influences the optimum extractor sample distance.

To understand this effect better, the extractor distance dependence of the secondary ion yield was recorded for three different scan sizes (figure 5-1-3-4). As can be seen the yield increase for larger distances depends strongly on the scan size. For a point measurement the maximum in yield for a distance between extractor and the sample around 7 cm disappears completely. This indicates that the angular dependence of the yield is playing an important role.

A scan area of i.e. 2mm x 2mm with a distance extractor nozzle to sample of 1 cm causes a variation of the angle between sample and extractor of up to 5.7° during the scan. Revisiting figure 5-1-1-3 the secondary ion yield drops to zero if we are 6° of the maximum. By moving the extractor away from the sample up to 7 cm, the angular variation is reduced to less than 1° and the maximum yield can be achieved. This is supported by Figure 5-1-3-5 showing the yield from a point measurement decreases with the distance from the sample. The interplay of those two factors creates the yield distance dependence from a scanned area which is also visible in Figure 5-1-3-4.

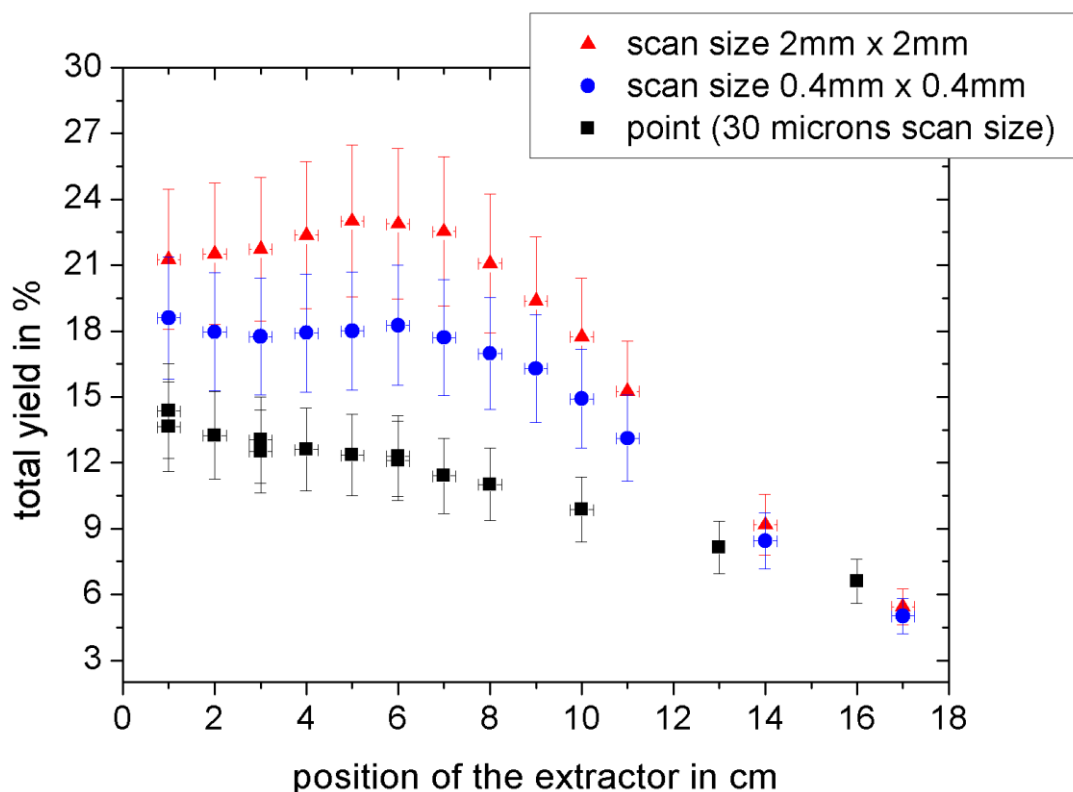


Figure 5-1-3-4: The total secondary ion yields for Irganox 1010 from 9 MeV O^{4+} primary ions. As one can see the bump becomes less pronounced for decreasing scan size and seems to disappear for a point measurement.

The differences in absolute total yield between the three scan areas hint to another important aspect of molecular imaging that can be easily overlooked. The differences can hardly depend on inhomogeneity in the sample as it is made up solely of Irganox 1010.

It is noticeable, that the yield increases with scan size. This can be explained by the angular dependence of the yield depending on the secondary ion mass. A larger scan size includes a wider angular range and will include more of the different optimum angles for the different secondary ion masses. Decreasing the scan size will decrease the available angle variation and thus the total secondary ion yield. This effect is more pronounced for mass spectra that show a wide range of secondary ion masses.

5.1.4 Dependence on the extraction voltage

For keV SIMS a strong dependence of the secondary ion yield on the extraction voltage has been reported by Gilmore et al. [62]. They have shown that while operating at 20 kV acceleration voltage, the MCP at the end of the mass spectrometer has an efficiency of 1 for masses up to 4000 Da. Meanwhile the RBI MS and most other current MeV SIMS setups (i.e. the JSI MeV SIMS [16]) operate with acceleration voltages that are much lower between 2 kV and 5 kV.

MeV SIMS is especially useful to produce high mass secondary ions where the influence of the acceleration voltage on the MS efficiency is especially pronounced. Accordingly, an investigation into the secondary ion yield behaviour for different acceleration voltages was undertaken for the RBI MeV SIMS.

The total secondary molecular ion yield obtained from Irganox 1010 for different extraction voltages can be seen in Figure 5-1-4-1. The increase of total yield is significant and already justifies realisation of a higher voltage setup.

Even more important for MeV SIMS is the yield increase for higher masses. Figure 5-1-4-2 compares the yield obtained for 3 kV extraction voltage to the yield obtained with 6 kV extraction voltage for different secondary ion masses. As can be seen, the yield increase is more pronounced for secondary ions having higher mass. Exactly the secondary ions one is especially interested in while performing an MeV SIMS experiment. The reason for this is the lower velocity of the heavy mass secondary ions with the same kinetic energy which decreases the secondary electron production efficiency in the MCP [87].

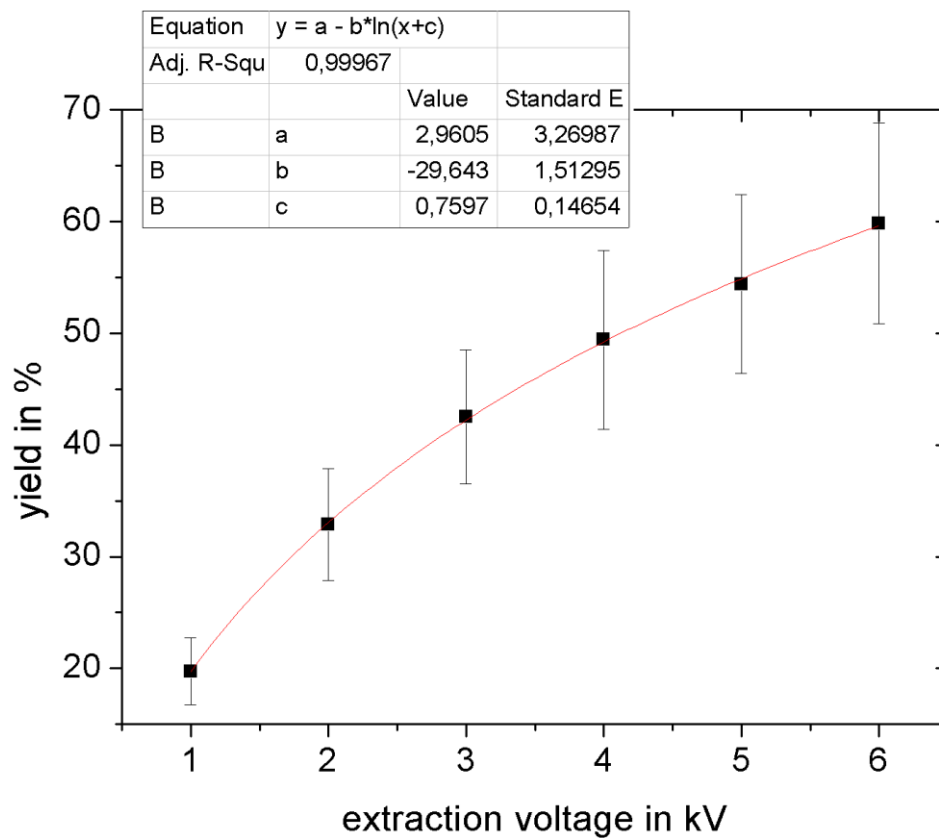


Figure 5-1-4-1: The total yield from an Irganox 1010 sample with 15 MeV Si^{4+} primary ions while varying the extraction voltage. Increasing the extraction Voltage from 1 kV to 6 kV leads to a more than threefold increase of the secondary ion yield. The fit indicates that the yield increase weakens for further voltage increase.

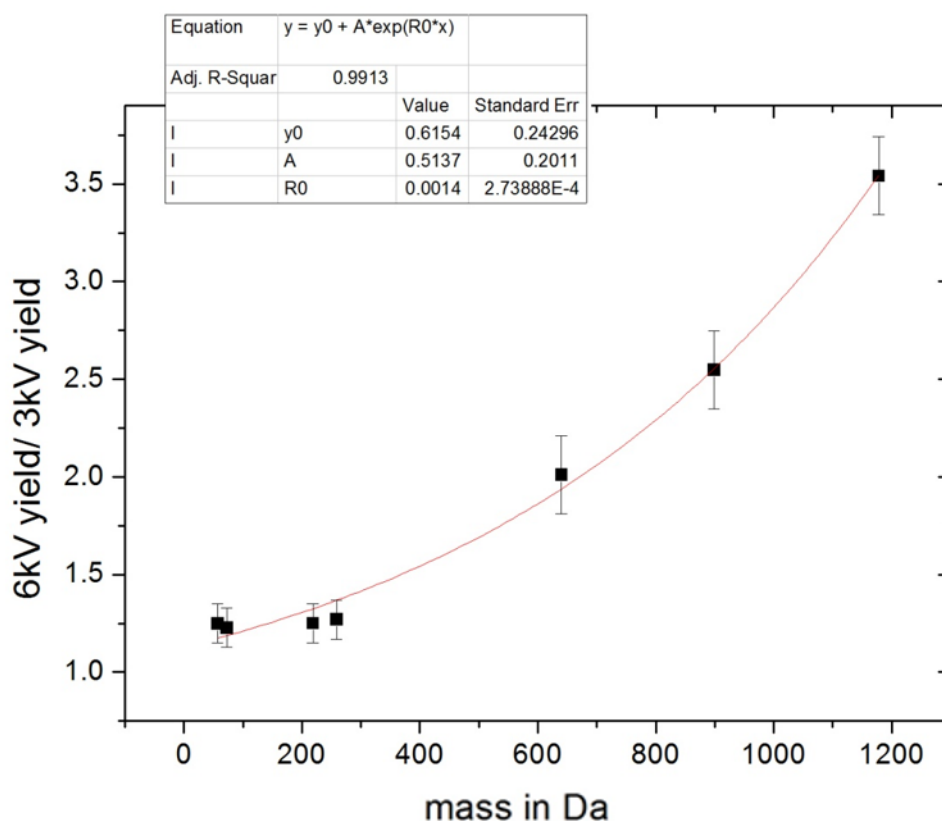


Figure 5-1-4-2: The quotient of the yield from an Irganox 1010 sample obtained with 3 kV extraction voltage and 6 kV compared for different mass regions. As one can see the effect becomes more significant for high masses.

Gilmore et al. [62] have tested this dependence for keV SIMS and the results presented in figure 5-1-4-2 from an MeV SIMS measurement follow the same trend with the results obtained in their publication for PS oligomers (Table 5-1-4-1).

Extraction voltage	keV SIMS on PS	MeV SIMS on Irganox 1010
6kV/3kV 800 Da	3.3±0.7	2.25±0.2
6kV/3kV 1200 Da	4.7±1.4	3.5±0.2

Table 5-1-4-1: comparison of the secondary ion yield obtained for extraction voltages of 6 kV and 3 kV.

The theory of electron production in the MCP predicts a velocity v_0 that changes the electron yield – velocity dependence from a higher order to a linear dependence. From Figure 5-1-4-2 it is visible that for masses below 300 Da the ratio for both voltages is constant hinting to a linear dependence of the yield on the ion velocity. The next datapoint above 600 Da has a very different ratio because it is already below v_0 for 3 kV extraction voltage. This means v_0 must be somewhere between the velocity of a particle with a kinetic energy of 3 keV and 300 Da mass and a particle with the same kinetic energy but 600 Da mass.

In Figure 5-1-4-3 the velocities for different molecule masses and the two extraction voltages as well as the range that includes v_0 for the atoms that form the Irganox molecule are presented.

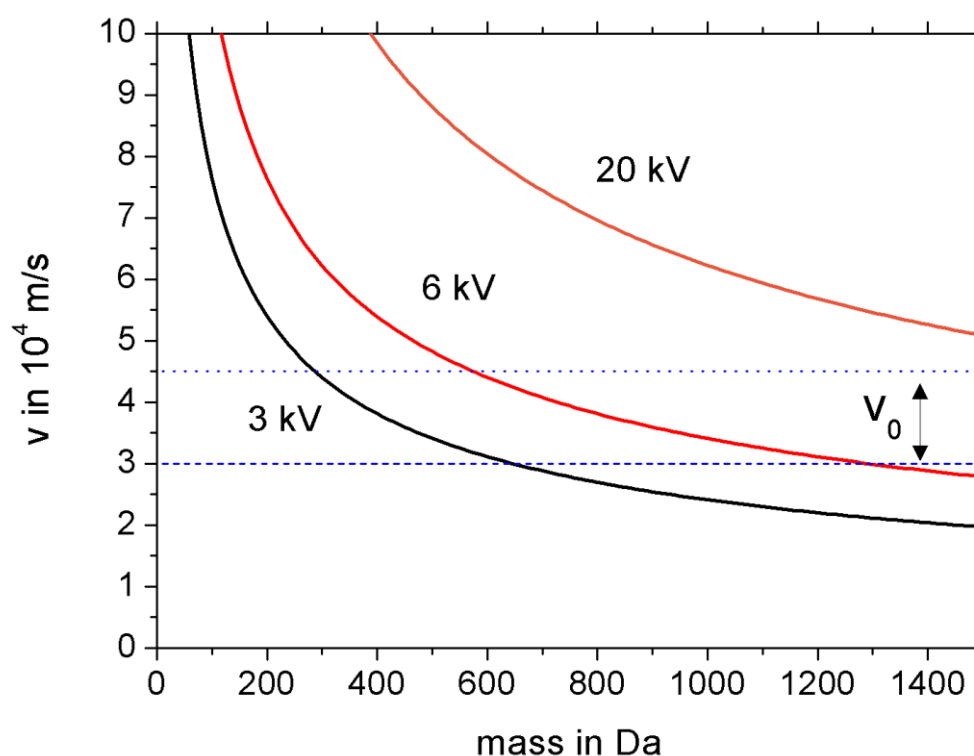


Figure 5-1-4-3: Velocity of the molecules as they hit the MCP. For the masses up to 1200 Da, 6 kV extraction voltage keeps the velocity of the molecule above the lower limit for v_0 obtained from Figure 5-1-4-2. 20 kV extraction Voltage provide velocities well above the upper limit for v_0 . The minimal extraction voltage necessary for staying above the upper limit of v_0 is 12.5 kV for 1200 Da.

The Results show that it is advisable to increase the extraction voltage to at least above 12.5 kV to obtain high yields for the Irganox molecular peak of 1178 Da mass. For higher molecule masses a higher extraction voltage is advisable. 20 kV would keep the velocity above the upper limit for v_0 for molecule masses up to 2000 Da.

5.1.5 Summary

The investigation of the experimental parameters' influence on the secondary yield has shown that all parameters need to be controlled carefully:

The yield depends on the angle between surface and the extractor and even a deviation of only 3 degrees can change the secondary ion yield by 80 %. The maximum of the secondary ion yield can be found close to a 90 °angle between the surface and the extractor and the angle dependence exists for the angles in both planes which can be seen in the mappings of homogenous samples. The angle dependence also changes with the mass. A secondary ion with heavier mass will be detected better in angle closer to the incoming beam while lighter mass secondary ions are detected about 2 degrees further away from the incoming beam. The acceptance distribution of the detector for the secondary ions decreases in width with increasing secondary ion mass. For accurate mappings the results have to be adjusted with the acceptance functions, if the scan size leads to a change of the angle between the extractor and the surface bigger than 0.5°.

The angle dependence also leads to varying secondary ions yields for different distances between extractor and surface. In some occasions it can be useful to increase the distance between sample and extractor to decrease the angle variation in a mapping.

Finally, it was shown that the extraction voltage is a significant factor influencing the detection of high mass secondary ions and an extraction voltage of 12 kV or higher is advisable to achieve high secondary ion yields for organic molecules with masses higher than 1000 Da.

5.2 Primary ion type and fluence dependence of the secondary ion yield

After the MeV SIMS setup is optimised, investigating the yield dependence on different primary ion beam characteristics such as the ion type, ion energy, its charge state and fluence can be used to further increase the secondary ion yield and provide insight into the secondary ion desorption process.

Previous publications have already shown that the MeV SIMS secondary ion yield depends on the type of primary ion used [1, 3]. With the newly developed ion beam intensity monitor [24] described in chapter 4.1. it is now possible to add data to the database of secondary ion yields for different primary ion types.

5.2.1 Primary ion characteristic dependence

Silicon and oxygen primary ions with kinetic energies between 5 and 18 MeV were used to study the secondary ion yield dependence on the primary ion type, energy and charge for thin layers of Leucine, Glycine and Irganox 1010 evaporated on Si. The fluence on the sample was between 10^{10} ions per cm^2 (for measurement in one point) and 10^8 ions per cm^2 (for the beam scanned over the sample).

In the Leucine sample the higher electronic stopping power for silicon ions compared to oxygen ions, leads to a higher secondary ion yield for the protonated Leucine molecule ($m = 132.1$) over the entire energy region (Figure 5-2-1-1). Similar results are obtained for Glycine and Irganox 1010 (25 % total secondary ion yield for oxygen, 105 % total secondary ion yield for silicon) with the yield of Silicon primary ions usually about four times higher than for oxygen primary ions. Also visible in the figure is the velocity effect's influence on the secondary ion yield [3] for the oxygen primary ions with the stopping force beyond the electronic stopping maximum.

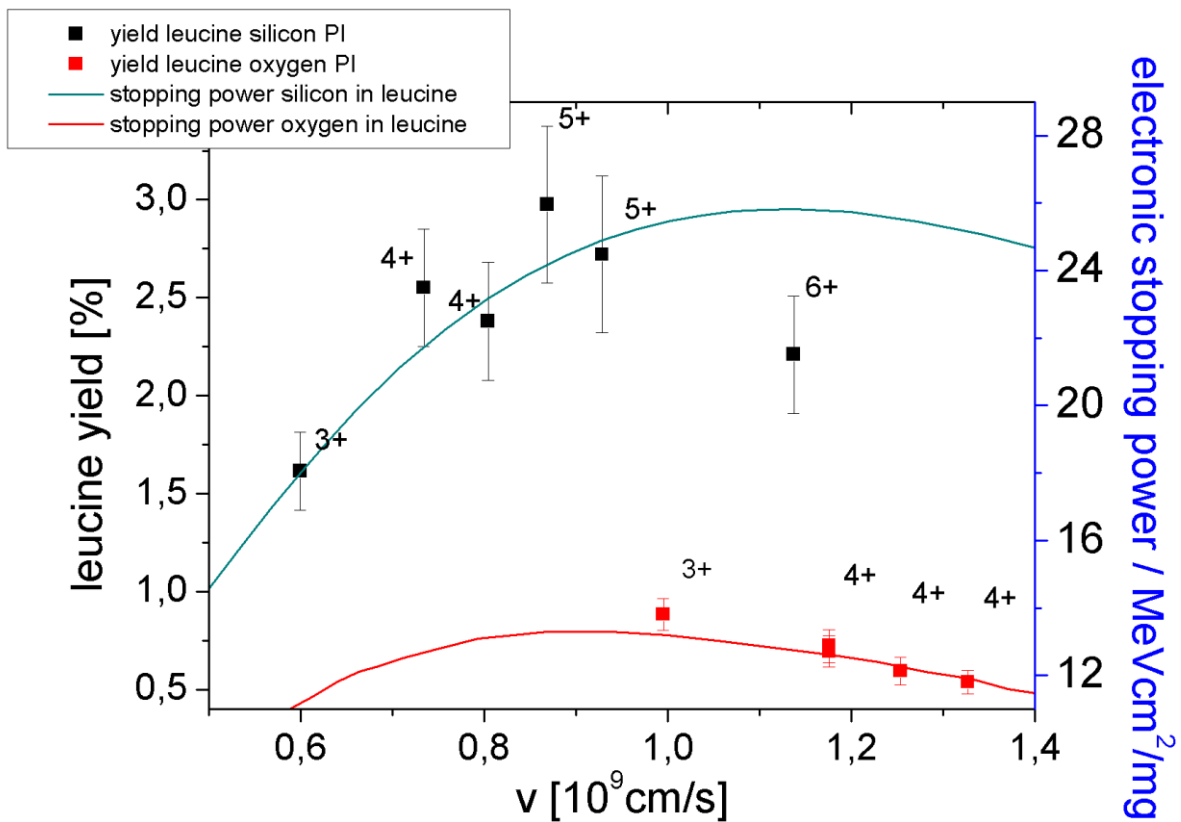


Figure 5-2-1-1: Yield versus ion velocity measured for a Leucine target using oxygen and silicon primary ions with different energies and charge states.

The variation of yields measured for a certain primary ion - target combination is high, especially for silicon primary ions, due to the strong dependence of the yield on the target's surface condition. Proper ways to decrease this variation must be found and reproducibility has to be improved before a more comprehensive study can be performed.

For now, the high variation of the secondary ion yield between different samples of the same type, especially for silicon primary ions, makes it advisable to perform these measurements on the same sample and during the same beam time (experimental conditions) in order to minimise the error.

One thing that can be taken from the data though, is the proportionality of the yield versus the electronic stopping power. For a shockwave model the yield Y is supposed to be proportional to the stopping force cubed and for the thermal spike the yield is proportional to the square of the stopping force.

The stopping force for Silicon with a primary ion velocity of 10^9 cm/s is around $24 \text{ MeVcm}^2/\text{mg}$ while it is about $12 \text{ MeVcm}^2/\text{mg}$ for oxygen. The yields obtained for the protonated Leucine peak in this velocity region are $(0.8 \pm 0.1) \%$ for oxygen and about four times higher with $(3.3 \pm 0.3) \%$ for silicon. This squared dependence on the stopping force supports the thermal spike model [39].

The total secondary ion yield obtained from Irganox 1010 shows a similar dependence with 25 % yield for Oxygen primary ions and a $13 \text{ MeVcm}^2/\text{mg}$ stopping force and 105 % yield for Silicon primary ions and a $25 \text{ MeVcm}^2/\text{mg}$ stopping force in the velocity region of 10^9 cm/s.

This comparison is quite rough because the results have not been recorded for the same primary ion velocity for Silicon and oxygen primary ions.

While the yields observed here are orders of magnitude higher than the yield observed for keV-SIMS, the question of the LLD and the maximum resolution achievable depends on the ionisation efficiency of MeV SIMS. If the damage produced by MeV ion impact is orders of magnitude higher as well, not much is gained regarding resolution and LLD. This question is the topic of the following chapter.

5.3 Fluence dependence of the secondary ion yield (dynamic MeV SIMS)

During MeV SIMS particles are sputtered/desorbed from the sample due to ion bombardment. This leads to the question after which primary ion fluence on the sample the MeV SIMS spectrum changes significantly due to modifications of the surface.

In the following chapters, terminology already established for keV-SIMS regarding the fluence dependence of the yield will be used, where one generally distinguishes between two modes of operation:

Low fluence static SIMS where it can be assumed that the primary ion beam always hits a pristine, not yet damaged part of the sample surface, and high fluence dynamic SIMS where the sputtering of the particles from the surface is used to perform depth profiling on a sample. For a long time, dynamic SIMS was the standard of SIMS until TOF-spectrometers made low fluence static SIMS possible [88].

The static keV SIMS limit usually is defined as the fluence that leads to a > 10 % of change in the secondary ion yield (static yield) and has been found to be between 10^{11} ions/cm² and 10^{13} ions/cm for different polymers with larger, more complex molecules having a lower static yield limit [89].

The static SIMS limit must be determined for MeV SIMS as well. If MeV SIMS is i.e. applied as an imaging technique for sensitive cell or tissue samples the varying static limits for different molecules can easily lead to false, relative concentrations. It is therefore advisable to determine the molecules that are of interest during the measurement and to stay below the static limit for these molecules. Additionally, the static SIMS limit also influences the practically achievable resolution for a measurement.

5.3.1 Crater formation

As MeV SIMS uses secondary ions ejected from the sample some form of material loss after ion bombardment can be assumed. A simple irradiation experiment was performed to see the form of crater produced. The sample to study this process was a 10 mm x 10 mm Leucine layer deposited on a silicon wafer which was irradiated with a continuous 8 MeV Si⁴⁺ ion beam for 30 minutes in an approximately 2 mm x 2 mm square area. The exact fluence itself was not recorded for this test run. From fluences recorded in previous experiments an order of magnitude of 10^{12} to 10^{13} ions/cm² can be assumed.

The results of a subsequent Atomic Force Microscopy (AFM) measurement performed on the irradiated area prove that this is well above the static SIMS limit for Leucine. First visual inspection of the sample clearly indicated changes of the surface. A picture, taken with the Atomic Force Microscope's optical microscope, can be seen on figure 5-3-1-1 showing the changes on the surface for the irradiated area which appears yellow compared to the green non-irradiated area. Also visible is some surface contamination from dust particles.

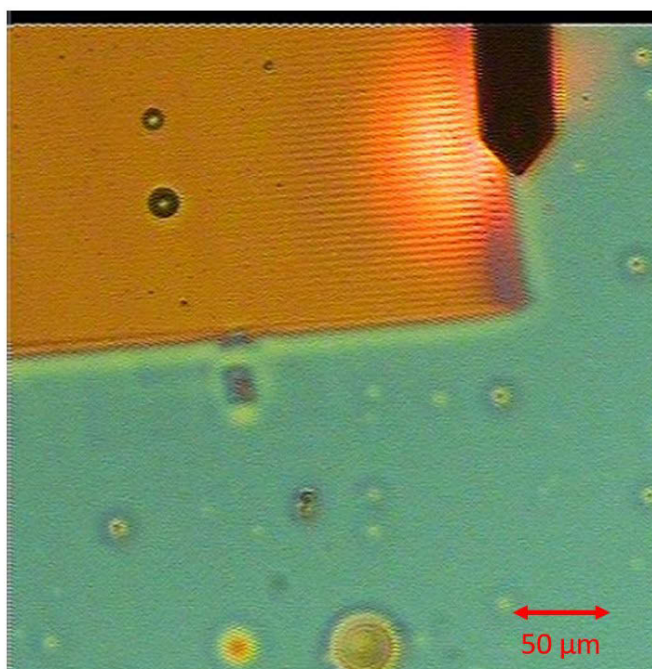


Figure 5-3-1-1: Optical microscope picture of the irradiated area and the AFM probe. Small trenches produced by the ion beam can be seen.

The profile of a scan over the edge (figure 5-3-1-2) indicates that the surface layer and layers below have been removed as the depth of the depression area produced is (30 ± 5) nm. The small trenches formed at the bottom of the depression have a depth of (5 ± 3) nm.

The upper layers are sputtered away which means MeV SIMS depth profiling is possible. The experiments also show that fluences that are within the static limit range of keV-SIMS are well above this limit for MeV SIMS, which while not certain from the outset regarding the different desorption processes, is an expectable result taking into account the higher stopping force for MeV ions.

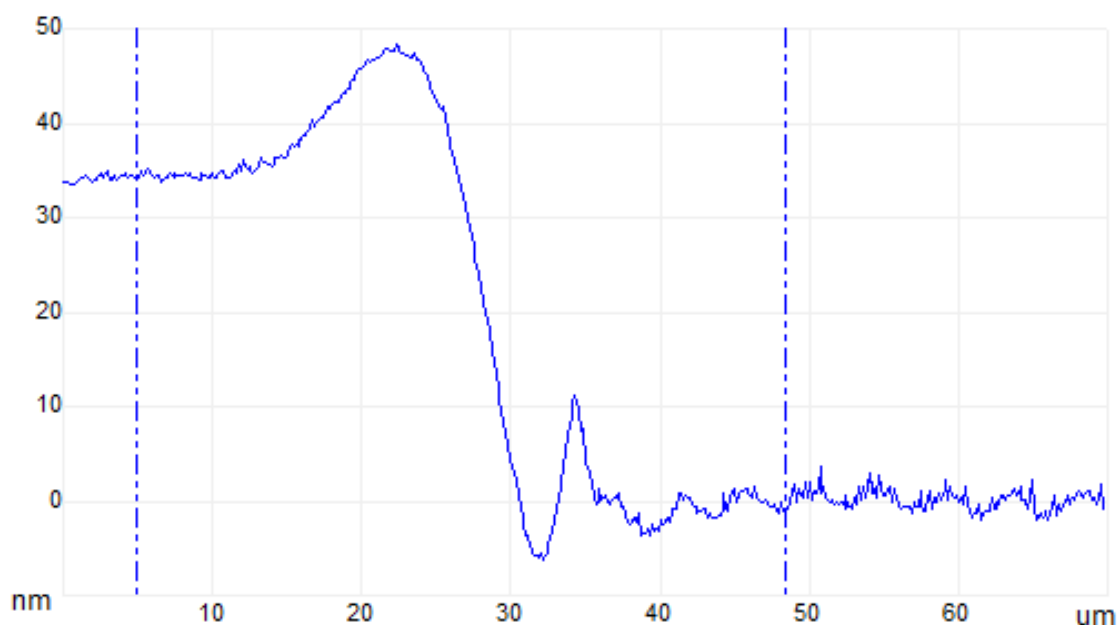


Figure 5-3-1-2: Sample morphology profile of an AFM scan over the border of the ion beam scan area showing the desorption of material from the sample as well as the deposition of material to the side of the ion impact area.

Another interesting result of the AFM measurement was that the ion microbeam left an array of trenches where it hit, which happens if the scan area and scanning speed are synchronised and the irradiation is unequally distributed in the scan area.

5.3.2 Static SIMS limit for organic compounds using MeV Ions

After verifying that MeV SIMS leads to crater formation, the limit of static SIMS, as the point when the yield for a given molecular ion changes from the starting value by more than 10 % [89], has to be investigated. As was mentioned before, for any quantitative MeV SIMS measurement knowledge of the limits of static SIMS is important, as the secondary ion yield combined with the static limit defines the lower limit of detection, as well as achievable spatial resolution of the technique for each analyte on a given sample.

The static limit for keV-SIMS is usually assumed to be around 10^{12} ions/cm². A look at the fluence dependence of the secondary ion yield for Irganox and Leucine (figure 5-3-2) shows a change in yield at fluences well below 10^{11} ions/cm². A similar effect was observed by Lau et al. [90] during keV SIMS of a low-density compound on Gold. This shows that for SIMS and especially MeV SIMS the static limit cannot simply be assumed and has to be tested carefully for each compound analysed.

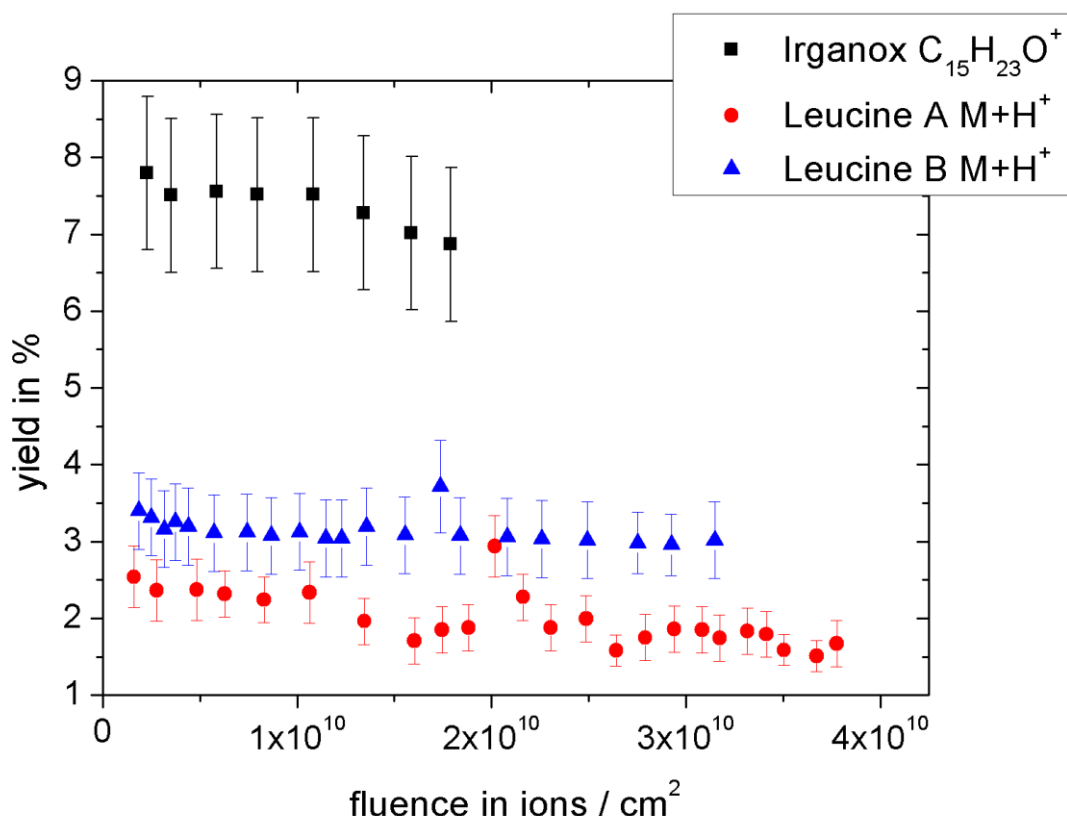


Figure 5-3-2-1: The yield evolution of two Leucine and one Irganox samples for low primary ion fluences, below an assumed static limit. All samples were irradiated with 8 MeV Si⁴⁺. Leucine A was measured by radiating in between measurements a larger area 400 µm x 400 µm and collecting the SIMS spectrum in the centre of the irradiated area from a 200 µm x 200 µm square. For Leucine B and Irganox 1010 the area irradiated was the same for all measurements 200 µm x 200 µm. In this case there can be an influence of the scan area border.

All samples show a decrease of secondary ion yield after the first data point indicating a sensibility of the yield to even the lowest fluences. Afterwards the yield is stable up to 10¹⁰ ions/cm² until a second decrease of yield starts. Both Leucine samples show a second local peak at about 2 x 10¹⁰ ions/cm². However, due to low statistics, and possible measurement error, this cannot be confirmed with confidence. As can be seen in the following chapter this behaviour is uncommon for the molecular peak whose yield generally decreases monotonously with increasing fluences.

5.3.3 High fluence (Dynamic) SIMS behaviour for homogenous samples

After the determination of the static limit for MeV SIMS an investigation of the yield behaviour at higher fluences becomes a necessity to find out what happens to the sample under further irradiation by MeV ions (i.e. cross linking [91], changes from positive resist to negative resist [92]) and if it is possible to develop a technique similar to keV SIMS depth-profiling for dynamic MeV SIMS.

An important value for dynamic MeV SIMS is the damage or disappearance cross section σ , defined as the area affected by a primary ion hitting the sample. Assuming an exponential decay of the yield during irradiation, the damage cross section can be calculated from a fit of the yield (Y) dependence on the fluence (f):

$$Y(f) = Y(0)e^{-(f/\sigma)} \quad (5.3.3.A).$$

The exponential decay assumes that each impact destroys a certain area of the sample surface, making it impossible to obtain a secondary ion for the molecular ion from this area.

A good example for the limits of this assumption are the results of measurements which were part of International Atomic Energy Agency (IAEA) coordinated research project (CRP) F11019, aiming to determine the MeV SIMS damage cross sections for various materials.

The yield – fluence dependence was recorded for two samples of Leucine on silicon. Both samples are single Leucine layers of (300 ± 100) nm thickness evaporated on silicon wafers. The results for a 5 MeV Si^{4+} primary ion beam for primary ion fluences up to 6×10^{12} ions/cm² and an irradiated area of 1 mm x 1 mm are presented in figure 5-3-3-1.

As one can see an important discrepancy in experimental yields for fluences up to 2×10^{12} ions/cm² is observed between the two similar samples. The yield for the 132 Da Leucine peak from sample A is initially more than twice the yield for the same peak from sample B. This difference could be caused by different surface conditions affecting the yield. As fluence increases above 2×10^{12} ions/cm², the yield from sample A drops down to the same yield values measured for sample B. At fluences above 2×10^{12} ions/cm² both yields stabilize.

Despite the difference in yields the static SIMS limit as defined before (10 % change in yield) is around 1×10^{12} ions/cm² for both samples.

The initial difference in secondary ion yield highlights the influence of surface contamination on the secondary ion yield. At the same time the experiment presents a possibility to have robust fully repeatable yields for a certain primary ion/sample combination and a similar approach was used by Imanishi et al. [2] on Silicon and Silicon-Oxide to prepare the sample surface before measurement:

Through irradiation before the measurement any surface contamination can be sputtered away and a layer that was previously below the surface is analysed, cancelling out the strong influence of sample handling and/or surface contamination on the secondary ion yield. As this layer has been already affected by transmission of MeV ions it has to be investigated how much these primary ions influence the yield and if it is indeed possible to get the same yield for samples with different surface conditions after the surface layers have been sputtered away.

Another possibility to clean the samples surface before the SIMS measurement, is the use of a keV ion gun to clean the sample surface by sputtering [93].

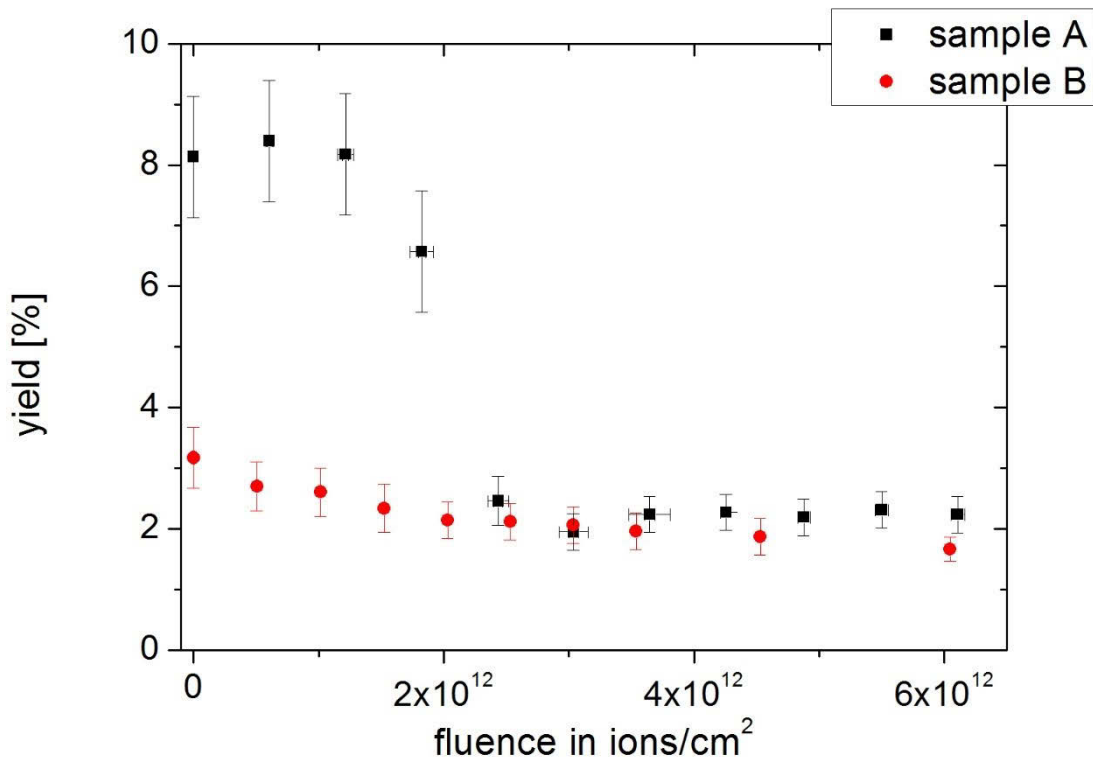


Figure 5-3-3-1: Fluence dependence of the yield obtained from two different Leucine samples using 5 MeV Si^{4+} primary ions. Around 2×10^{12} ions/cm² the yields reach the same level indicating that the surface contamination on sample A has been removed.

The result of this experiment illustrates the problems with using the definition of the damage cross section in formula 5.3.3.A. For two samples made using the same sample preparation method and the same experimental setup and primary ion, completely different damage cross sections can be obtained.

The reason for this discrepancy in this case is the different surface condition for both samples. An oxygen contamination of the surface, for example, can change the secondary ion yield in SIMS significantly [94] and the quick decrease to a common level hints to a surface contamination being the reason for the increased yield.

Additionally, the interaction between the sample and the primary ion and the processes initiated by the primary ion impact are more complex than simply breaking up molecular bonds. Aside from breaking up molecular bonds, new connections can be produced, an effect known as cross linking which finds its application i.e. in ion beam lithography techniques.

Moving on to higher primary ion fluencies the effects of cross linking and fragmentation can be observed. Experiments have been performed on Glycine, Arginine and Leucine and are presented in the following figures.

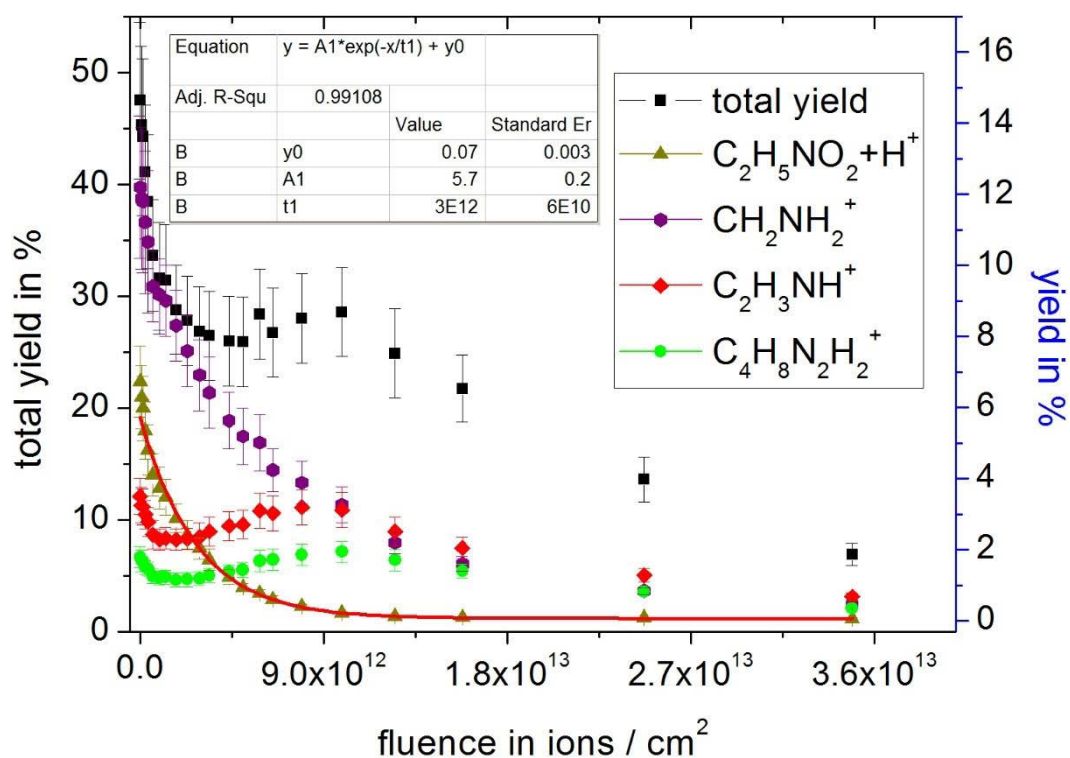


Figure 5-3-3-2: Dynamic SIMS of a Glycine target using 8 MeV Si^{4+} primary ions. The 76 Da molecular ion intensity decreases monotonously, as the applied fluence increases. The total yield though has a second maximum at 10^{13} ions/ cm^2 . This is most likely caused by the formation of new molecules from the fragments of the already damaged area. The damage cross section calculated according to formula 5.3.3.A. is: $\sigma = (0.365 \pm 0.008) \times 10^{-12} \text{ cm}^2$.

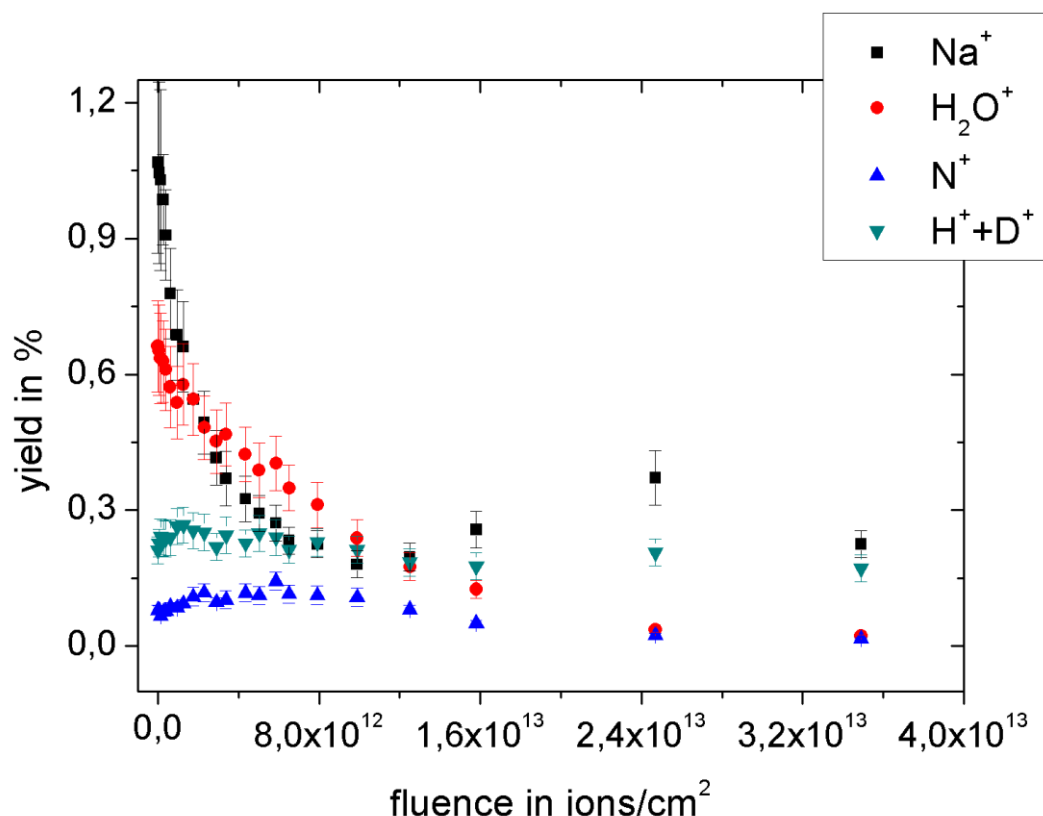


Figure 5-3-3-3: The low mass signals from the same Glycine target as in figure 5-2-3-3. The sodium signal is quite interesting as it shows a decrease following the decrease of the molecular ion yield and then a new increase to a second maximum. This hints to the fact that the surface of the substrate was reached. First the sodium bound in the evaporated Glycine layer is desorbed. Afterwards sodium is desorbed from the contamination within the interface between the top layer and the substrate [95]. The hydrogen and deuterium signal show a similar behaviour while water and nitrogen stem mostly from the evaporated layer.

Figure 5-3-3-2 and 5-3-3-3 show that there is even some increase in yield under irradiation. The most likely reason for such behaviour is the effect of cross linking and production of new molecules under ion bombardment. The damage cross section of $(2.74 \pm 0.06) \times 10^{12}$ ions/cm² and the crater depth of (20 ± 10) nm [96, 97] found in earlier works supports the assumption that the final overall decrease of yield can be interpreted as reaching the silicon wafer substrate. Figure 5-3-3-4 shows a comparison of the mass spectrum from a pristine sample to a mass spectrum obtained at the second local yield maximum at 10^{13} ions/cm². Well visible in the blue spectrum are the groups of fragments that rise in intensity compared to the molecular peaks.

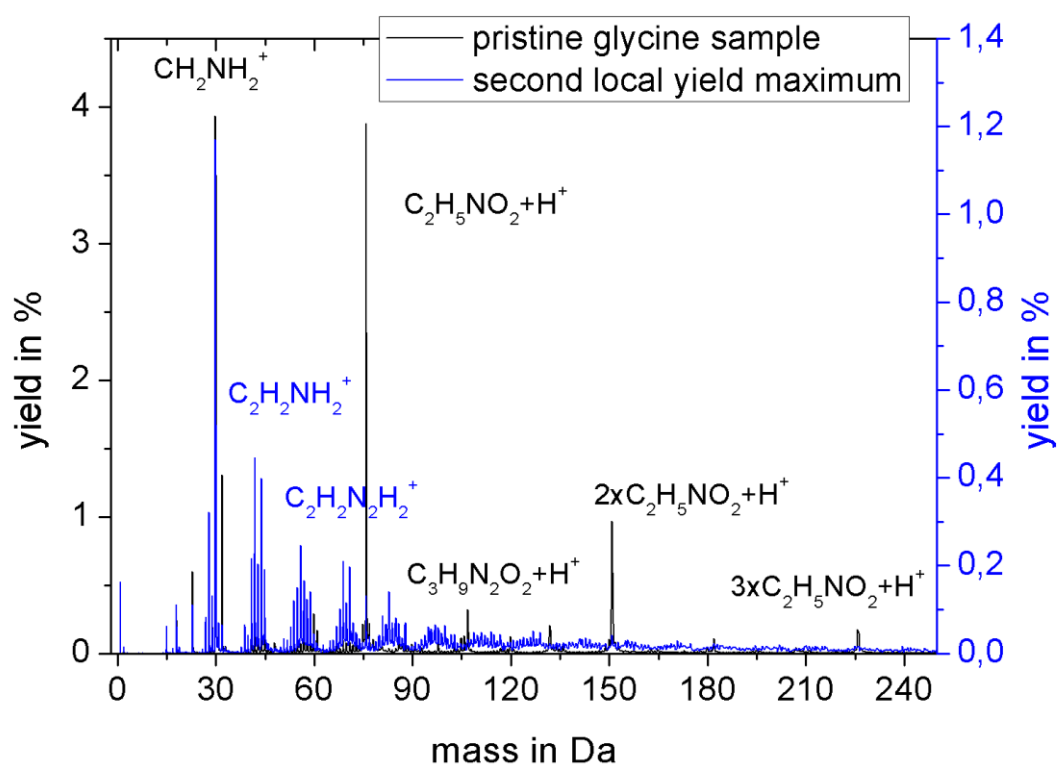


Figure 5-3-3-4: The new molecules formed under bombardment with 8 MeV Si^{4+} primary ions.

The molecular peaks for which we can observe an increase in their intensity and/or that appear are produced through new bonds formed by radicals. The final decrease of intensity for all peaks is likely caused by the sample being sputtered away and thinning out similar to the effect shown in Appendix B.

The same experiment was performed on an Arginine sample. Figure 5-3-3-5 shows the spectra obtained at the start and at the second local yield maximum as presented for Glycine.

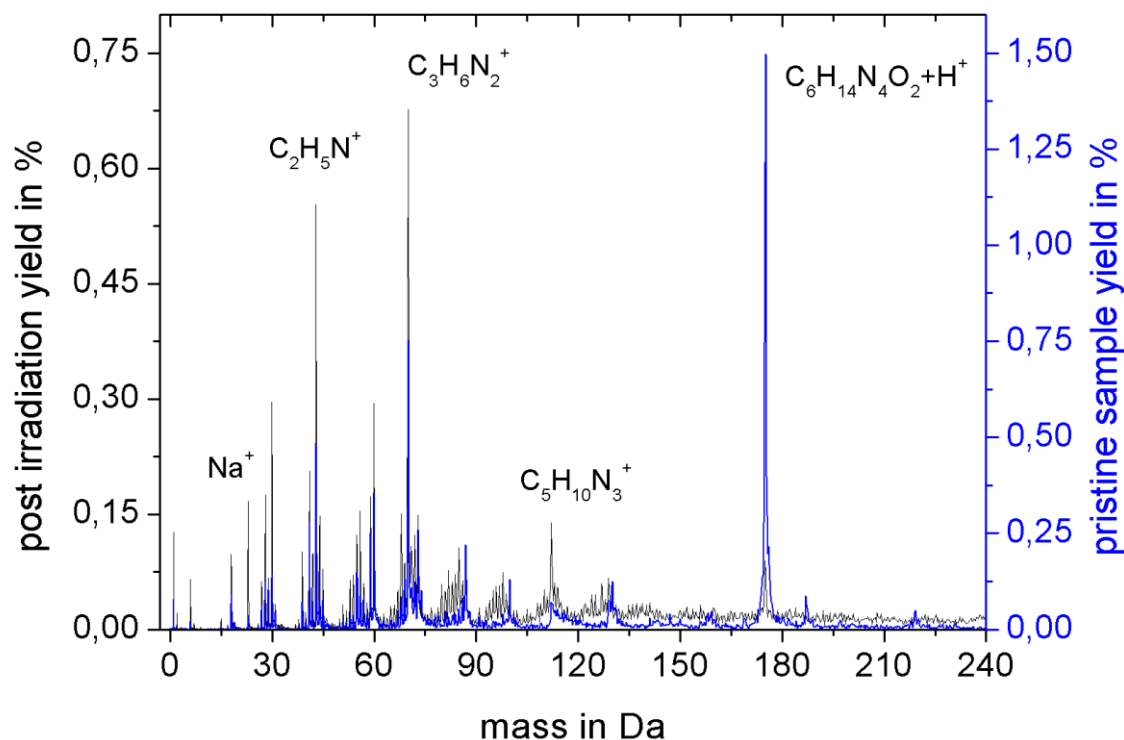


Figure 5-3-3-5: The new molecules formed under bombardment of Arginine with 9 MeV O^{4+} primary ions.

This spectrum has a well visible Na-peak. It shows an interesting behaviour as the sodium peak increases during the measurements (figure 5-3-3-6). This can be attributed to sodium bound in the Arginine or from the surface of the silicon wafer [95]. Based on similar behaviour seen from the experiment performed on Glycine in figure 5-3-3-3, it can be concluded that this sodium signal originates from the surface of the wafer as the sodium peak of a contamination in the glycine sample had a higher intensity while the intensity of the sodium peak at high fluences is the same.

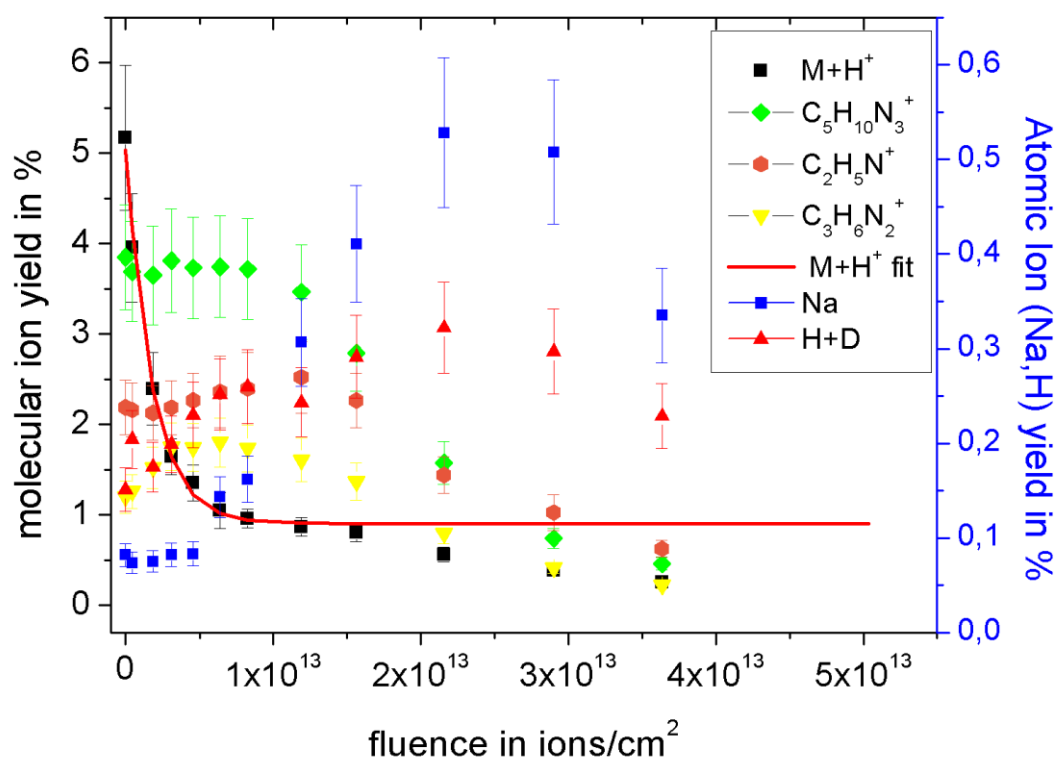


Figure 5-3-3-6: The yield fluence dependence for various molecular and atomic ions obtained under bombardment of Arginine with 9 MeV O^{4+} primary ions. The Arginine yield decreases exponentially and flattens of at certain fluence. Its damage cross section would be $(0.6 \pm 0.2) \times 10^{-12} \text{ cm}^2$. Sodium and hydrogen yields increase as the molecular peak decreases.

In addition to the amino acids Arginine and Glycine, Leucine was irradiated as well. Again, a local maximum is reached, with an observable variation for the relative intensities between the characteristic peaks compared to the pristine sample (figure 5-3-3-7). An interval with stable yield for some peaks exists for fluence between 10^{13} ions/cm² and 2×10^{13} ions/cm² followed by a linear decrease (figure 5-3-3-8). This again can be attributed to desorption of the target reaching levels where the surface of the substrate is reached.

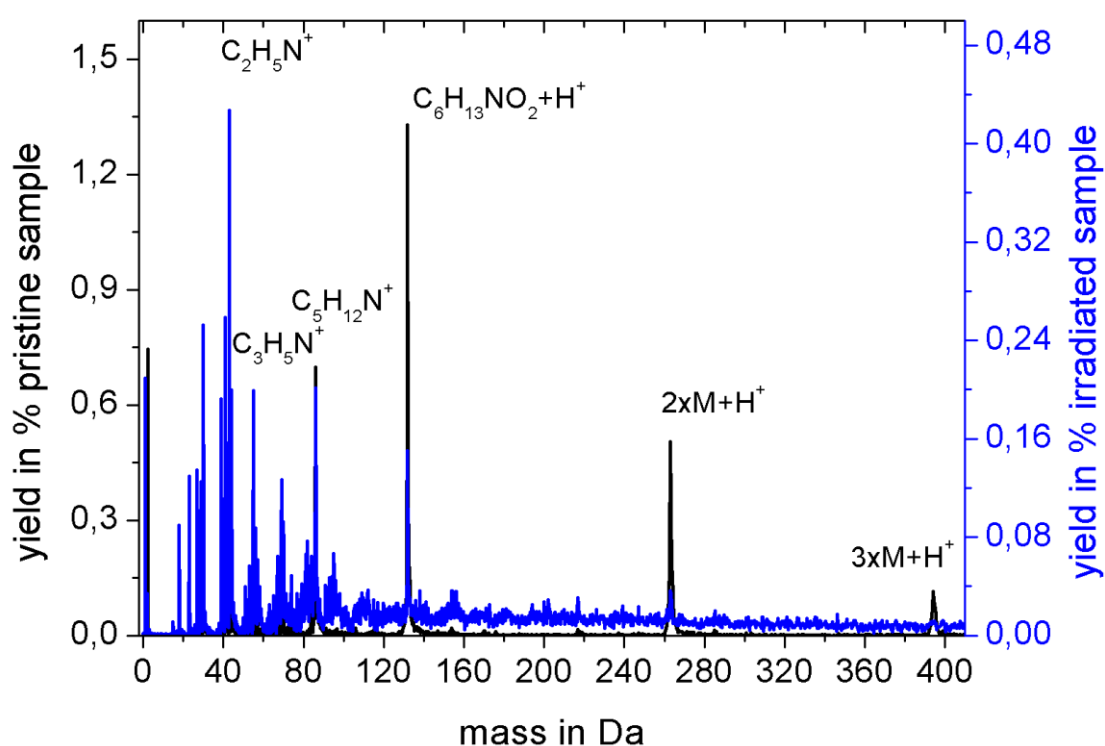


Figure 5-3-3-7: Mass spectrum of a pristine Leucine sample and the same sample after irradiation with 8.4×10^{12} ions/cm². The molecular peaks decrease in intensity while the fragments from the damaged areas increase.

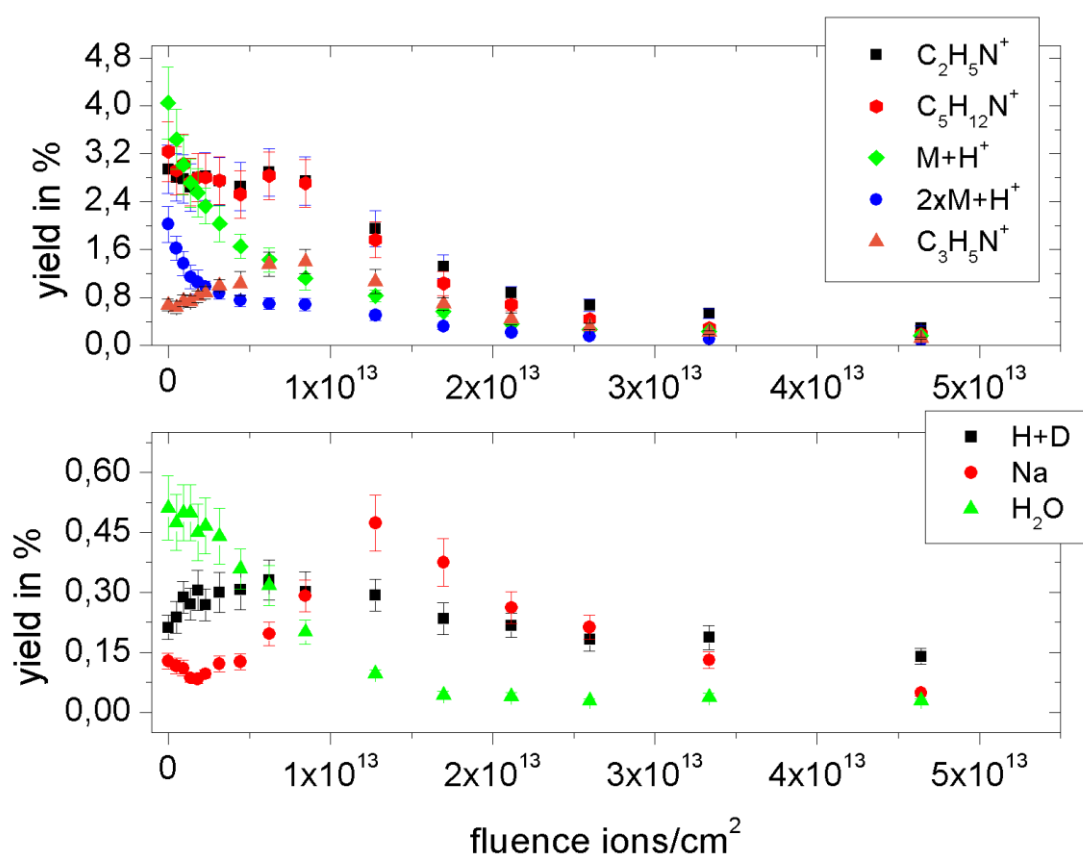


Figure 5-3-3-8: Selected peaks of the Leucine mass spectrum and their yield evolution depending on the 8 MeV Si^{4+} primary ion fluence. Water and the molecular ions show a monotone decrease while sodium has a peak at fluences around 10^{13} ions/cm². The damage cross section is similar to Glycine with $(0.4 \pm 0.03) \times 10^{-12} \text{ cm}^2$ for the single Leucine peak and $(0.7 \pm 0.04) \times 10^{-12} \text{ cm}^2$ for the peak of di-Leucine.

The Leucine sample shows the same trend as Arginine and Glycine which is reasonable as all three are amino acids. The H_2O signal decreases with the molecular ion and the atomic ions of hydrogen and sodium have a local maximum at high fluences indicating that one has reached the surface layer of the wafer. This way these measurements can be interpreted as double layer dynamic SIMS measurements with the evaporated material on top of a “contamination” layer, which shows up in the measurements.

5.3.4 Summary

The study of the fluence dependence of the MeV SIMS secondary ion yield has shown that fluences that would be just at the static limit for keV-SIMS (10^{11} ions/cm² to 10^{13} ions/cm²) and only change the sample characteristics slightly, are enough to produce craters of 30 nm depth in MeV SIMS.

A further look at the behaviour of the MeV SIMS secondary ion yield at lower fluences reveals a static limit for Leucine below 2×10^{10} ions/cm².

Looking at the dynamic SIMS regime, the interaction intensity and penetration depth of MeV-ions makes it seem impossible to do depth profiling with MeV SIMS. The study of the secondary ion yield behaviour in the dynamic SIMS regime in chapter 5.3.3 though shows that there is a possibility for dynamic MeV SIMS depth profiling:

After an exponential decrease of the yield for fluences up to a value between 5×10^{12} ions/cm² and 9×10^{12} ions/cm² there is a stable region of secondary ion yield for the characteristic molecules of a material as well as an increase of fragments that belong to it. Once a layer has been desorbed completely the yields for the characteristic molecule and the fragments decrease.

It was also possible to identify the layer below the top layer as the signal of contaminations from the Si-base, i.e. Sodium increased after the signals from the top layer decreased to similar value for all samples while being varied at the start of the measurement (table 5-3-4-1). These results are the motivation for testing the capabilities of MeV SIMS on multi-layer samples.

sample	Na-yield at start in ‰	Na-yield at second maximum in ‰	
Glycine	11±2	3.6±0.5	2,4
Arginine	0.7±0.1	5.2±0.8	2,25
Leucine	1.2±0.2	4.2±0.6	1,25

Table 5-3-4-1: Sodium yield at the start (sample surface) and at the second yield maximum (wafer surface) of the dynamic SIMS experiments.

5.4 MeV SIMS on multi-layer samples

Multi-layer samples are commonly investigated in keV SIMS [98]. Either to gain information about the depth profile of a sample or as part of a yield enhancing technique called Metal assisted (MetA) SIMS. In this case a thin layer evaporated on top of the sample surface can enhance the secondary ion yield while also changing the mass spectrum [99]. After the results from the previous chapter, it is interesting to explore the possibilities MeV SIMS offers in this field. The enhanced yield for organic molecular ions is useful i.e. for the analysis of organic solar cells. Accordingly, two types of sample have been tested: thin layers of metal on top of the analyte and a real well defined two-layer sample.

5.4.1 MeV SIMS on PS/PMMA double layer sample

In order to explore the possibilities of depth profiling using MeV SIMS in analogy to dynamic keV SIMS, a well-defined double layer of Polystyrene (PS) on Polymethylmethacrylate (PMMA) has been prepared at the KU Leuven by Vanina Cristuado. The thickness of each layer was (100 ± 10) nm, determined by Ellipsometry [100]. The goal now was to apply enough fluence to the sample to fully desorb the top layer and see a clear PMMA spectrum. Figure 5-4-1-1 shows the spectra before and after irradiation with 8 MeV Si^{4+} primary ions as well as the mass spectrum of PMMA.

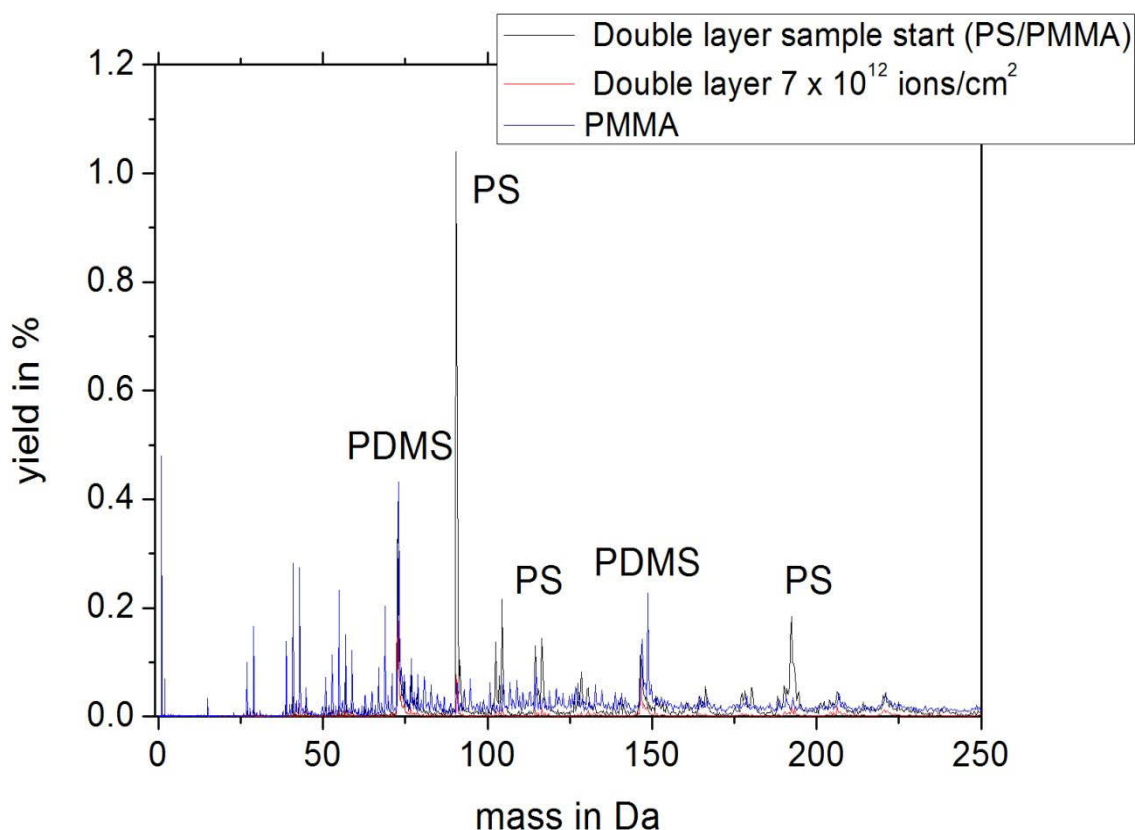


Figure 5-4-1-1: The spectra of the double layer compared to a PMMA sample. The dose on the sample wasn't sufficient to reach the layer below the Polystyrene layer. The characteristic PS peaks lose 90 % and more of their intensity while peaks that can be attributed to PDMS contamination loose only about 40 %.

Unfortunately, the fluence applied on the sample was too low to reach the PMMA layer below the PS layer. This is in good agreement with the high primary ion fluence SIMS experiments from the previous chapter, which suggest that more fluence is necessary to sputter away a 100 nm layer. Table 5-4-1-1 shows the change of yield for certain characteristic peaks for the spectra after irradiation with 7×10^{12} ions/cm² 8 MeV Si⁴⁺.

Mass in Da	Parent molecule	Starting yield in %	End yield in %	End yield / start yield in %
73	PDMS (Si(CH ₃) ₃)	3.4±0.5	2.1±0.3	62.5
91	PS (C ₇ H ₇)	8.8±0.7	0.7±0.1	7.7
117	PS (C ₉ H ₉)	1.2±0.2	0.09±0.001	7.1
147	PDMS (Si ₂ O(CH ₃) ₅)	0.9±0.1	0.6±0.05	70
193	PS (C ₁₅ H ₁₃)	1.5±0.2	0.2±0.03	11

Table 5-4-1-1: Change of the peak intensity after irradiation. The PDMS peaks are much less influenced by the irradiation while the PS yield declines down to about 10 % of its starting value

What can be seen from these measurements is that a 100 nm layer of PS is thick enough to stop any signal from the PMMA layer below and that the irradiation up to 7×10^{12} ions/cm² does not lead to any migration of the PMMA into the top layer.

Additionally, the different decrease for PDMS and PS peaks shows the different damage cross section for both ions in their composition as the PS secondary ion yield decreases much stronger after irradiation.

5.4.2 Spectra of metalized Leucine samples

Deposition of a thin layer of gold or any other metal on the analysed sample before the measurement is known in the keV SIMS community as metal assisted SIMS (MetA SIMS).

Two samples were prepared through evaporation for investigation how such samples behave in MeV SIMS measurements. A thin gold layer on top of Leucine and a copper layer evaporated on top of a thin gold and a thick Leucine layer were prepared.

The resulting spectra after irradiation with 8 MeV Si^{4+} primary ions are shown in the figures 5-4-2-1 and 5-4-2-2. The spectrum shown in figure 5-4-2-1 is the first application of this technique to MeV SIMS. The yield was not measured in this case. One can see that the metal layer leads to a higher fragmentation of the Leucine desorbed from the sample, an effect not known in keV MetA SIMS [101]. The ratio between the different clusters of Leucine is the same though.

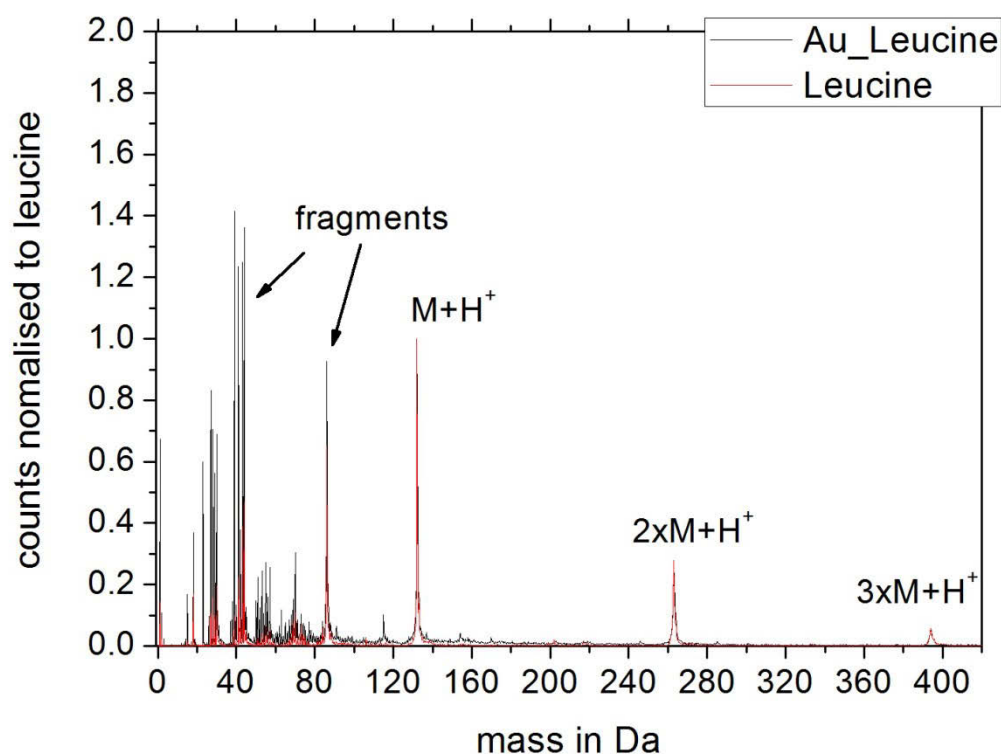


Figure 5-4-2-1: Effect of a thin gold layer on a Leucine spectrum. The primary Ion is 8 MeV Si^{4+} . The number and relative yield of the lighter mass fragments is increased which may be caused by the passage of Leucine ions through the gold layer.

Now as this sample still showed the characteristic Leucine peaks, another layer of copper was evaporated on top. The resulting spectrum was very different to the usual Leucine Spectrum. New high mass peaks appear which can be interpreted as a Leucine-copper complex. After irradiation with an 8 MeV Si^{4+} ion beam the intensities of these peaks decrease, possibly because the gold-Leucine layer below the copper rich top layer has been reached. An alternative explanation for the decrease could be the normal decrease of yield for molecular ions compared to fragments, already observed in the previous chapters.

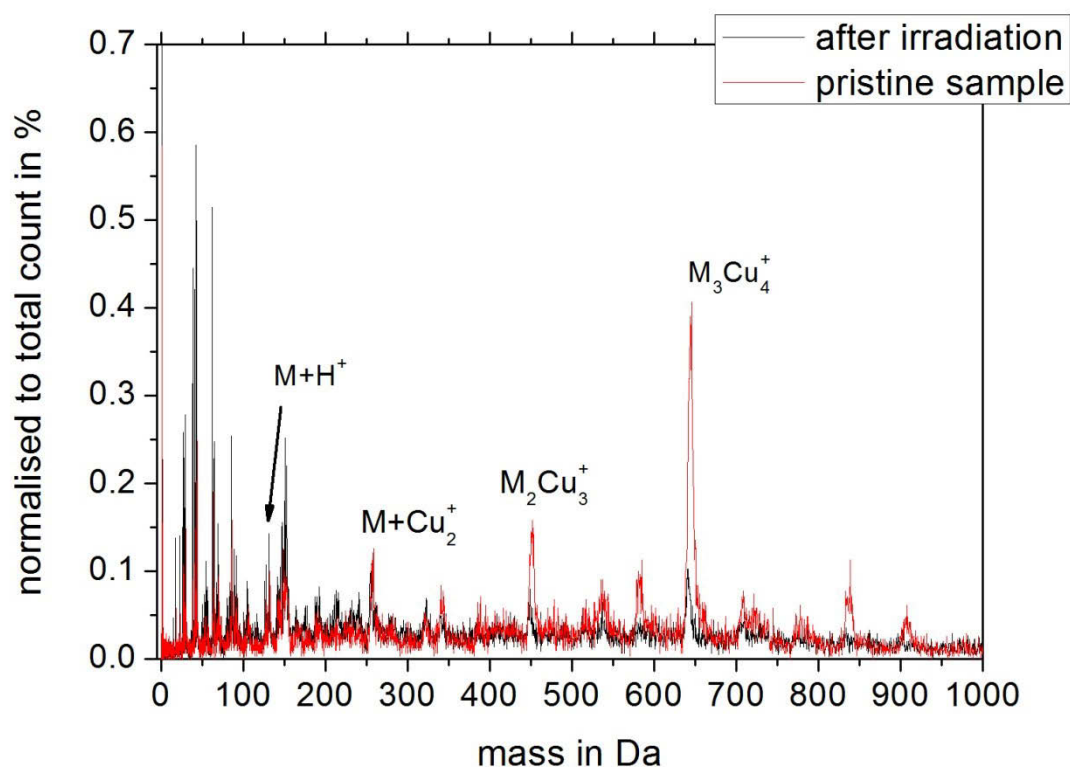


Figure 5-4-2-2: Spectrum of the Cu_Au_Leucine sample normalised to the total amount of secondary ions collected. In red the pristine sample and in black the sample after irradiation. The primary ion is 8 MeV Si^{4+} .

5.4.3 Summary

The multi-layer MeV SIMS tests on the PS/PMMA sample with known layer thickness is in good agreement with the dynamic SIMS experiments from chapter 5.3. The fluence of 7×10^{12} ions/cm² was not enough to desorb the upper PS layer with 100 nm thickness as was the case for the samples tested in chapter 5.3. Accordingly, there is no PMMA signal visible in the spectrum. Also present in the sample was a PDMS a contamination which was much more resistant to radiation damage than the PS.

The test of MeV MeTA SIMS on Leucine showed that a thin gold layer simply introduces more fragmentation into the spectrum while a thin copper layer introduces composite peaks of copper and Leucine ($\text{M}_x\text{Cu}_{x+1}^+$) with a relative intensity of these composite peaks that is up to 3 times higher (in the case of M_3Cu_4^+ then the simple characteristic peak of Leucine in this spectrum).

As one can see, the evaporation of copper on the sample surface can be a way to increase the yield of bigger molecule clusters in MeV SIMS if the molecule in question can bind copper atoms.

5.5 MeV SIMS of mixed samples

A technique commonly used in keV SIMS is standard based quantification [102, 103]. So far there has been no investigation into the possibilities for standard based MeV SIMS and thus a first proof of principle experiment was performed at the RBI. The results are presented here.

5.5.1 Production of mixed samples

The samples for the experiment were produced in the same evaporator as described in chapter 5.1, but instead of only one compound, mixtures of Leucine and Glycine as well as of two pigments based on phthalocyanine called PB 15:3 (blue) and PV 19 (red) were used. The materials were chosen for their similarity in matrix material. The mixtures were obtained by simply shaking the powders together. Afterwards the mixtures were evaporated which further helped the mixing. The process of evaporation itself as well as the deposition, lead to a certain mixture of the compounds on the sample which was not determined before the MeV SIMS measurements.

5.5.2 Yields of mixed samples

The spectra for the mixed samples obtained with an 8 MeV Si^{4+} can be seen in figure 5-5-2-1 and 5-5-2-2. The characteristic peaks for booth materials are visible.

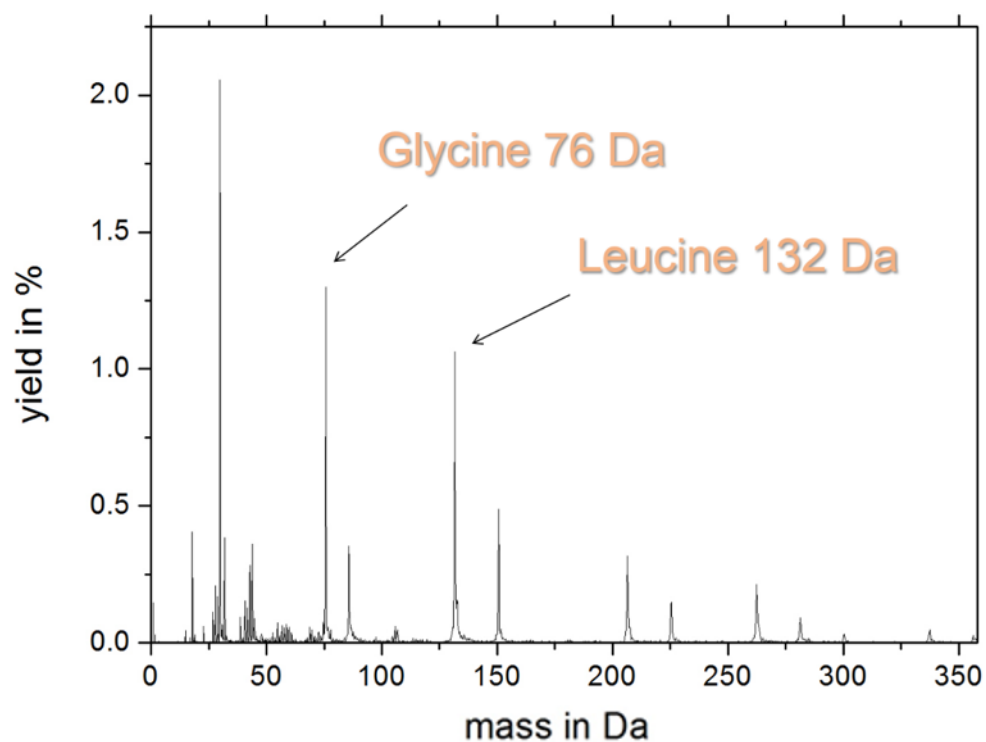


Figure 5-5-2-1: Yield achieved for the Glycine-Leucine mix tested. The molecular peaks of Leucine at 132 Da and of Glycine at 76 Da as well as their molecular combinations are clearly visible.

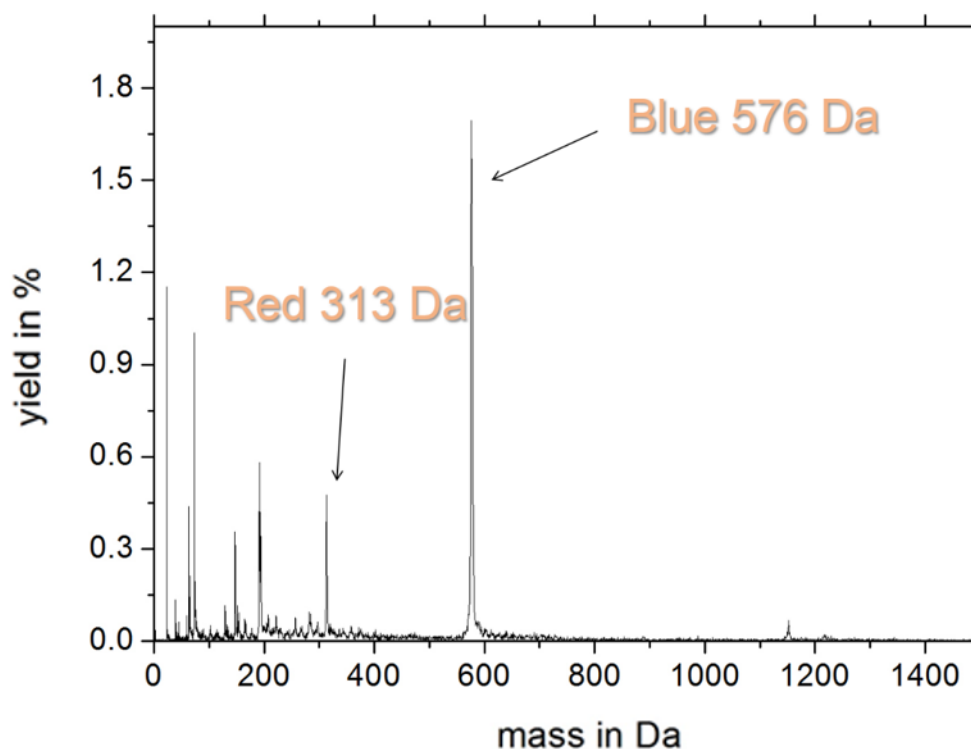


Figure 5-5-2-2: Yield obtained for the pigment mixture. Here also the characteristic molecular peaks for both pigments are present.

The mixture for the amino acid sample was 42 mol % Leucine and 58 mol % Glycine evaporated on silicon and the yields achieved were 3.4 % Glycine and 3.9 % Leucine. The yield values for pure samples are 11 % for Glycine and 5.4 % for Leucine, taken from the averages of pure sample measurements obtained while working on this thesis. Assuming a linear connection of the yields to the number of molecules in the sample and a homogenous sample we can calculate the sample composition from the secondary ion yields with:

$$X_i = \frac{N_i}{N_{total}} = \frac{R_i \times N_{i0}}{\sum R_i \times N_{i0}} = \frac{R_i \times \rho_i^N}{\sum R_i \times \rho_i^N}$$

$$\text{and } R_i = \frac{N_i}{N_{i0}}.$$

Here N_{total} is the number of molecules in the measured volume of the mixed sample, N_i the number of ions of one type in the measured volume for the mixed sample, N_{i0} the number of ions of the same type in the same volume in a pure sample, ρ_i^N the number of ions in a pure sample per cm^3 assuming we have a homogenous sample and R_i is the ratio of the yield for the selected molecule in the mixed sample as compared to the pure sample.

This leads to a composition of $X_L = (60 \pm 7) \text{ mol } \%$ for Leucine and $X_G = (40 \pm 7) \text{ mol } \%$ for Glycine.

For the pigment mix sample, the composition of the mix before evaporation was 65 mol % PB 15:3 and 35 mol % PV 19 pigments. The obtained yield ratio R_i was 82 % of the pure sample yield for PB 15:3 (blue) and 19 % of the pure sample yield for PV 19 (red). The same calculations as above lead to a molecular ratio X_i between the pigments of $X_{PB15:3} = (71 \pm 6) \text{ mol } \%$ for PB 15:3 and $X_{PV19} = (29 \pm 6) \text{ mol } \%$ for PV 19.

Considering the error of the yield measurement established earlier, the results of the measurement agree with the composition of the mix before evaporation for the pigments. For Leucine and Glycine, the results of the quantification do not fit to the assumed composition of the sample.

The reasons for this discrepancy are the use of pure sample values that have not been obtained at the same day with the mixed sample yields and the fact that the composition of the powder is not necessarily the composition of the mix deposited silicon wafer.

For a good quantification, the pure sample standards must be measured under the same conditions. Using internal standards measured on the same sample holder with the mixed samples is advisable.

6 MeV SIMS Applications

In this chapter, four applications for MeV SIMS will be presented that show the wide range of uses for this analysis technique. A Forensics application and a RoHS compliance-check application have been tested to show possible uses for MeV SIMS and a material science as well as a cultural heritage application show how MeV SIMS can help solving questions from different fields of research.

6.1 Application I: Forensics

One advantage of MeV SIMS is its sensitivity and small amount needed to analyse elemental and/or molecular content. This characteristic of the technique may be interesting for applications in forensics where samples are quite often microscopic and unique.

An example that could come up during criminal investigations might be the question, who wrote on a document first and if a document has been changed afterwards with another pen. This case was simulated, to explore the capability of MeV SIMS to solve such a problem. A red and a blue pencil with distinctly different mass spectra were used to deposit ink on paper (Fornex premium) by handwriting.

A single blue, a single red and a red stripe crossing over a blue one, were prepared. The centre of the cross formed in the latter case was almost black, making it impossible to discern by eye which colour was on top.

In order to determine what ink was on top, first a spectrum of the paper without ink on it was taken using an 8 MeV Si^{4+} primary ion beam. It confirms to the spectra obtained during keV-SIMS for cellulose (figure 6-1-1):

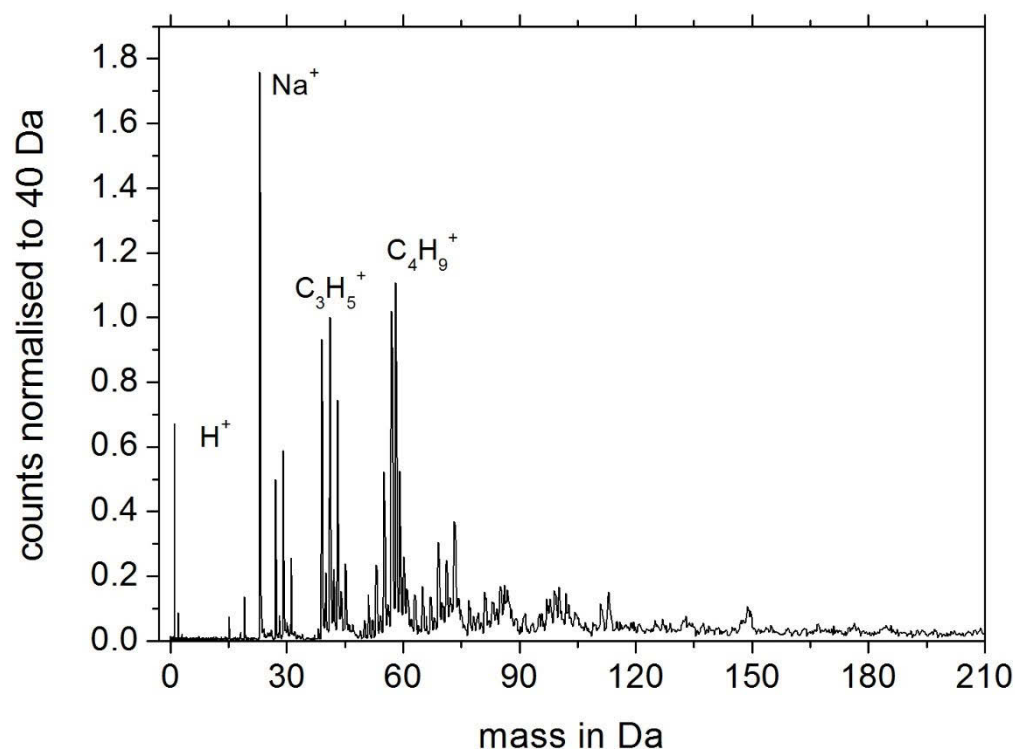


Figure 6-1-1 Spectrum of paper showing the characteristic cellulose spectrum. The scan area was $300\ \mu\text{m} \times 300\ \mu\text{m}$ and the primary ion was $8\ \text{MeV}\ \text{Si}^{4+}$.

Then the red and the blue ink on the paper were measured. The spectra were taken from single lines written on the previously analysed Paper with scan areas of $300\ \mu\text{m} \times 300\ \mu\text{m}$ using $8\ \text{MeV}\ \text{Si}^{4+}$. Figure 6-1-2 shows the red ink produces a distinct peak group around 450 Da and the blue ink has a single peak around 470 Da and a distinctive Peak group in the 320 Da to 480 Da interval.

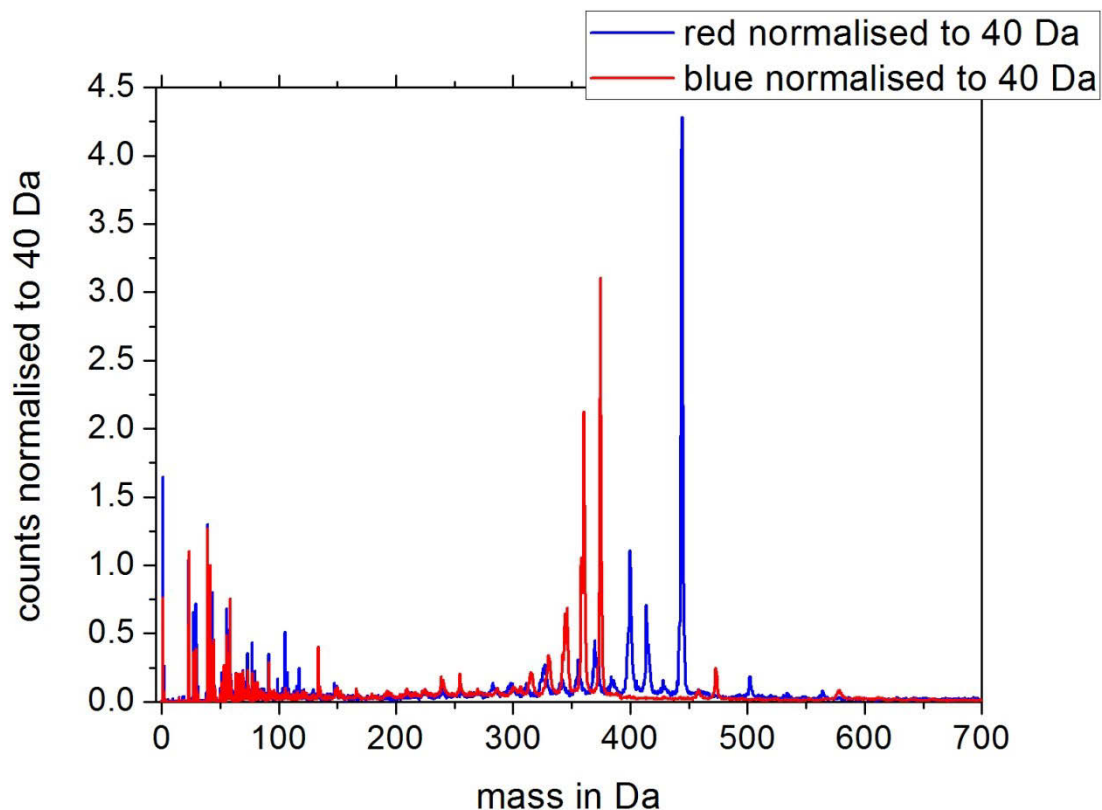


Figure 6-1-2: Spectrum of inks used with red ink in blue and blue ink in red. Both spectra were normalised to the 40 Da peak using an 8 MeV Si^{4+} primary ion beam on a $300\text{ }\mu\text{m} \times 300\text{ }\mu\text{m}$ scan area.

After these standard spectra had been recorded a mapping of the intersection of the two lines crossing was taken. Figure 6-1-3 shows how such a cross looks and the total MeV SIMS counts obtained during the mapping. It is impossible to discern with the eye which colour is on top but a look at the MeV SIMS spectrum for different areas shows distinctly different mass spectra.

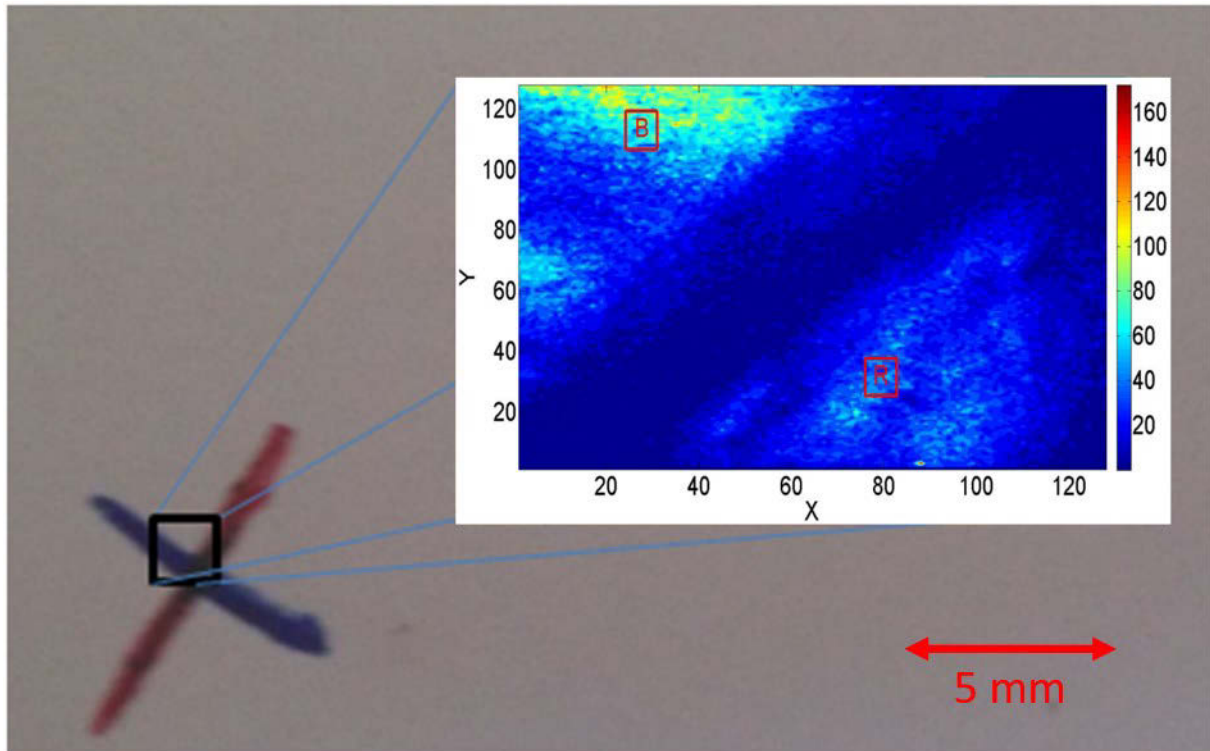


Figure 6-1-3: The sample area investigated during the scan. B and R show the areas of blue ink and red ink. The total signal during the scan obtained using 8 MeV Si^{4+} primary ions was used for the map and the scan size was 1 mm x 1 mm. The picture shows a reproduction of the sample to picture the problem.

The total secondary ion count has a minimum at the crossing. This is caused by the bending of the paper when the ink was applied very generously. The resulting change of angle between extractor and sample is illustrated in the sketch in figure 6-1-4. It changes to a value which is far away from the optimum angle in the bend area and as has been shown in chapter 5.1.1., deviations from this angle produce a drop in the secondary ion yield. Looking at the mapping shown in figure 6-1-3 one can also see that the area of low intensity has a direction along the red line on the paper. This hints to the fact that the red ink was deposited last introducing the final bending on the paper. As we will see in the spectra taken from the crossing this assumption is correct.

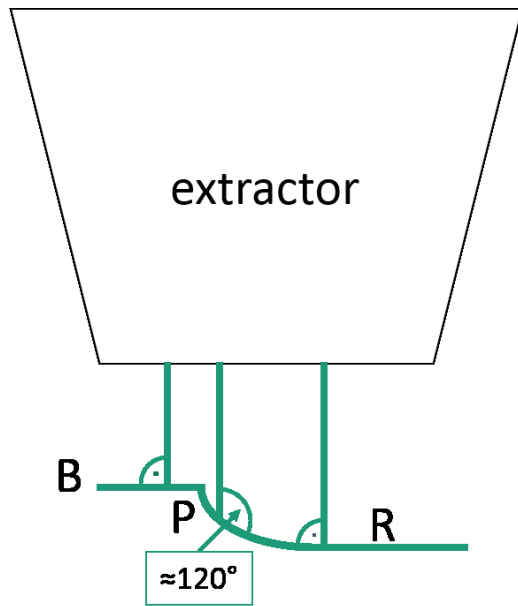


Figure 6-1-4: the sample morphology of the ink cross showing the reason for the yield drop at the crossing. While the angle to the extractor is optimised at the areas B and R around 90° it is far from the optimum in the bend area where it is approximately 120°.

100 μm x 100 μm scans of the areas marked R and B in figure 6-1-3 were obtained using 8 MeV Si^{4+} primary ion beams, to identify the ink present in areas around the intersection and at the centre of the crossing itself. The spectra were then compared to the standard spectra for the pure ink on paper in figure 6-1-5. The comparison shows clearly that the red ink is on top in the cross centre.

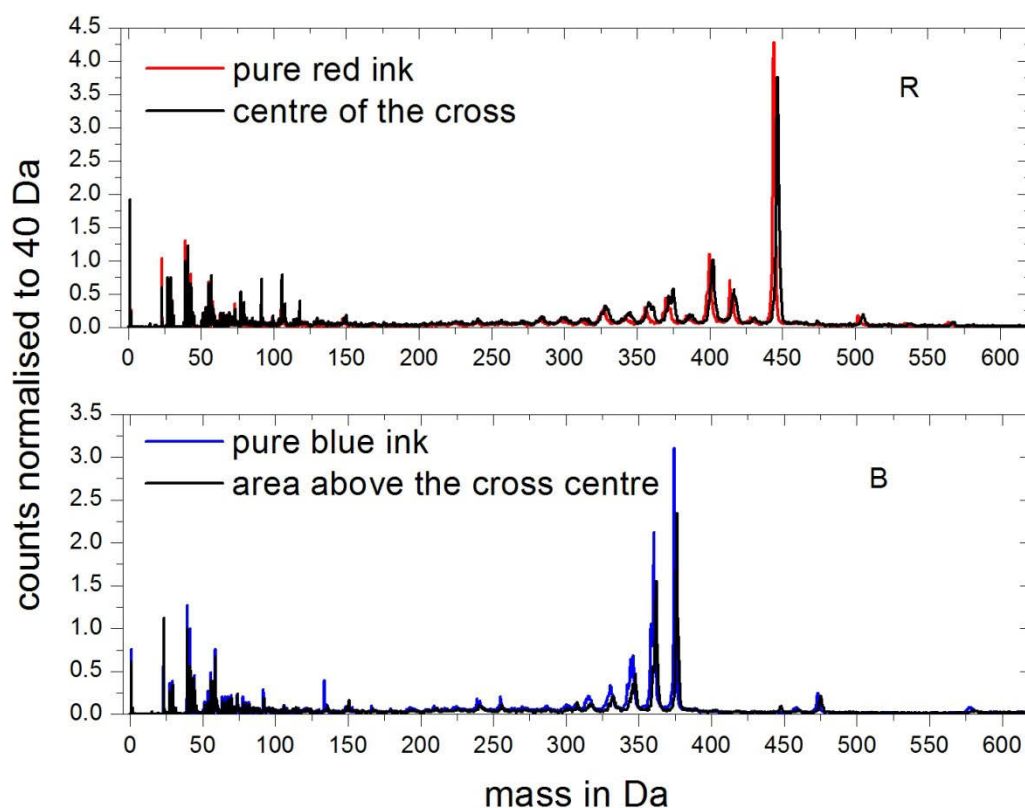


Figure 6-1-5: The spectra taken from the two 100 μm x 100 μm areas near the cross centre. While it is impossible to see which ink is on top by just looking at the sample with the eye, the spectra clearly show the red ink is on top at the centre of the cross.

The results of this experiment prove that MeV SIMS can be used in this forensics application and in many other forensic cases where molecular content mappings can help solving the puzzle. In this particular case, it has to be applied with caution though, as the inks have to be well discernible in their mass spectra.

6.2 Application II: Study of post-Byzantine Albanian Orthodox Church icons

In south eastern Albania around Korçë, in the province with the same name, one can find a rich heritage of post-Byzantine orthodox iconography. Some of the most prolific examples are presented (example in figure 6-2-1) in the collection of the National Museum of Medieval Art (NMMA).

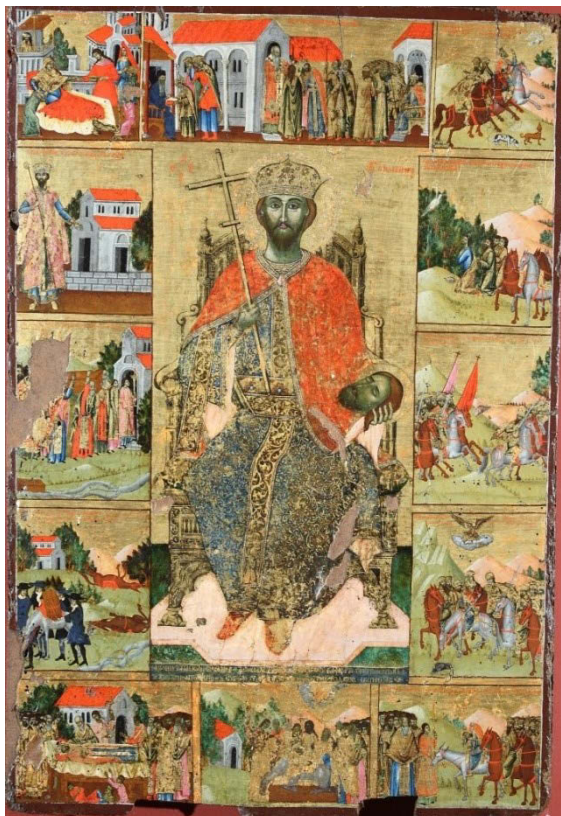


Figure 6-2-1: An example of the icons that can be found in the NMMA Korçë museum: The Icon of Saint Jovan Vladimir painted by Kostandin Shpataraku, from the Ardenica Monastery in Albania. The sample investigated is from a similar picture from a gold-plated area comparable to the ones visible in the picture.

The office for icon restoration of the NMMA works on the conservation of the museums' icons and has supplied part of an icon in storage to analyse the varnish used to seal the icons surface. The conservation specialists suspected some kind of natural resin and were asking for data to support or disprove their assumption. Figure 6-2-2 shows the sum of two MeV SIMS spectra obtained of different spots (spot size 20 μm) on the sample.

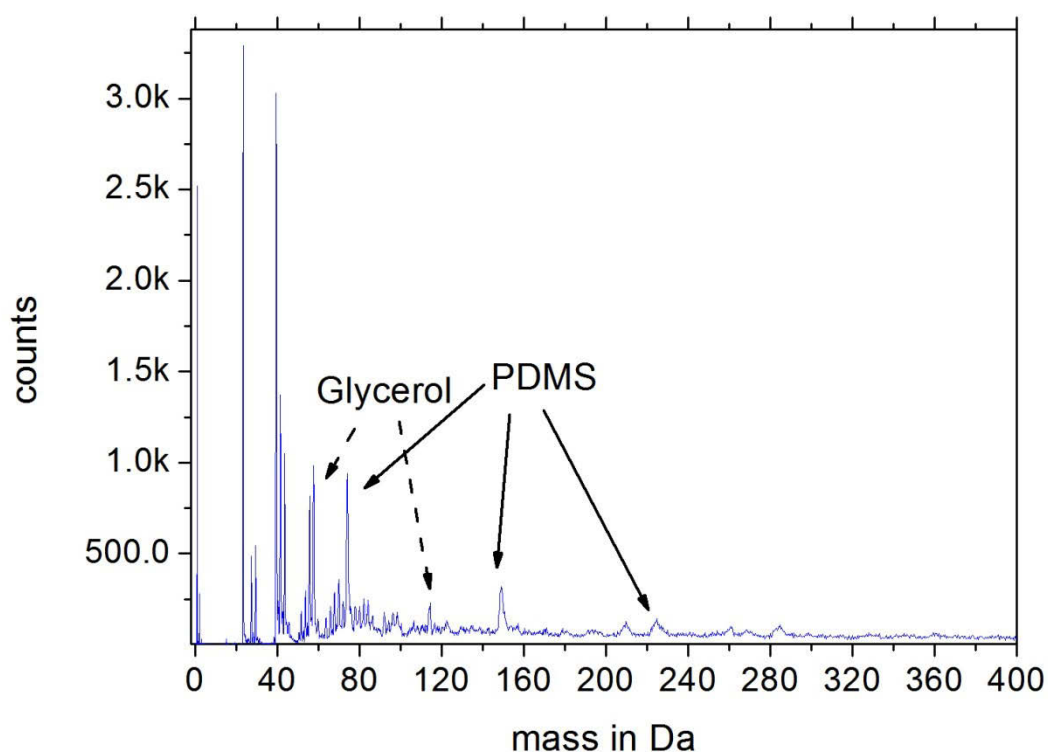


Figure 6-2-2: Sum mass spectrum from two measurements on the icon gold chip surface. The sample shows contamination with sodium to a high degree and characteristic PDMS peaks.

A study of icons from a similar time-period was performed on post-Byzantine icons from the area around Mount Athos on the Peloponnese and Thessaloniki [104]. It finds vegetable oils in 15 out of 24 samples and the resin colophony in all but two of the samples analysed which instead showed the signature peaks of Venice turpentine.

Now looking at the MeV SIMS spectrum of the varnish taken from the stored Icon there is the problem of a PDMS contamination introducing many peaks as well as the Sodium peak at 23 Da. The sample was contaminated during the transport from Korçë because a plastic container was used, which once again shows how important sample handling is for MeV SIMS, as any contamination can produce misleading results. What can be seen though, are the characteristic mass peaks of glycerol [105], which is not present in the plastic container. This hints of the usage of vegetable oil in the varnish, assuming there is no other source of contamination. Further measurements are necessary to identify characteristic groups for the other components. The sample's surface can be cleaned by irradiation before the next measurements, if the varnish is as stable as the PMMA investigated in the next chapter.

6.3 Application III: Study of the fragmentation and cross-linking effects in PMMA

Polymethylmethacrylate (PMMA), also known as acrylic glass or under its trade name Plexiglass, is mainly used as glass substitute. Additionally, it is used in the industry as resist for lithography.

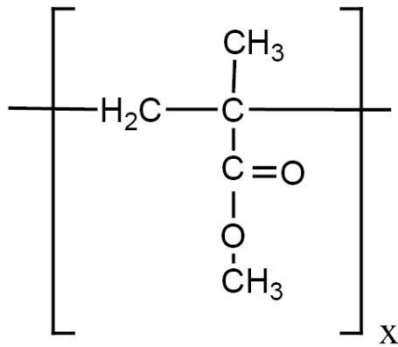


Figure 6-3-1: Unit cell of PMMA. The side branches provide the rigidity of the material.

The change of PMMA from positive to negative resist for MeV Ion beam lithography has been investigated by R. Norarat in her PhD thesis [92]. During the investigation, the question which processes lead to the change of characteristics from positive to negative resist came up. One explanation for the change can be cross linking, the production of new connections between molecules, damaged by the ion beam.

In order to get more information on the type of molecules formed, a sample of PMMA on a Silicon wafer substrate was investigated by MeV SIMS. The sample was analysed and irradiated with 5 MeV Si⁴⁺ ions. The resulting spectra for the pristine sample as well as the spectra obtained after irradiation are shown in figure 6-3-2. The characteristic peaks of PMMA are the two fragments at 41 Da (C₃H₅⁺) and 69 Da (C₄H₅O⁺).

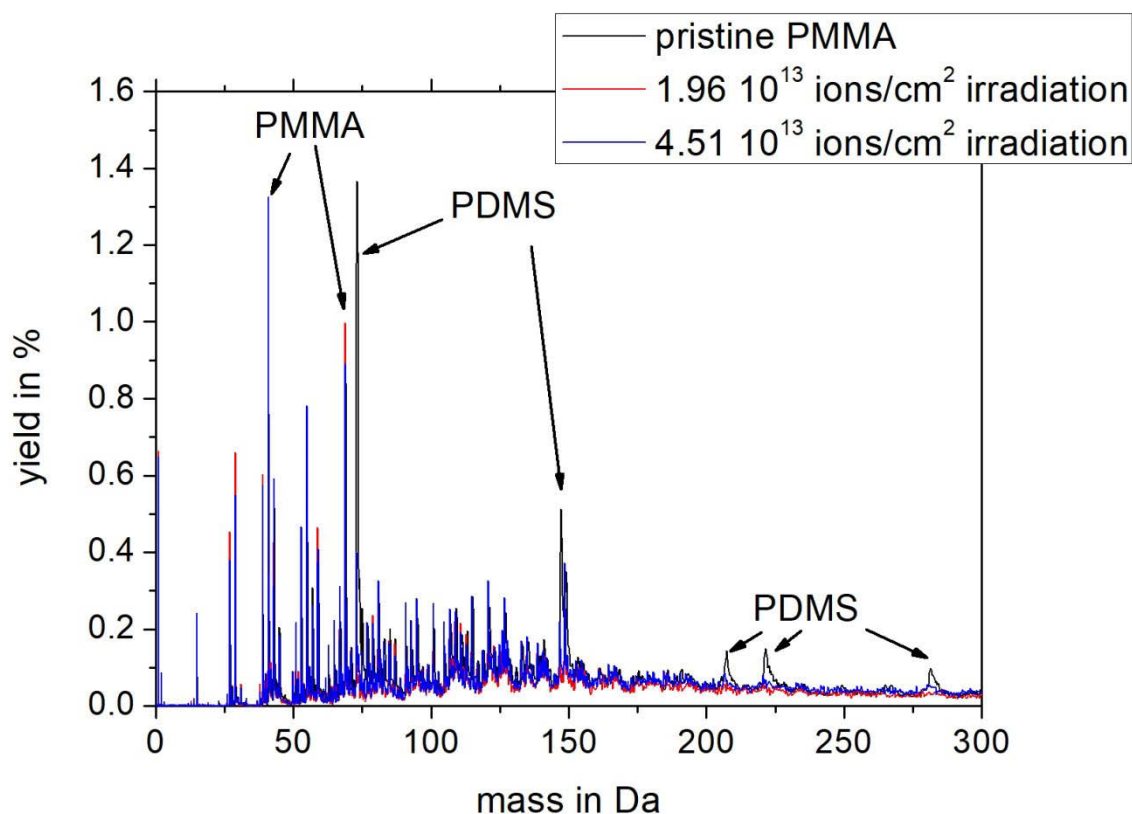


Figure 6-3-2: Yields in % for a pristine PMMA sample with a Polydimethylsiloxane (PDMS) contamination and the same sample after irradiation with 5 MeV Si^{4+} primary ions. The high mass PDMS peaks clearly disappear while the characteristic peaks of PMMA at 41 Da and 69 Da stay and the low mass peaks increase in intensity.

The first most visible result of the measurement shown in Figure 6-3-2 is that the fluence on the sample was enough to clean of a Polydimethylsiloxane (PDMS) contamination. The peaks of the contamination disappear. No completely new peaks, which could be attributed to the cross-linking effect starting, can be detected. It is possible that the secondary ions of new cross-linked molecules already appear in the secondary ion spectrum right from the start of the measurement. This is supported by the fact that the peaks for secondary ions with masses higher than 89 Dalton, the mass of the protonated unit cell of PMMA, appear in the spectrum.

A zoom in around 76 Da for the secondary ion yield in figure 6-3-3 and around 149 Da in figure 6-3-4 completes the picture, as it shows how some peaks even gain intensity after irradiation. Cross-linking can be an effect that explains the increase of yield for these higher mass secondary ions. Another explanation is the removal of the PDMS surface contamination.

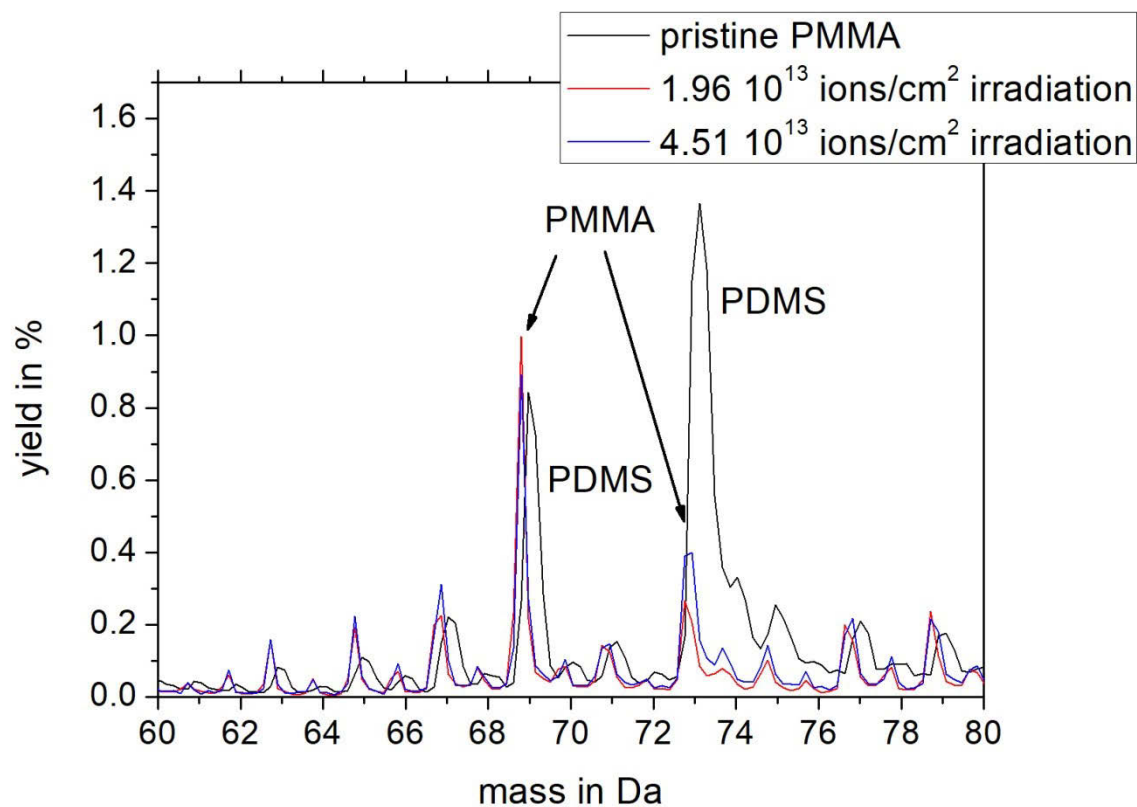


Figure 6-3-3: Yields in % for the same sample as in figure 6-3-2 zoomed in around the 76 Da area. The disappearance of the PDMS contamination is clearly visible, as much as the stable/increasing PMMA yield even though the sample is irradiated.

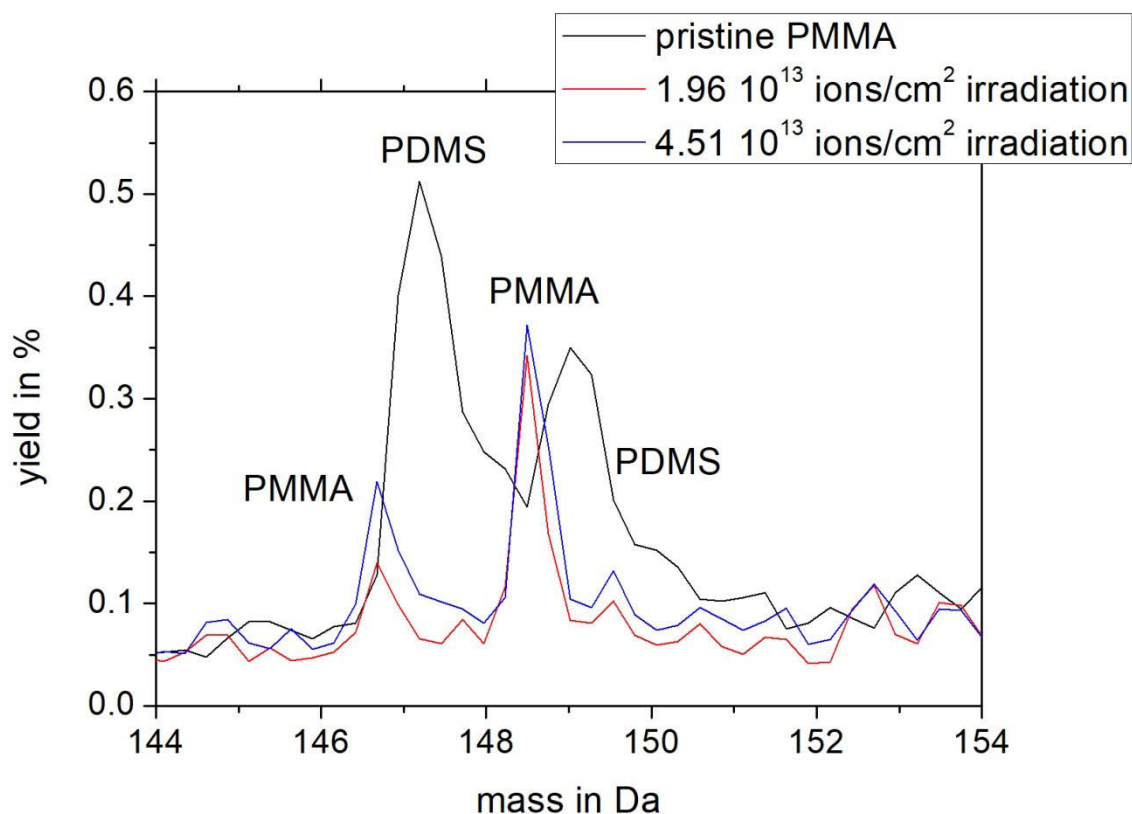


Figure 6-3-4: Yields in % for the same sample as in figure 6-3-2 zoomed in around the 147 Da area. The disappearance of the PDMS contamination is clearly visible, as much as the stable and even increasing PMMA yield even though the sample is irradiated.

Two mechanisms of cross linking proposed by Chapiro et al. [106] have the mass of 226 Da ($C_{12}O_4H_{18}$) and 254 Da ($C_{14}O_4H_{22}$) both consisting of two unit-cells bound at their side chains. This mass peaks are not visible in the spectrum as they are neutral. The most prominent higher mass peak is at 149 Da and can be interpreted as the cross-linked $C_{12}O_4H_{18}$ molecule minus H_2O and one $COOCH_3$ group.

6.4 Application IV Mass spectrum of a PCB board

PCBs are a widely used component in electronics and have to adhere to the RoHS [107] directive. In this context test procedures with good LLD are interesting to investigate for their ability to assure the RoHS standards are met.

For the test a common PCB board piece (as it is used in most electronic components) was taken, in order to test if it is possible to determine the type of PCB used and if any materials of interest can be found. The mass spectrum obtained using an 8 MeV Si^{4+} primary ion beam is shown in figure 6-4-1.

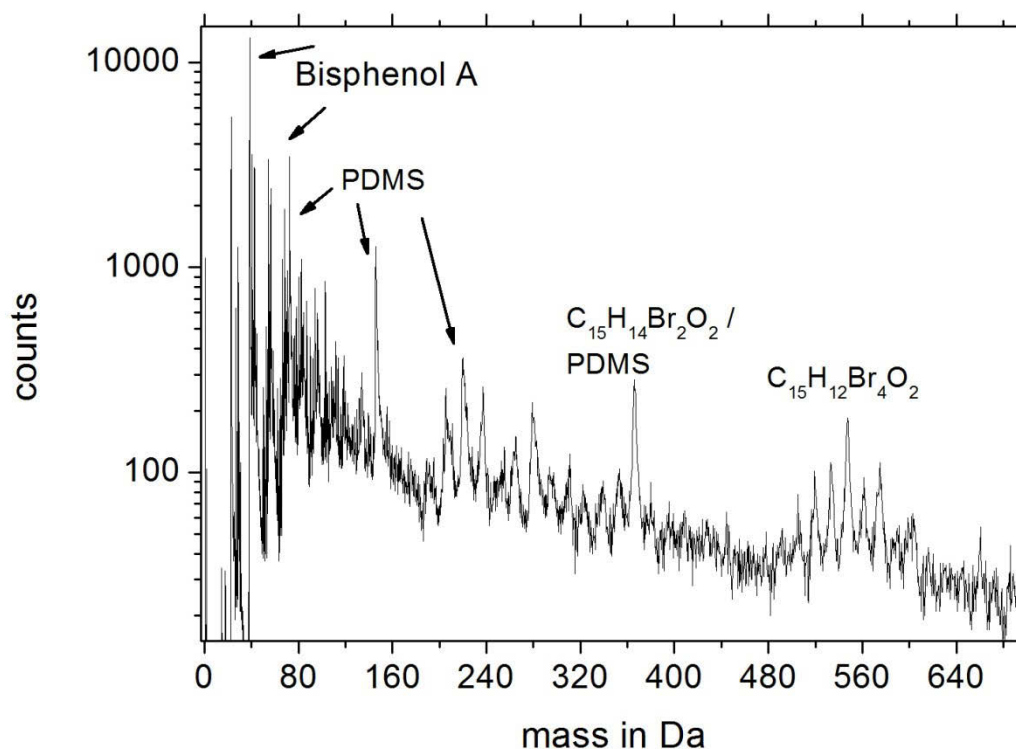


Figure 6-4-1: Mass spectrum of the PCB. Characteristic peaks for Bisphenol A and bromated Bisphenol A molecules which make up the epoxy resin are visible, also a surface contamination with PDMS.

The spectrum shows the characteristic peaks for Bisphenol A (41 Da, 57 Da) the main building block of most epoxy resin used in PCB boards. The Bisphenol A used in these boards is a material which is currently reviewed by the EU and might be regulated more strictly in the future.

The question now is, what kind of bromides were used to make the PCB flame resistant. The peak near 370 Da can be assigned to Dibromobisphenol A but could also be PDMS. Another peak around 544 Da can be assigned to Tetrabromobisphenol A. The mass spectrum shows peaks that fit to a mixture of Bisphenol A types and because commercial PCBs are a mixture of Bisphenol types this can be expected.

No clear lead peak at the expected mass of 207 Da appears in the spectrum. An expected and fortunate result as the PCB is already RoHS compliant regarding the current regulation which prohibits the use of lead.

Another interesting aspect of this mass spectrum is the different calibration as compared to the Leucine standard spectrum used at the same day. In this case it was helpful to have a PDMS contamination which can be recognised by its characteristic peaks for re-calibration of the spectrum.

7 Conclusions and Outlook

During the work on this thesis several ways to improve the MeV SIMS setup's performance have been investigated:

1. Regarding the possibility to perform ambient pressure and heavy ion MeV SIMS applications, thick-walled glass capillaries were tested and found to be sturdy and easy to handle while also showing good characteristics for PIXE measurements running along with the mass spectrometry.

Compared to a thin walled glass capillary the PIXE-background from the capillary wall material disappears completely. While further work to decrease the exit diameter, which was 30 μm for the capillary tested, is necessary, the capillaries can and have been already used for heavy ion SIMS, using ions that cannot be focused with conventional magnetic quadrupole lens systems due to the ion beam's high rigidity. Tests of newly produced thick wall capillaries with potentially smaller exit diameters are under way at Chiang Mai University.

2. The establishment of a reliable method to measure the secondary ion yield using a Si-PiN diode that periodically intercepts the beam, brought insight into yet unknown experimental parameter dependencies of the secondary ion yield:

First the secondary ion yield depends considerably on the angle between the analyte surface and the secondary ion extractor. An angle difference of 3° leads to a drop of 90 % in the secondary ion yield. This manifest itself further in a scan size and distance dependence of the yield. While the collection efficiency of the secondary ion extractor generally decreases with its distance to the sample a large scan size coupled with the angle dependence leads to a more complicated behaviour. The ideal position of the extractor to maximise the yield depends on the secondary ion as well as the scan size.

Additionally, the angle dependence of the yield leads to an inhomogeneous collection efficiency over the scan size. This information is important in order to interpret an MeV SIMS mapping correctly. It is especially important, because the angular dependence is not the same for different secondary ions. Ions with heavier mass tend to be collected at a higher rate with a lower angle between the primary ion beam and the extractor compared to light mass secondary ions, supporting a Coulomb-explosion based model as description of the secondary ion desorption process.

To sum it up, a newly designed MeV SIMS setup will benefit from a sample holder which has the option to change the angle between sample and extractor in two planes and a changeable distance between extractor and surface.

3. Apart from the setup parameters, the influence of the primary ion on the secondary ion yield was investigated as well. A second order dependence of the yield on the stopping force was observed, supporting a thermal spike model for the secondary ion desorption. Combined with the angle dependence of the secondary ion yield these results support the combined coulomb explosion and thermal spike model by E.M. Bringa and R. E. Johnson [39]. Still, a high variance in the yield measurements has been registered due to the strong dependence of the secondary ion yield on the aforementioned setup parameters as well as on the surface characteristics of the sample.
4. Another important aspect investigated is the static / dynamic SIMS region. It is important to determine the border between static and dynamic SIMS for MeV SIMS, which is defined as the primary ion fluency that is necessary to observe a change in secondary ion yield of at least 10 %. The values determined for keV SIMS, which itself has a large variation of static limits according to the literature [89, 90], cannot just be extrapolated.

In comparison to keV SIMS a much lower fluence limit for static MeV SIMS was observed, well below 10^{11} ions/cm². Therefore, before any measurement, the static limit should be checked for a given sample. Alternatively, one can choose to stay well below 10^{10} ions/cm², to be relatively safe under the static limit although the safest method is always an experimental determination of the static limit.

Further measurement in the dynamic MeV SIMS regime shed light into the processes happening during MeV ion bombardment. The breaking and rearrangement of bonds can be seen in the yield dependence on the primary ion fluence. It was shown that dynamic (multilayer) MeV SIMS, and in the case of the experiments on PMMA, the removal of a PDMS contamination layer, is possible.

5. The possibility of quantitative MeV SIMS has been tested by measuring samples of simple mixed monolayers. The results show that quantitative MeV SIMS, in its most simple form based on the use of standards, can be performed.
6. After all the basic tests had been performed, several applications including analysis of cultural heritage, forensics and material science applications were tried out. The

technique is able to solve a forensics question regarding which ink was applied last on a crossing of two ink lines, it is able to identify the type of material used in a PCB and hint to the varnish used for an orthodox church icon. Further on information about the molecules produced after MeV ion irradiation of PMMA was gained.

To sum it up, quite a few new aspects of MeV SIMS have been discovered, leaving room for considerable future development of the technique. The characterisation of the setup and the influence of the setup parameters and primary ion fluence on the yield can be used to establish well defined yield measurement settings, which will produce more reproducible and comparable results. The next step from here will then be quantitative MeV SIMS, greatly increasing the value of the technique.

The establishment of the possibility of dynamic MeV SIMS further widens the field of applications. Materials that are well suited can be found and the process of reorganisation of molecular bonds after ion bombardment can be investigated as well.

In conclusion it is evident that there is still a lot more room for the development of MeV SIMS.

Appendix A MeV SIMS spectra compilation

As MeV SIMS is a new technique compared to keV-SIMS the database for example Spectra is small. For the peak identification, especially for high masses, the keV-SIMS spectra as they can be found for example in the static SIMS library [108], are not always sufficient. To increase the available information on MeV SIMS spectra this appendix shows several spectra obtained during the work on this thesis.

The following MeV SIMS spectra have been recorded using 8 MeV Si^{4+} primary ions:

- Glycine
- Leucine
- Arginine
- Irganox 1010
- Polymethylmethacrylate
- Polystyrene
- Cholesterol
- PV 19 red pigment
- Phthalocyanine blue PB 15

The samples were produced as described in chapter 5. In some cases, no primary ion intensity measurement was performed and for these spectra only counts are plotted on the y axis. What will become clear, especially in the comparison to keV-SIMS is the appearance of high mass secondary ions and their higher absolute yield as well as relative intensity compared to fragments for MeV SIMS.

A.1 Glycine

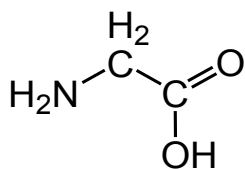


Figure A-1-1: Structure of Glycine which is the simplest amino acid. Two carbon atoms make up the backbone of the molecule. One holding the ammoniac and one connected to the acidic (carboxyl) group.

Glycine ($\text{C}_2\text{H}_5\text{NO}_2$, mass 75 Da, chemical structure in figure A-1-1) is one of the simplest amino acids with many important functions. Fortunately, it can be synthesized in the human body making it a non-essential amino acid. Its main use in industry is as food supplement for example as sweetener or taste enhancer. Pure Glycine forms crystals through bonds between

the NH_3^+ and the COO^- group of the molecule which is also the form it is present in the sample analysed. The spectrum obtained from it is shown in figure A-1-2.

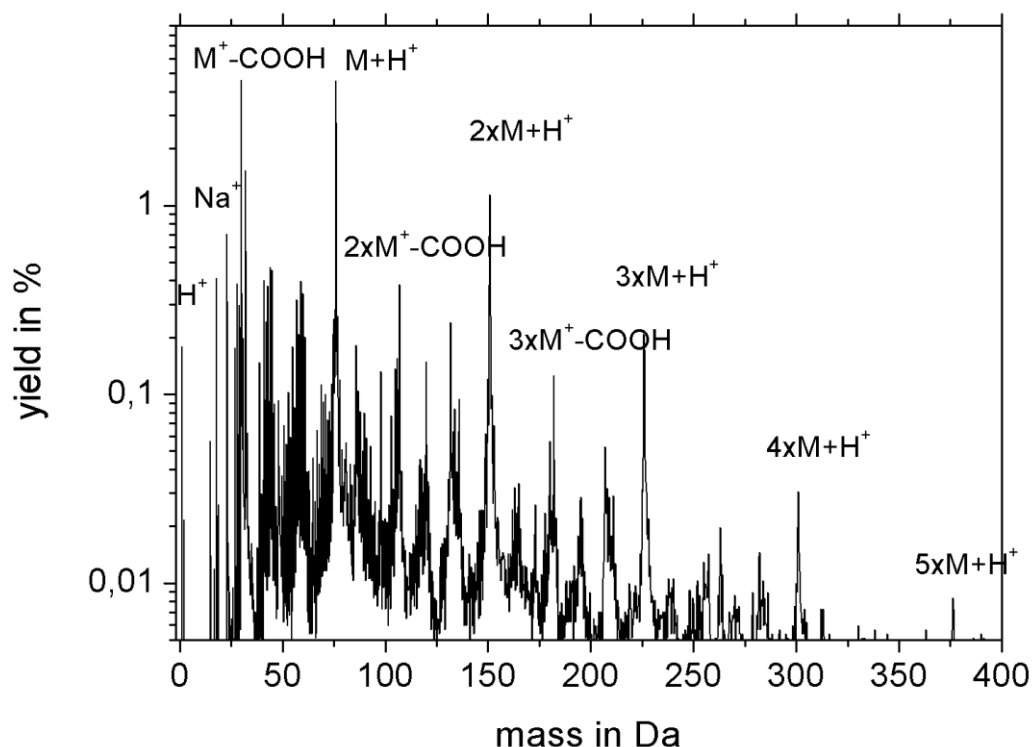


Figure A-1-2: Glycine spectra taken with an 8 MeV Si^{4+} beam. Most important peaks noted are the protonated molecular peaks of Glycine ($\text{M}+\text{H}^+$) and the fragment peak of Glycine minus the COOH (carboxyl) group.

A comparison of the relative intensity of the different peaks from GC-MS [109] to the relative intensities from MeV SIMS (figure A-1-2) can be seen in table A-1-1.

Mass	Relative intensity GC-MS	Relative intensity MeV SIMS
30 ($\text{C}_2\text{H}_2\text{NH}_2$)	100	100
45 (COOH)	11	10
59 ($\text{C}_2\text{H}_5\text{NO}$)	0,1	8,6
75/76(Glycine protonated)	3	99
2xGlycine	N/A	25
3xGlycine	N/A	4,3

Table A-1-1: Relative intensities compared to the main peak at 30 Dalton for a GC-MS mass spectrum and an MeV SIMS spectrum.

On the low mass fragment side, the relative intensity is almost the same. The huge difference between the relative intensities for both techniques appears for higher mass secondary ions and especially intact Glycine molecules. Additionally, the Glycine-Glycine and Glycine-Glycine-

Glycine molecules are only visible using MeV SIMS with relative intensities higher than the molecular peak of Glycine in the GC mass spectrum.

A.2 Leucine

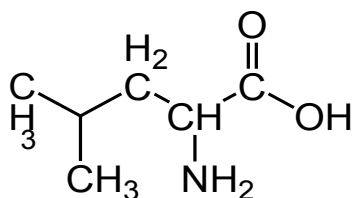


Figure A-2-1: Structural formula of Leucine

Leucine (C₆H₁₃NO₂, mass 131 Da, chemical structure in figure A-2-1) is an essential amino acid. Unlike Glycine, it cannot be produced by the human body and has to be taken in with food. Fortunately, it can be found in all kinds of food, with especially high concentrations in protein rich foodstuff like Soy, beef or peanuts [110].

Its function in the human body is mainly the building and maintaining of muscle tissue which makes it a popular additive in food supplements for muscle formation.

Figure A-2-2 shows a spectrum obtained from Leucine evaporated on a silicon wafer. Visible are molecules made up of up to seven Leucine molecules together.

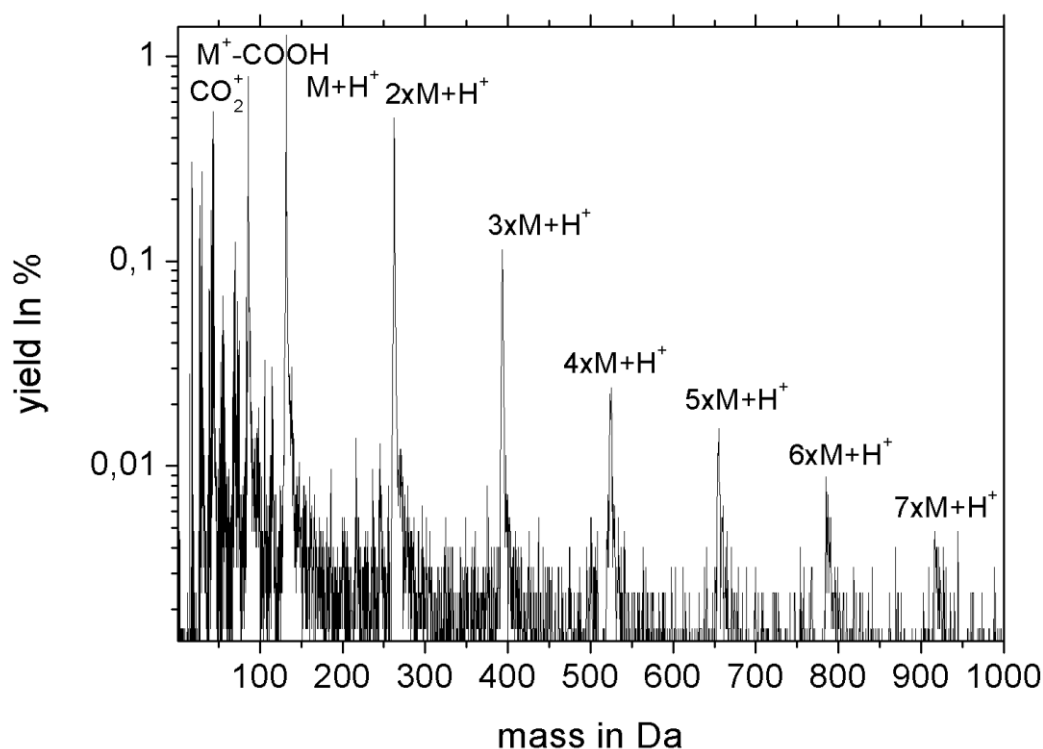


Figure A-2-2: MeV SIMS spectrum of Leucine using 8 MeV Si^{4+} primary ions. Up to seven Leucine molecules are ejected together as molecular ions. With yields of up to 1,3 % for the single-molecular ion of Leucine.

A.3 Arginine

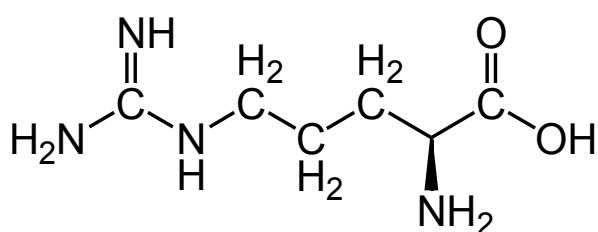


Figure A-3-1: Structural formula of Arginine ($\text{C}_6\text{H}_{14}\text{N}_4\text{O}_2$, mass 175 Da)

Arginine ($\text{C}_6\text{H}_{14}\text{N}_4\text{O}_2$, mass 175 Da) is a semi-essential amino acid. It can be synthesised by the human body but isn't produced sufficiently in most cases, so some must be consumed through nutrition. Its role is mostly in the healing processes of tissue and bone. In contrast to Leucine and Glycine it has four amino groups.

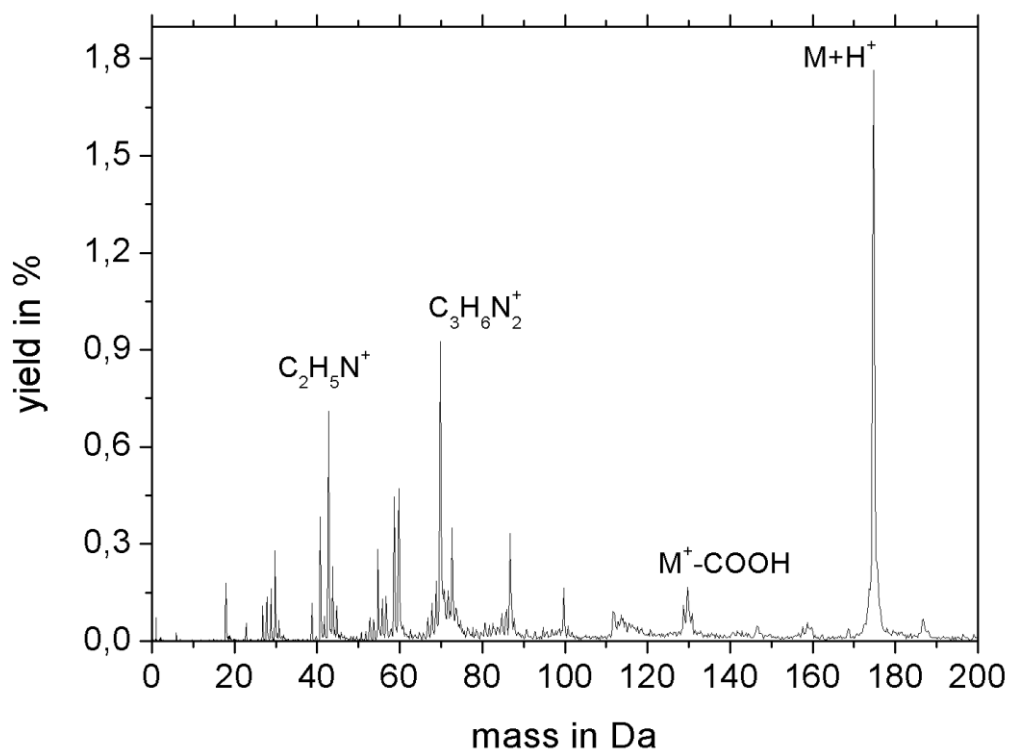


Figure A-3-2: MeV SIMS spectrum of Arginine using 8 MeV Si^{4+} in contrast to the other spectra there are no poly-Arginine peaks visible.

A.4 Irganox 1010

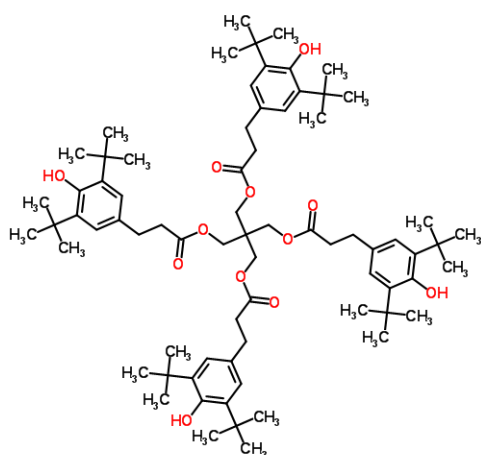


Figure A-4-1: Structural formula of Irganox 1010, the molecule has four branches around a centre carbon atom. The four branches are visible as fragments in the mass spectrum.

Irganox 1010 ($C_{73}H_{108}O_{12}$, mass 1176 Da) is an antioxidant used to stabilise organics like oil, adhesives or plastics like the polyethylene used for plastic bottles. In Figure A-4-2 a keV-SIMS spectrum is shown and in figure A-4-3 an MeV SIMS spectrum obtained using 8 MeV Si^{4+} primary ions.

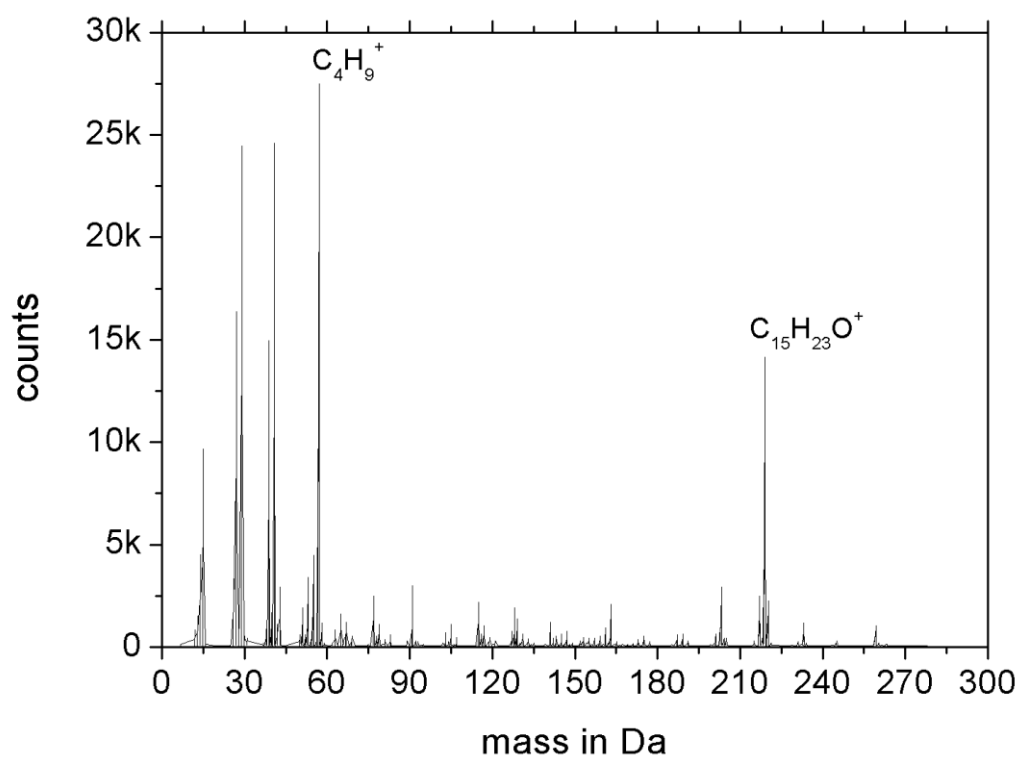


Figure A-4-2: KeV-SIMS spectrum of Irganox 1010 using 8 keV Cs^+ primary ions [108]. Most prominent are the broken of chains of carbohydrates at 221 Da. The full 1178 Da peak is not visible.

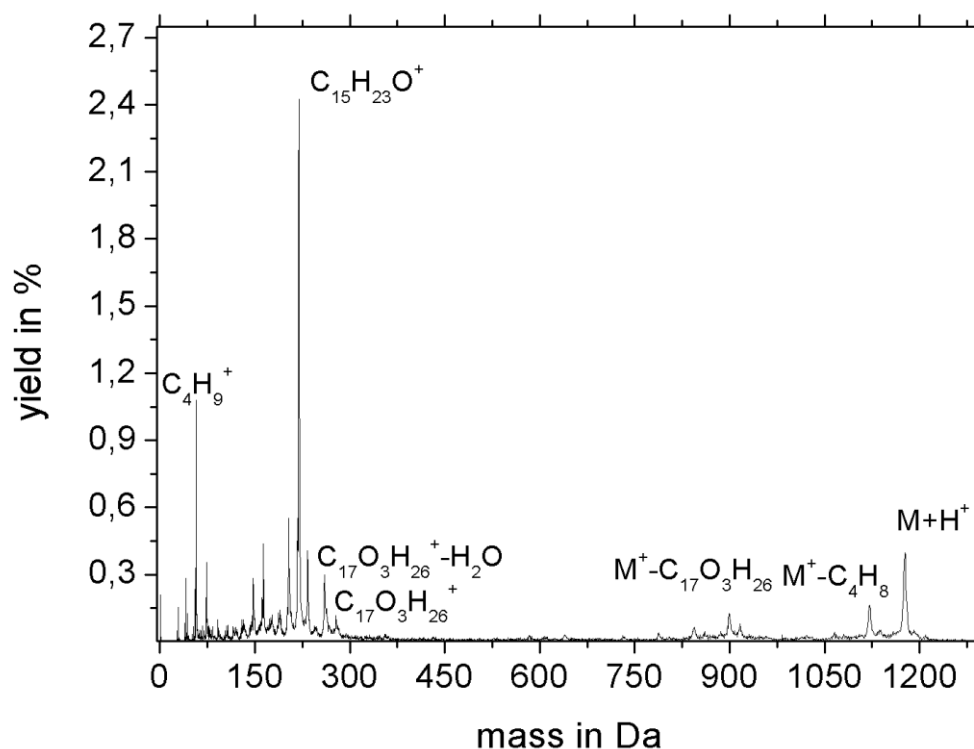


Figure A-4-3: MeV SIMS spectrum of Irganox 1010 using 8 MeV Si^{4+} . Here the molecular peak is visible. Also, visible, the molecule minus one of the C_4H_8 groups and minus one of the complete $\text{C}_{17}\text{H}_{26}\text{O}_3$ groups.

A.5 Polymethylmethacrylate

Polymethylmethacrylate (PMMA, $(\text{C}_5\text{O}_2\text{H}_8)_n$) is also known as PLEXIGLAS or acrylic glass. It is used as glass substitute in all kinds of windows and eyeglass lenses.

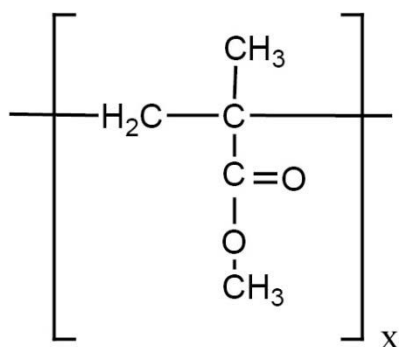


Figure A-5-1: Structural formula of PMMA repeat cell

Due to the low intensity of the signal of PMMA and contamination of the sample with Polydimethylsiloxane (PDMS) which is a common contaminant for SIMS and ingredient of

many plastic compounds, there are only higher mass peaks of PDMS in the spectrum. The PMMA peaks appear in the low mass section. Figure A-5-2 shows the keV-SIMS spectrum for PMMA and PDMS and figure A-5-3 shows the MeV SIMS spectrum of a PDMS contaminated PMMA sample.

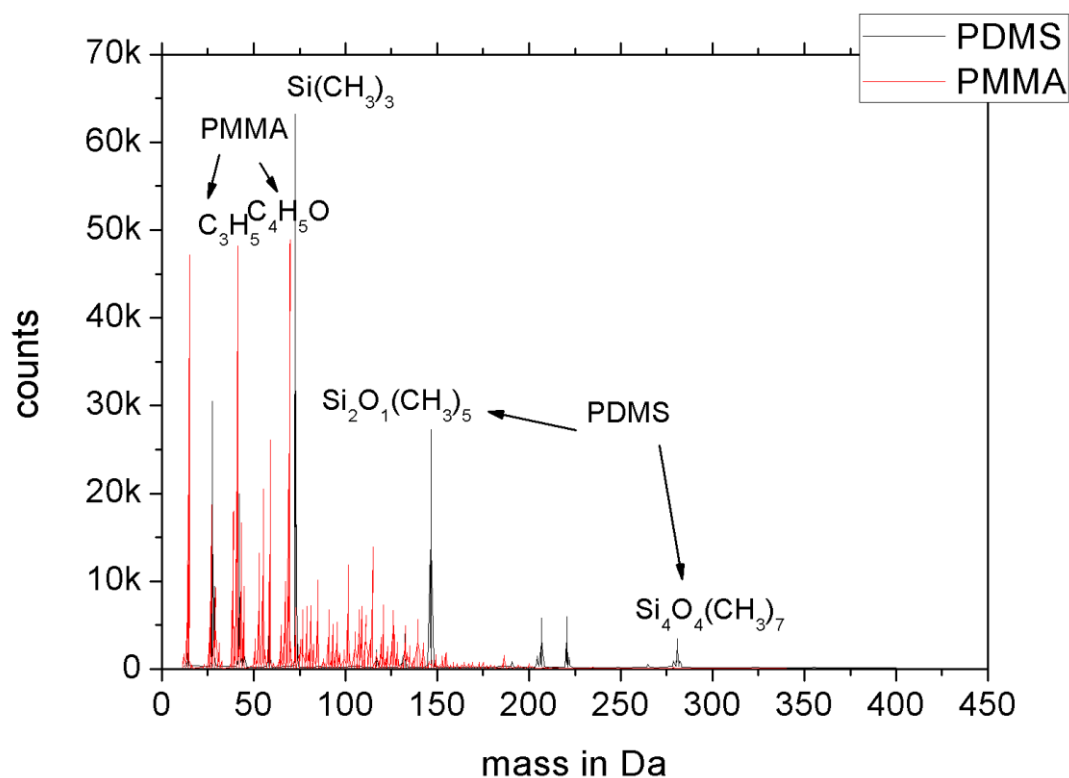


Figure A-5-2: KeV SIMS spectrum of PMMA and PDMS taken with Cs^+ keV primary ions. The high mass part is not shown as no peaks were present above 300 Da. [108]

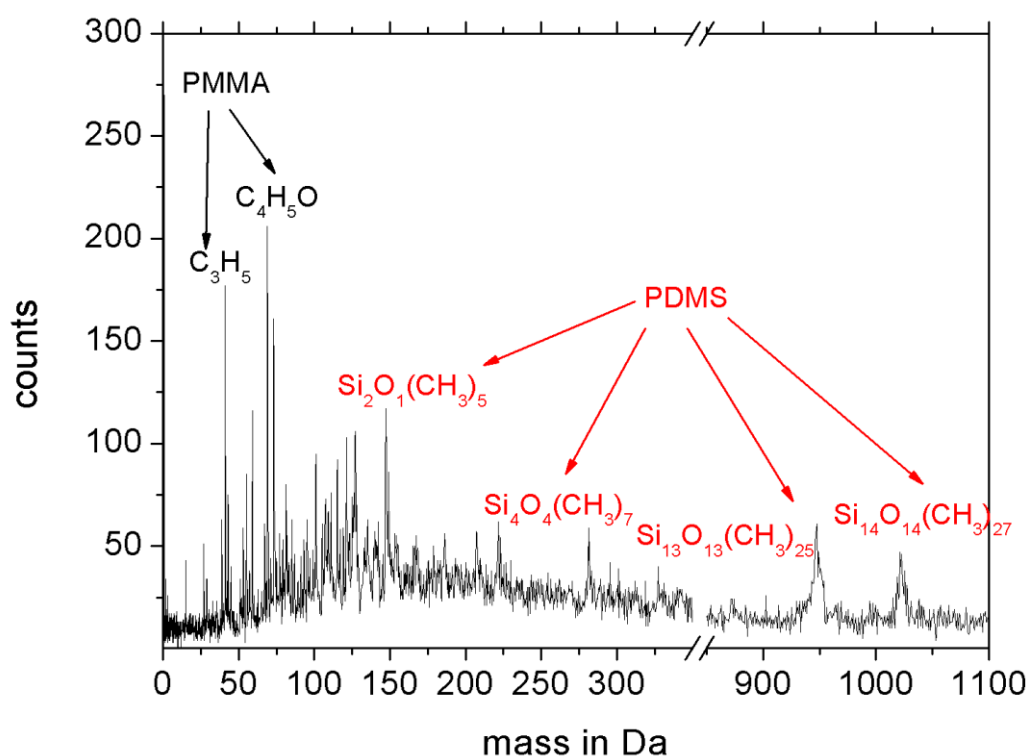


Figure A-5-3: MeV SIMS of the contaminated PMMA sample. for the higher masses it only shows the PDMS peaks.

The most interesting part is the appearance of high mass peaks of the PDMS contamination visible in the mass spectrum. These peaks cannot be found in the keV-SIMS spectrum of PDMS.

A.6 Polystyrene

Polystyrene (PS, $(C_8H_8)_n$) is most commonly known for its role in the packaging industry and is one of the most produced plastics worldwide. Its low to non-existent biodegradability makes it a significant pollution factor. Figure A-6-1 shows the unit cell of the Polymer.

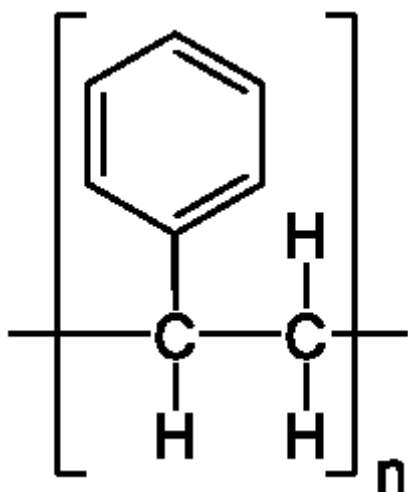


Figure A-6-1: Structural formula of PS repeat cell, note the aromatic ring.

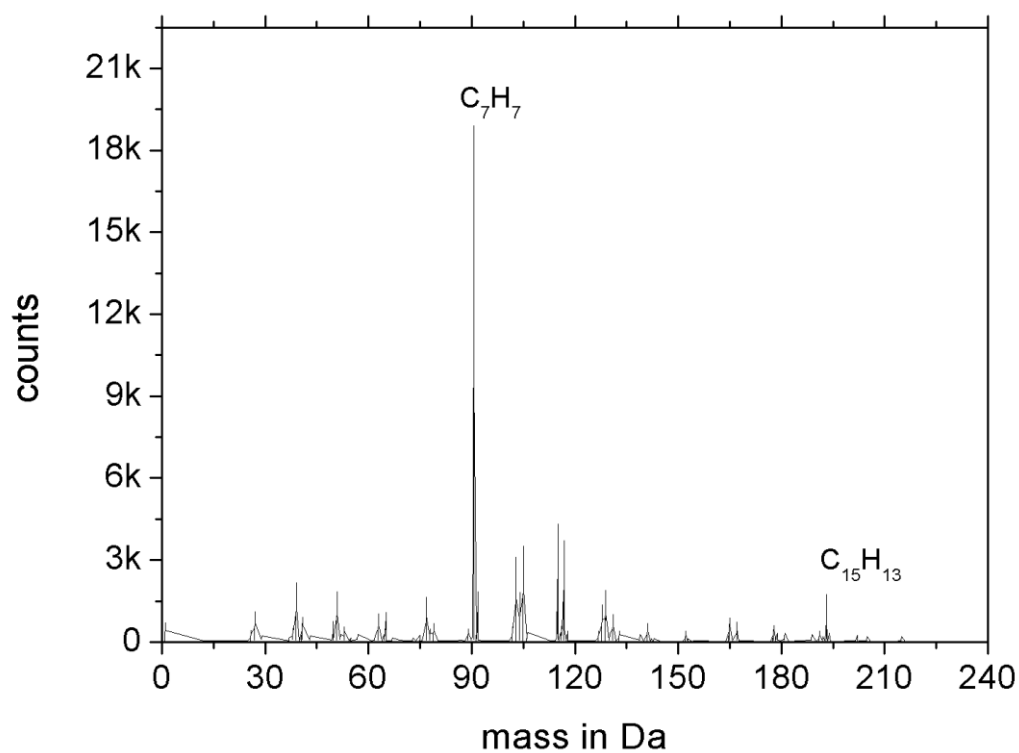


Figure A-6-2: KeV SIMS spectrum of polystyrene taken with a Cs^+ primary ion beam [108]. The main peaks are the C_7H_7 and with about 10 % of its intensity the $\text{C}_{15}\text{H}_{13}$ peak.

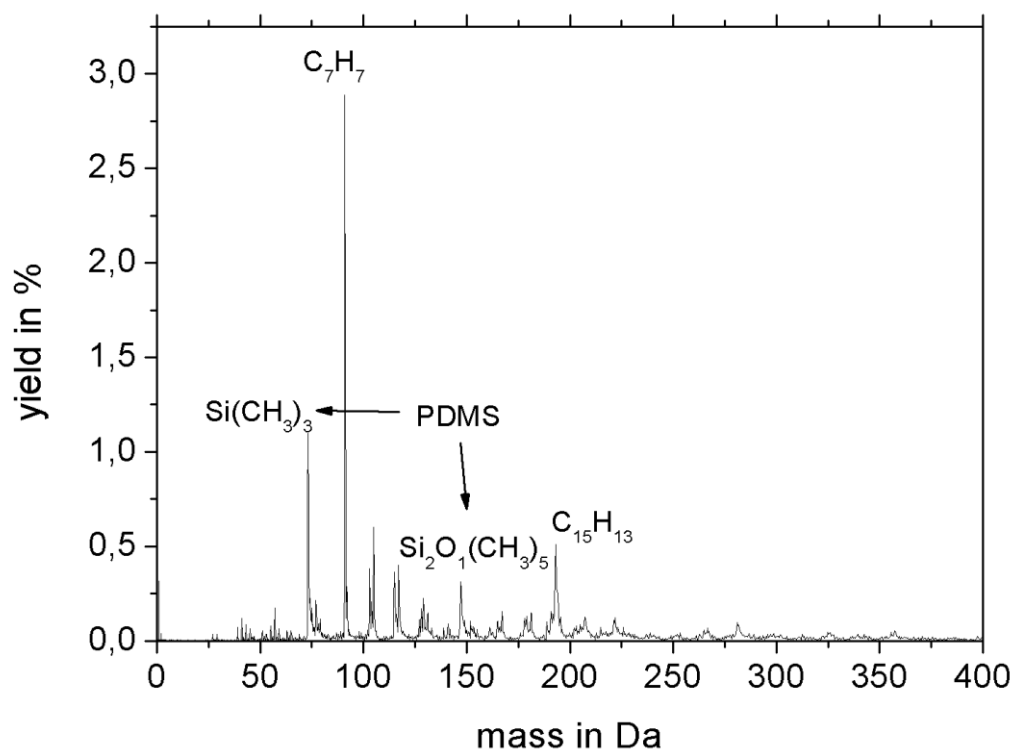


Figure A-6-3: MeV SIMS spectrum of Polystyrene. Again, some PDMS contamination is visible. This shows how good a PDMS detection device MeV SIMS is.

Again, the spectrum shows a PDMS contamination problem even though the yield of polystyrene is high with about 3 % absolute secondary ion yield for the characteristic C_7H_7 peak. The relative intensity of the $C_{15}H_{13}$ peak compared to the C_7H_7 peak is about 20 %, which is two times the value obtained for keV-SIMS.

A.7 Cholesterol

Cholesterol is another biomolecule, belonging to the lipid group ($C_{27}H_{46}O$, mass 386.65 Da). It can be found in the cell walls of animals including humans. Figure A-7-1 shows the structure of Cholesterol.

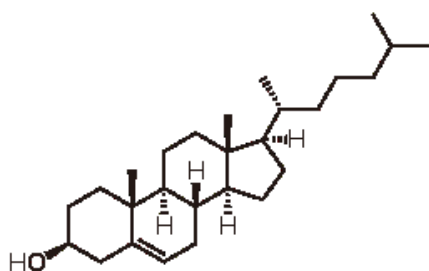


Figure A-7-1: Structural formula of Cholesterol.

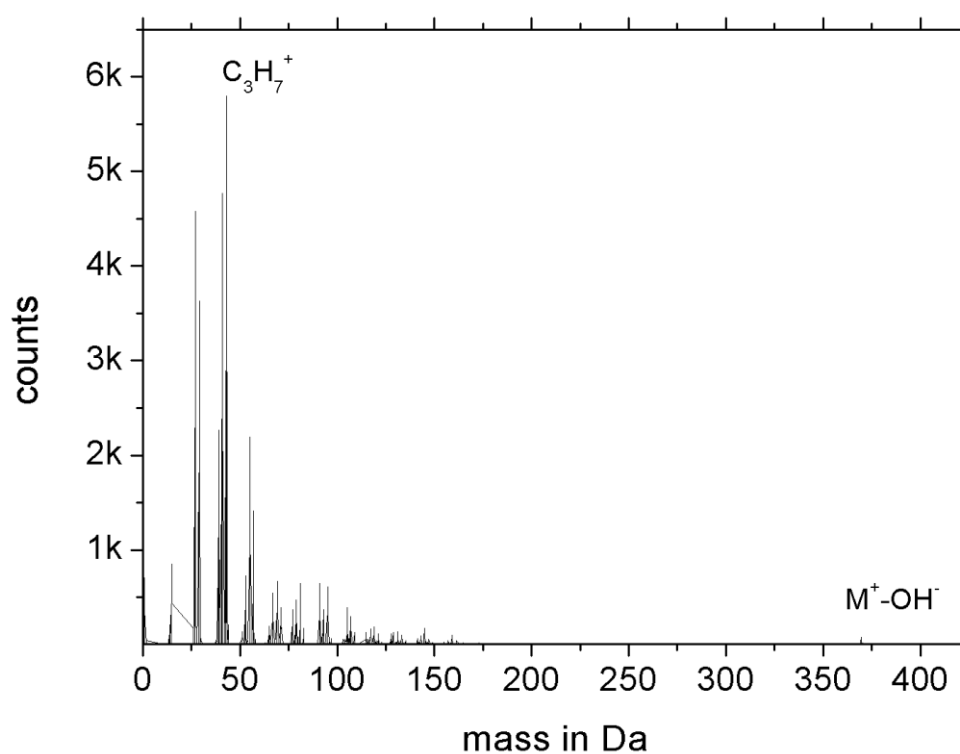


Figure A-7-2: The keV Sims spectrum taken with Ga^+ primary ions. The main peak is at 43 Da with periodic repeating groups at 12 Da steps. The molecular peak is barely visible.

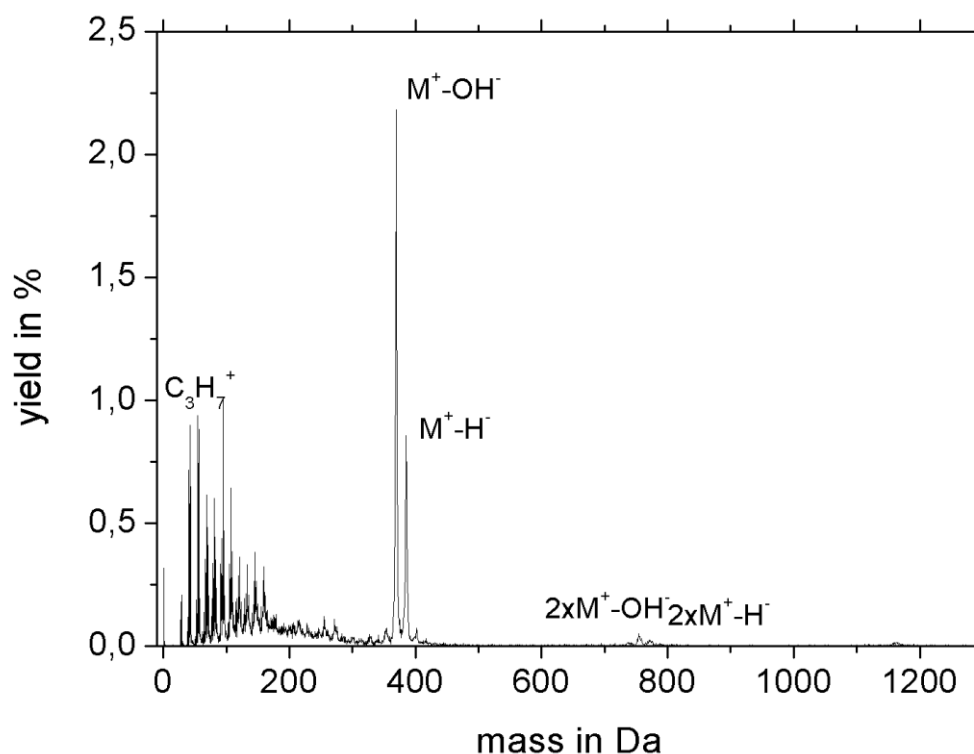


Figure A-7-3: MeV SIMS spectrum taken with 8 MeV Si^{4+} . The barely visible molecular peak from the keV-SIMS spectrum turns into the dominant peak. Also, a di-cholesterol peak group can be seen.

A.8 Quinacridone rosé PV 19

Quinacridone ($\text{C}_{20}\text{H}_{12}\text{N}_2\text{O}_2$, PV19, mass: 312 Da) is an important pigment in a number of manufacturers paints, mostly as a single pigment, but also in quite a few mixtures. This is an interesting pigment which is available in two major versions, Rose and Violet, but things become complicated in that there is also a “red” form not far removed from the Rose, all covered by the same PV19 designation.

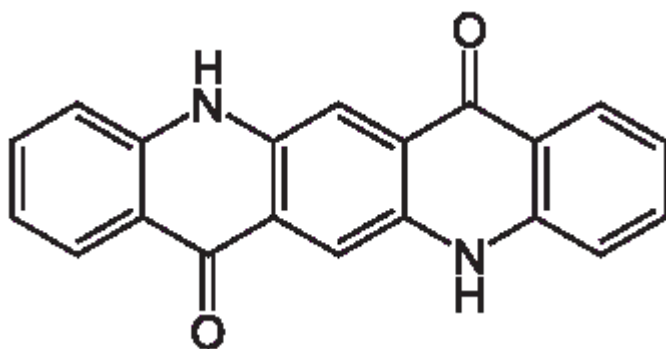


Figure A-8-1: Quinacridone molecule

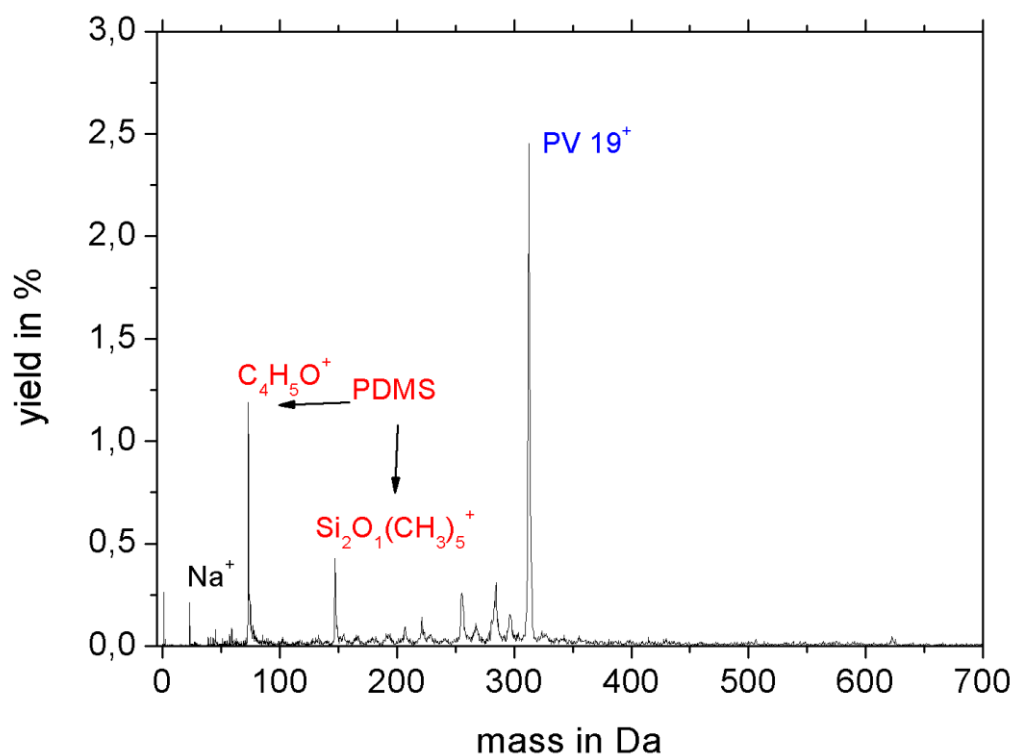


Figure A-8-2: Mass spectrum of Quinacridone using 8 MeV Si^{4+} primary ions also showing a PDMS contamination.

A.9 Phthalocyanine blue PB 15

Phthalocyanine blue (PB 15, $\text{C}_{32}\text{H}_{16}\text{CuN}_8$, mass: 576 Da) is a pigment based on phthalocyanine with a copper atom in the centre. The molecular structure is shown in figure A-9-1 and the MeV SIMS spectrum obtained from the pigment is shown in figure A-9-2. Additionally, to the pigment there is often found PDMS contamination in the spectrum.

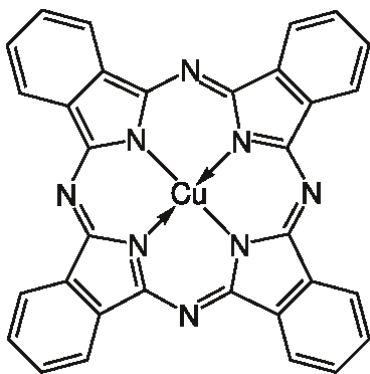


Figure A-9-1: Phthalocyanine blue molecule with the copper atom in its centre.

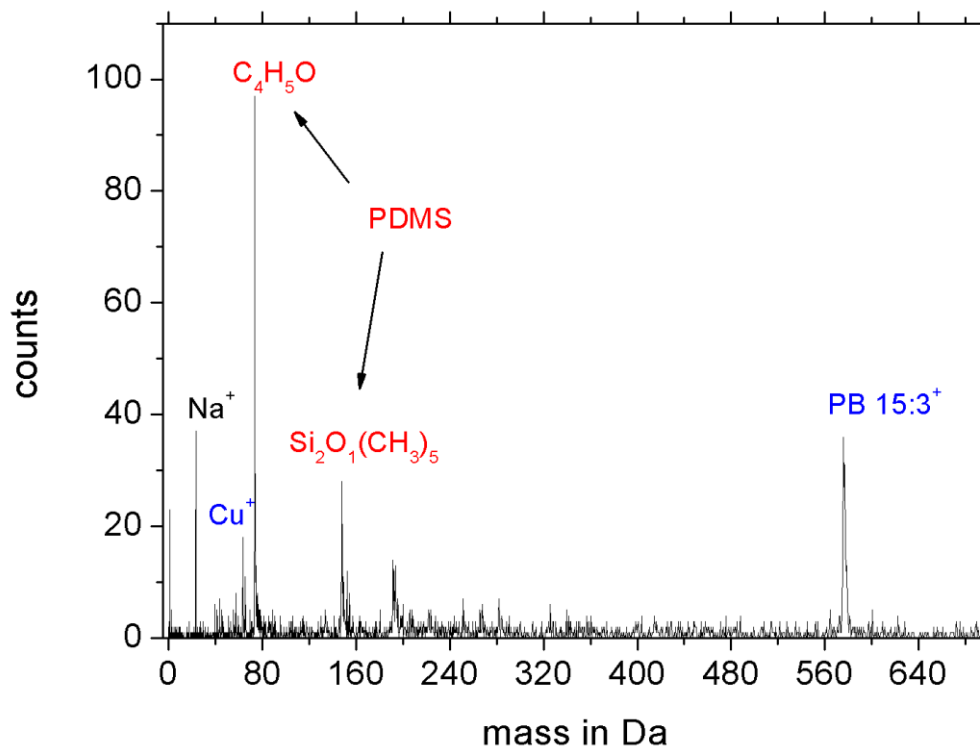


Figure A-9-2: Phthalocyanine blue MeV SIMS spectrum showing a PDMS contamination, the copper peak at 63.5 Da and the Phthalocyanine blue peak at 576 Da.

Appendix B Sample thickness influence

During a visit to the KU Leuven the topic of the thickness influencing the secondary ion yield on a keV-SIMS measurement came up. Previous studies by Bolbach et al. [97] showed a yield maximum for keV-SIMS at two monolayers or 5 nm and at 20 nm for PDMS. This also had to be tested for an MeV SIMS experiment.

Three samples of Glycine with thicknesses of 300 ± 20 nm, 200 ± 20 nm and 100 ± 20 nm produced in the RBI evaporator were tested for their secondary ion yield. The scan area was $100 \mu\text{m} \times 100 \mu\text{m}$ and the primary ion was 8 MeV Si^{4+} .

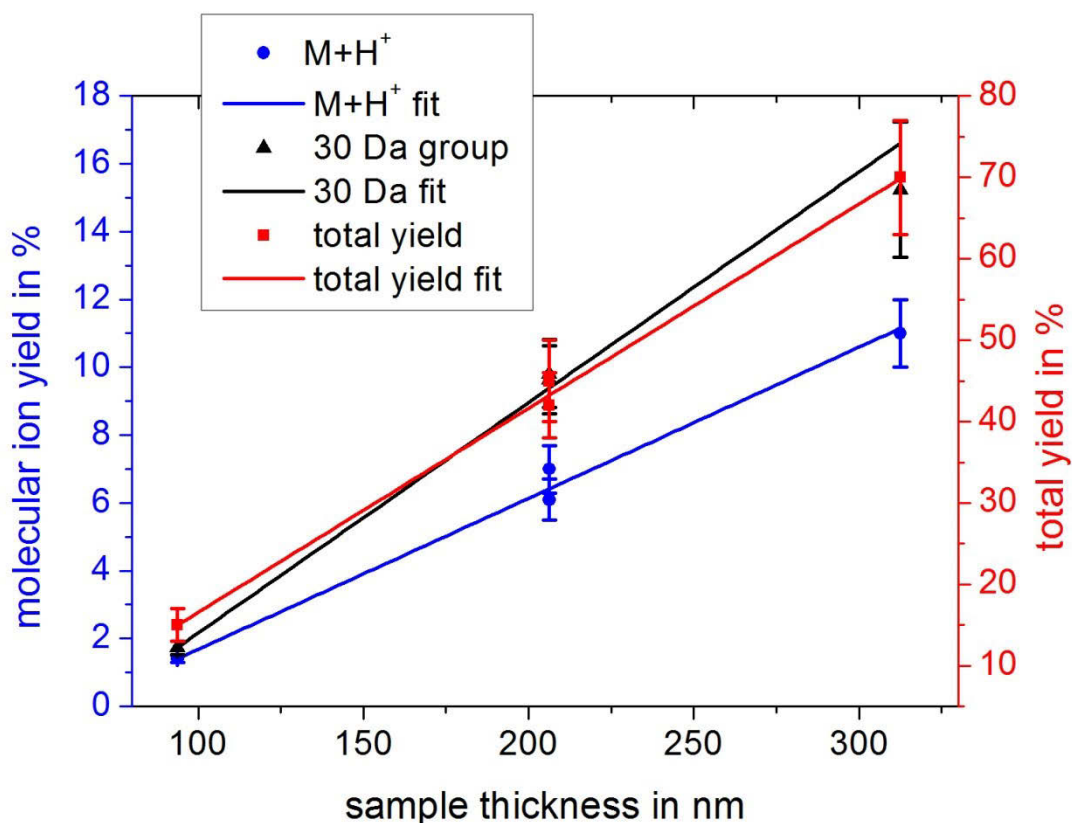


Figure B-1: Thickness-yield dependence - in blue the Glycine molecular ion signal, in black the 30 Da fragment peak yield and in red the total ion yield.

The first assumption was the reduced yield might stem from an incomplete coverage of the wafer during evaporation. The ratio between the thicknesses t compared to the ratio between the yields Y being $\frac{t_1}{t_2} \neq \frac{Y_1}{Y_2}$ and the fact that the yield on two different points for the thickness 200 nm is the same for two different points support the interpretation that the coverage of the wafer is continuous, and the yield decrease stems from the decreasing layer thickness.

This coincides with earlier measurements for other MS techniques [97] even though the thickness in these experiments was ten times lower. A possible explanation for this large discrepancy is the scaling of the thickness measurement in the RBI evaporator done by a quartz crystal microbalance, which might use the wrong calibration.

If the calibration was correct it shows that the MeV SIMS desorption process is influenced by energy deposition even 200 nm below the surface. At the least the results show that there is a dependence of the secondary ion yield on the surface density of the material which is a prerequisite for quantitative analysis.

Bibliography

- [1] B. Jones, "The Development of MeV Secondary Ion Mass Spectrometry," *PhD Thesis*, pp. 52-54, 2012.
- [2] A. S. H. O. A. I. N. Imanishi, "Electronic Sputtering from a SiO₂ Target Bombarded by Heavy Ions," *AIP Conf. Proc.* 475, p. 396, 1999.
- [3] P. Hakansson, A. Johansson, I. Kamensky, B. Sundqvist, J. Fohlman, P. Peterson, "Fast heavy-ion induced desorption of biomolecules," *ieee transactions on nuclear science*, p. 1776–1778, 1981.
- [4] D. Harker, "X-RAY SPECTROMETER". USA Patent US 2540821 A, 6 february 1951.
- [5] Y.Q. Wang, M. Nastasi, "Handbook of Modern Ion Beam Materials Analysis," 2009.
- [6] E. D. L. A. P. B. J. D. H. Thomas R. Covey, "Liquid chromatography/mass spectrometry," *analytical chemistry*, p. 1451A–1461A, 1986.
- [7] D. Henneberg, "Eine Kombination von Gaschromatograph und Massenspektrometer zur Analyse organischer Stoffgemische," *D. Z. Anal. Chem.* , pp. 12-23, 1961.
- [8] Z. T. J. M. W. B. G. R. Graham Cooks, "Mass Spectrometry Sampling Under Ambient Conditions with Desorption Electrospray Ionization," *science volume 306, Issue 5695*, pp. 471-473, october 2004.
- [9] W. Z. M. S. H. M. Uwe Pies, "Matrix-assisted laser desorption ionization time-of-flight mass spectrometry: a powerful tool for the mass and sequence analysis of natural and modified oligonucleotides," *Nucleic Acids Res*, pp. 3191-3196, august 1993.
- [10] P. F. D. J. L. J. Allison C. Aiken, "Elemental Analysis of Organic Species with Electron Ionization High-Resolution Mass Spectrometry," *analytical chemistry*, p. 8350–8358, 2007.
- [11] D. T. R.D. Macfarlane, "Californium-252 plasma desorption mass spectroscopy," *Science*, pp. Vol. 191, Issue 4230, pp. 920-925, march 1976.
- [12] F. H. Y. F. J. R. G.M. Lancaster, "Secondary ion mass spectrometry of molecular solids. Cluster formation during ion bombardment of frozen water, benzene, and cyclohexane," *Journal of the American Chemical Society*, pp. 1951-1958., 1979.
- [13] G. J. v. B. Vilmos Kertesz, "Improved imaging resolution in desorption electrospray ionization mass spectrometry," *Rapid Commun. Mass Spectrom.*, p. 2639–2644, 2008.

- [14] J. M. W. a. R. G. C. Zoltan Takats, "Ambient mass spectrometry using desorption electrospray ionization (DESI): instrumentation, mechanisms and applications in forensics, chemistry," *Mass Spectrom.*, p. 1261–1275, 2005.
- [15] B. Hagenhoff, "High Resolution Surface Analysis by TOF-SIMS," *Mikrochim Acta*, p. 259–271, 2005.
- [16] Z. S. N. O. P. P. V. Z. R. Luka Jeromel, "Development of mass spectrometry by high energy focused heavy ion beam: MeV SIMS with 8 MeV Cl⁷⁺ beam," *Nuclear Instruments and Methods in Physics Research B*, p. 22–27, August 2014.
- [17] Y. Nakata, *Fundamental Studies and Development of a Molecular Imaging Technique by Mass Spectrometry Using MeV Heavy Ion Beams*, 2009.
- [18] M. D. M. M. A. G. M. S. H.-A. Schulte-Borchers, "Time-of-flight MeV-SIMS with beam induced secondary electron trigger," *Nuclear Instruments and Methods in Physics Research Section B: Beam Interactions with Materials and Atoms*, pp. 94-98, 2016.
- [19] I. B. R. Z. S. D. D. C. N. S. T. Tadic, "Development of a TOF SIMS setup at the Zagreb heavy ion microbeam facility," *Nuclear Instruments and Methods in Physics Research B*, vol. 332, pp. 234-237, 2014. , pp. vol. 332, pp. 234-237 , 2014.
- [20] I. B. R. M. J. M. P. H. a. M. H. Zdravko Siketic, "Submicron mass spectrometry imaging of single cells by combined use of mega electron volt time-of-flight secondary ion mass spectrometry and scanning transmission ion microscopy," *Applied Physics Letters*, pp. 093702-1 - 093702-4, 2015.
- [21] L. Matjacic, *Optimisation and application of AP MeV SIMS*, University of Surrey, 2018.
- [22] M. K. M. F. T. A. J. Toshio Seki, "Ambient analysis of liquid materials with Wet-SIMS," *Nuclear Instruments and Methods in Physics Research Section B: Beam Interactions with Materials and Atoms*, pp. 189-193, 2016.
- [23] I. B. R. Z. S. M. J. Valentin Stoytschew, "Influence of experimental parameters on secondary ion yield for MeV-SIMS," *Nuclear Instruments and Methods in Physics Research Section B Beam Interactions with Materials and Atoms*, pp. 194-198, 2016.
- [24] I. B. R. J. D. M. J. L. M. Z. S. R. W. Valentin Stoytschew, "MeV-SIMS yield measurements using a Si-PIN diode as a primary ion current counter," *Nuclear Instruments and Methods in Physics Research B*, pp. 194-198, 2016.
- [25] J.F. Ziegler, J.P. Biersack, U. Littmark, "The Stopping and Range of Ions in Matter," in *Treatise on Heavy-Ion Science*, Pergamon Press, 1985, pp. 93-129.

- [26] D. S. V. N. I. T. T. M. Jakšić, "In-air ion beam analysis with high spatial resolution proton microbeam," *Nuclear Instruments and Methods in Physics Research Section B: Beam Interactions with Materials and Atoms*, pp. 185-188, 2016.
- [27] R.-H. F. J. H. D. J. G. L. D. L. U. R. T. R. A. S. D. S. R. S. W. T. J. V. J. Z. T. Butz, "The Leipzig high-energy ion nanoprobe: A report on first results," *Nuclear Instruments and Methods in Physics Research B*, pp. 161-163, 2000.
- [28] P. H. B. S. a. R. Z. Jonas Bergquist, "Mass spectrometry of proteins - perspectives on past and present," *International Journal of Mass Spectrometry*, pp. 73-82, 2007.
- [29] M. F. M. K. S. N. T. A. J. M. Toshio Seki, "Analysis of liquid materials in low vacuum with Wet-SIMS," *Surface and Interface Analysis*, pp. 1133-1136, 2014.
- [30] R. S. R. M. D.F. Torgerson, "New approach to the mass spectroscopy of non-volatile compounds," *Biochemical and Biophysical Research Communications*, p. 616–621, august 1974.
- [31] K. Wien, "Fast heavy Ion induced desorption," *Radiation Effects and Defects and Solids*, pp. 137-167 , 1989.
- [32] P. Sigmund, "Six decades of atomic collisions in solids," *Nuclear Instruments and Methods in Physics Research Section B: Beam Interactions with Materials and Atoms*, pp. 391-412, September 2017.
- [33] P. Sigmund, "Stopping power: Wrong terminology," *ICRU News*, p. 16.
- [34] J. P. B. U. L. James F. Ziegler, SRIM, The stopping and Range of Ions in Matter, Chester, Maryland: SRIM Co., 2008.
- [35] W. B. a. M. Kitagawa, "Effective stopping-power charges of swift ions in condensed matter," *PHYSICAL REVIEW* 8, pp. 5631-5637, 1982.
- [36] F. F. a. P. M. E. F. Guinea, "Charge States for Protons Moving in an Electron Gas," *Physical Review Letters*, pp. 604-607, 1981.
- [37] J. Lindhard, "On the properties of a Gas of charged particles," *Matematisk-fysiske Meddelelser, bind 28, nr. 8*, pp. 3-57, 1954.
- [38] G. Szenes, "Thermal spike model of amorphous track formation in insulators irradiated by swift heavy ions," *Nuclear Instruments and Methods in Physics Research B* , pp. 141-144 , 1996.
- [39] R. J. E.M. Bringa, "Coulomb Explosions and Thermal Spikes," *Physical Review Letters* 88, May 2002.

- [40] J. A. J. D. S. V. V. a. E. A. S. S. Della-Negra, "The Pegase project, a new solid surface probe: focused massive cluster ion beams," *Surf. Interface Anal.* , p. 66–69, 2011.
- [41] I. B. R. M. B. V. D. S. F. M. K. Z. M. H. M. Z. .. P. Z. S. N. S. T. T. M. Jaksic, "New capabilities of the Zagreb ion microbeam system," *Nuclear Instruments and Methods in Physics Research B* , p. 114–118, 2007.
- [42] "<https://www.pelletron.com/products/mc-snics/>," [Online].
- [43] L. Lamm, "SNICS Ion Source," Nuclear Science Laboratory, 2009.
- [44] R. Middleton, "A Negative-Ion Cookbook," *Department Of Physics, University of Pennsylvania*, 1989.
- [45] S. I. S. (SIS)., "SIMION," 2017.
- [46] A. A. a. F. H. Read, "Electrostatic cylinder lenses II: Three element einzel lenses," *Journal of Physics E: Scientific Instruments*, pp. 150-155, 1972.
- [47] A. S. Carsten Peter Welsch, "Layout of an electrostatic storage ring at IAP," *Proceedings of the 2001 Particle Accelerator Conference*, pp. 2551-2553, 2001.
- [48] J. C. a. E. Walton, "Experiments with high velocity positive ions - (I) further developments in the method of obtaining high velocity positive ions," *Proceedings of the Royal Society of London. Series A, Containing Papers of a Mathematical and Physical Character*, pp. 619 - 630, 1932.
- [49] P. P. H.-P. S. Alfred Holzer, "Cockcroft-walton cascade circuit for voltage multiplication". Patent US3911292 A, 1975.
- [50] V. A. M. E. P. K. K. M. C. N. J. P. M. W. Asad Shariff, "The Lund Nuclear Microprobe sub-micron set-up. Part I: Ion optics calculation," *Nuclear Instruments and Methods in Physics Research Section B: Beam Interactions with Materials and Atoms*, pp. 1-6, april 2005.
- [51] D. J. M.B.H. Breese, "Ion optical study of a transmission ion microscope," *Nuclear Instruments and Methods in Physics Research B* , pp. 236-240, 1999.
- [52] L. M. F. V. Norbert Jakubowski, "Sector field mass spectrometers in ICP-MS," *Spectrochimica Acta Part B* 53 , p. 1739–1763, 1998.
- [53] A. V. L. a. B. A. T. Igor V. Chernushevich, "An introduction to quadrupole – time-of-flight mass spectrometry," *Journal of Mass Spectrometry*, p. 849–865, 2001.
- [54] R. E. March, *Encyclopedia of Spectroscopy and Spectrometry - Ion Trap Mass Spectrometers*, 1999.

- [55] A. E. C. a. D. F. Eggers, "An Ion ``Velocitron",*" The Review of Scientific Instruments*, pp. 605-607, September 1948.
- [56] Z. M. N. S. M. Jaksic, "On the use of pulsed microbeam in IBIC," *Nuclear Instruments and Methods in Physics Research Section B: Beam Interactions with Materials and Atoms*, pp. 176-180, September 2003.
- [57] J. Ladislawszwa, "Microchannel Plate Detectors," *Nuclear Instruments and Methods*, pp. 587-601, 1979.
- [58] GIDS-GmbH, "MCP-Types," Mannheim, 2015.
- [59] G. GmbH, "provided by GIDS GmbH," GIDS GmbH, [Online]. Available: <http://www.gids-gmbh.com>.
- [60] G. C. a. F. Sauli, "High-Resolution Electronic Particle Detectors," *Ann. Rev. Nucl. Part. Sci.*, pp. 285-349, 1984.
- [61] H. N. Seishi Takeda, "An Analysis of Signal Pulse from Semiconductor," *Journal of Nuclear Science and Technology*, pp. 195-204, 1967.
- [62] I.S Gilmore, M.P Seah, "Ion detection efficiency in SIMS: Dependencies on energy, mass and composition for microchannel plates used in mass spectrometry," *International Journal of Mass Spectrometry*, pp. 217-229, 2000.
- [63] D. E. R. Lisa L. Haney, "Delayed extraction for improved resolution of ion/surface collision products by time-of-flight mass spectrometry," *Analytica Chimica Acta* , p. 225–233, 1999.
- [64] T. J. C. a. R. J. Cotter, "A Curved-field Reflectron for Improved Energy Focusing of Product Ions in Time=of=flight Mass Spectrometry," *Rapid Communications in Mass Spectrometry*, pp. 1037-1040, 1993.
- [65] V. I. K. D. V. S. a. V. A. Z. B. A. Mamyrin, "The mass-reflectron, a new nonmagnetic time-of-flight mass spectrometer with high resolution," *Zh. Eksp. Teor. Fiz.* , p. 1973, 82-89 .
- [66] A. M. S. B. E. C.-C. M. B. Dariusz Wegrzynek, "Micro-beam X-ray fluorescence and absorption," *Nuclear Instruments and Methods in Physics Research B* , p. 176–182, 2005.
- [67] Artur Lutfurakhmanov, Gregory K. Loken, Douglas L. Schulz, Iskander S. Akhatov, "Capillary-based liquid microdroplet deposition," *Applied Physics Letters*, pp. 124107-124107-3, september 2010.
- [68] G. Kemp, "Capillary Electrophoresis - A Versatile Family of Analytical Techniques," *Biotechnology and Applied Biochemistry* , pp. 9-17, february 1998.

- [69] C. Sosa, V. Stoytschew, J. Leani, H. J. Sánchez, C. A. Pérez, R. D. Perez, "Calibration Method for Confocal X-Ray Microanalysis with Polychromatic Excitation," *Journal of Spectroscopy*, pp. 1-7, january 2015.
- [70] Ioanna Mantouvalou, Timo Wolff, Christian Seim, Valentin Stoytschew, Wolfgang Malzer, Birgit Kanngiesser, "Reconstruction of Confocal Micro-X-ray Fluorescence Spectroscopy Depth Scans Obtained with a Laboratory Setup," *Analytical Chemistry*, p. 9774–9780, august 2014.
- [71] M.J. Simon, M. Döbeli, A.M. Müller, H.-A. Synal, "In-air STIM with a capillary microprobe," *Nuclear Instruments and Methods in Physics Research B*, pp. 237-240, 2012.
- [72] M. Folkard, B. Vojnovic, G. Schettino, M. Forsberg, G. Bowey, K.M. Prise, B.D., *Nuclear Instruments and Methods in Physics Research B*, pp. 270-273, 1997.
- [73] T. Nebiki, T. Yamamoto, T. Narusawa, M.B.H. Breese, E.J. Teo, F. Watt, J. Vac. Sci., *Nuclear Instruments and Methods in Physics Research B*, p. 1671, 2003.
- [74] T. Nebiki, M. Hasnat Kabir, T. Narusawa, *Nuclear Instruments and Methods in Physics Research B*, pp. 226-229, 2006.
- [75] N. Fujita, K. Ishii, H. Ogawa, *Journal of Physics: Conference Series*, vol. 194, p. 142004., 2009.
- [76] D. Sekiba, H. Yonemura, T. Nebiki, M. Wilde, S. Ogura, H. Yamashita, M., *Nuclear Instruments and Methods in Physics Research B*, vol. 266, p. 4027, 2008.
- [77] J. Hasegawa, S. Shiba, H. Fukuda, Y. Oguri, *Nuclear Instruments and Methods in Physics Research B*, vol. 266, p. 2125, 2008.
- [78] Jun Hasegawa, Sarawut Jaiyen, Chalermpong Polee, Nares Chankow, Yoshiyuki Oguri, "Transport mechanism of MeV protons in tapered glass capillaries," *JOURNAL OF APPLIED PHYSICS*, vol. 110, pp. 044913-1-044913-10, 2011.
- [79] Sarawut Jaiyen, Nares Chankow, Jun Hasegawa, Yoshiyuki Oguri, "Effect of wall material and shape on MeV ion focusing ability of tapered," *Nuclear Instruments and Methods in Physics Research B*, vol. 271, p. 13–18, 2012.
- [80] Roberto D. Pérez · Héctor J. Sánchez · Marcelo Rubio · Carlos A. Pérez, "Characterization of homemade x-ray polycapillaries," *X-Ray Spectrometry*, pp. 646-651, 2009.
- [81] B.L. Henke, E.M. Gullikson, and J.C. Davis., "X-ray interactions: photoabsorption, scattering, transmission, and reflection at E=50-30000 eV, Z=1-92," *Atomic Data and Nuclear Data Tables*, vol. 54, no. 2, pp. 181-342, 1993.
- [82] H. W. Werner, "Quantitative secondary ion mass spectrometry: A review," *Surface and Interface Analysis*, pp. 56-74, 1980.

- [83] W. A. C. T. F. G. H. M. H. K. Z. W. M. Toulemondea, "Electronic sputtering of metals and insulators by swift heavy ions," *Nuclear Instruments and Methods in Physics Research Section B: Beam Interactions with Materials and Atoms*, p. 346–357, 2003.
- [84] G. B. D. F. J. E. H. K. P. D. H. B. S. R.M. Papaléo, "MeV ion sputtering of polymers: correlation between secondary ion radial velocity distributions and heavy ion track structure," *Nuclear Instruments and Methods in Physics Research Section B*, pp. 667-671, june 1994.
- [85] B. U. R. S. B. R. K. a. R. E. J. D. Fenyő, "Molecular-dynamics study of electronic sputtering of large organic molecules," *Phys. Rev. B* , pp. 1895 - 1902, August 1990.
- [86] B. U. R. S. P. H. A. H. a. G. J. Werner Ens, "Directional correlation between the primary particle and ejected molecular ions in electronic sputtering of large organic molecules," *Physical Review B*, pp. 763-766, 1989.
- [87] R. J. B. a. L. Friedman, "A model of secondary electron yields from atomic and polyatomic ion impacts on copper and tungsten surfaces based upon stopping-power calculations," *Journal of Applied Physics*, pp. 3928-3936, 1977.
- [88] A. Benninghoven, "Surface analysis by secondary ion mass spectrometry (SIMS)," *surface science*, pp. 246-260, 1990.
- [89] I. S. G. a. M. P. Seah, "Static SIMS: A Study of Damage Using Polymers," *Surface and Interface Analysis*, pp. 746-762, 1996.
- [90] N. G. M. X. H.-Y. J. F. O. K. Y. Leo W.M. Lau, "Primary ion fluence dependence in time-of-flight SIMS of self-assembled," *Applied Surface Science* 255, p. 1029–1032, 2008.
- [91] A. L. Evelyn, "MeV ion beam interaction with polymer films containing cross-linking agents," *AIP Conference Proceedings*, pp. 753-756, 1999);.
- [92] R. Norarat, "Development of imaging with MeV ions," *PhD Thesis*, 2013.
- [93] R. N. S. Sodhia, "Time-of-flight secondary ion mass spectrometry (TOF-SIMS):—versatility in chemical and imaging surface analysis," *Analyst*, pp. 483-487, 2004.
- [94] J. ö. P. W. Klaus Franzreb, "Quantitative study of oxygen enhancement of sputtered ion yields. I. Argon ion bombardment of a silicon surface with O2 flood," *Surface Science*, pp. 291-309, 10 12 2004.
- [95] F. T. J. D. I. Constant, "Deposition and removal of sodium contamination on silicon wafers," *Semiconductor Science and Technology*, pp. 61-66, 2000.
- [96] J. D. H. J. Y. L. B. I. B. ., G. B. R. G. a. K. S. Della-Negra, "Heavy particle induced ion emission from Langmuir-Blodgett films: dependence on the charge state and the angle of incidence," *Nuclear Instruments and Methods in Physics Research B*, pp. 121-128, 1990.

- [97] R. B. S. D. N. C. D. W. E. Y. L. D. M. B. S. a. K. S. G. Bolbach, "Variation of yield with thickness in SIMS and PDMS: Measurements of secondary ion emission from organic molecular films," *Nuclear Instruments and Methods in Physics Research B*, pp. 74-82, 1988.
- [98] W. v. G. J. v. D. P. R. J. J. N. C.W.T. Bulle-Lieuwma, "Characterization of polymer solar cells by TOF - SIMS depth profiling," *Applied surface science*, pp. 547-550, 2003.
- [99] A. D. P. B. a. H.-N. M. L. Nittler, "Insights into the yield enhancement and ion emission process in metal-assisted SIMS," *Surf. Interface Anal.*, p. 18-21 , 2012.
- [100] D. H.Arwin, "Unambiguous determination of thickness and dielectric function of thin films by spectroscopic ellipsometry," *Thin Solid Films*, pp. 101-113, 1984.
- [101] T. J. C. K. K. B. L. N. F. B. M.-S. J. D. S. P. W. B. J. V. S. Sage J. B. Dunham, "Metal-assisted polyatomic SIMS and laser desorption/ionization for enhanced small molecule imaging of bacterial biofilms," *Biointerphases*, pp. 02A35-1 -02A35-11, 2016.
- [102] K. J. A. D. M. R. S. Z.X.Jiang, "Quantitative SIMS analysis of SiGe composition with low energy O₂⁺ beams," *Applied Surface Science*, pp. 7262-7264, 2006.
- [103] A. Y. N. N. S. S. Hisayoshi Yurimoto, "Quantitative SIMS analysis of GSJ rock reference samples," *GEOCHEMICAL JOURNAL*, pp. 215-236, 1989.
- [104] P. A. a. M. P. Vieillescazes, "Study of Post-Byzantine Icon Varnishes by Chromatographie and Spectroscopic Methods," *Studies in Conservation*, pp. 37-44, 2005.
- [105] T. C. a. F. F. R.N. KATZ, "Particle Bombardment (keV) Mass Spectra of Ethylene, Glycol, Glycerol and Water at sub-ambient temperatures," *International Journal of Mass Spectrometry and Ion Processes*, pp. 85-97, 1987.
- [106] A. Chapiro, "Chemical modifications in irradiated polymers," *Nuclear Instruments and Methods in Physics Research Section B: Beam Interactions with Materials and Atoms*, pp. 111-114, 1988.
- [107] E. Union, "EUR-LEX," 2002. [Online]. Available: <http://eur-lex.europa.eu/legal-content/EN/TXT/?uri=celex:32002L0095>.
- [108] D. B. A. H. John C. Vickerman, Static SIMS Library, SurfaceSpectra Ltd. , 2006.
- [109] B.-A. A. J.R.Majer, "The Mass Spectrum of Glycine," *Organic Mass Spectrometry*, pp. 147-152, 1981.
- [110] A. R. S. N. D. L. US Department of Agriculture, "USDA National Nutrient Database for Standard Reference," July 2017. [Online]. Available: <https://ndb.nal.usda.gov/ndb/>.

Notes:

за моето семейство